Dissertation
submitted to the
Combined Faculties of the Natural Sciences and Mathematics
of the Ruperto-Carola-University of Heidelberg, Germany
for the degree of
Doctor of Natural Sciences

Put forward by

Master Phys. Tatiana Vasyunina
born in: Verkhnyaya Salda (Russia)

Oral examination: December 13th, 2010

VERY EARLY STAGES OF MASSIVE STARS

REFEREES: PROF. DR. THOMAS HENNING
PROF. DR. RALF KLESSEN

Zusammenfassung

Es ist das Ziel dieser Doktorarbeit, die Anfangsbedingungen sowie die frühen Phasen der Entstehung massereicher Sterne mittels geeigneter Beobachtungsstudien zu untersuchen. Hierfür haben wir zwei Objektklassen ausgewählt: Infrarot–Dunkelwolken (IRDCs) sowie ein nachfolgendes Stadium, welches durch die Existenz eines noch jungen, eingebetteten (Proto)-Sternhaufens gekennzeichnet ist.

Als ersten Schritt haben wir die Massen und Säulendichten für eine neue Stichprobe von südlichen IRDCs bestimmt unter Verwendung von eigenen Kontinuumsemissionskarten im Millimeter–Bereich sowie von Extinktionsdaten, basierend auf archivierten Infrarot–Karten des *Spitzer*–Satelliten. Die abgeleiteten Parameter zeigen, daß diese IRDCs potentielle Kandidaten für die Geburtsplätze massereicher Sterne sind und nicht unbedingt nur Sterne niedriger und mittlerer Masse produzieren werden. Insbesondere der Vergleich unserer Resultate mit schon bestehenden Daten für molekulare Kerne niedriger Masse ohne Sternentstehungsaktivität zeigt, daß IRDCs einen Trend zu systematisch höheren Säulendichten zeigen. Die interpolierten zentralen Höchstwerte für die Säulendichten überschreiten auch den kritischen Schwellenwert, der von einigen theoretischen Studien als entscheidend für die Entstehung massereicher Sterne angesehen wird. Desweiteren setzen wir uns kritisch mit den Limitierungen der angewandten Emissions- und Extinktionsmethoden auseinander.

Zweitens haben wir die physikalischen Bedingungen sowie die chemische Zusammensetzung des mit den IRDCs assoziierten dichten Gases unter Verwendung von Millimeter–Spektroskopie für einer Reihe von Moleküllinien analysiert. Alle Wolken zeigen komplexe HCO^+ Linienprofile, und in einigen IRDCs finden wir SiO–Emission. Diese Befunde weisen auf Einfall- und Ausfluß–Bewegungen zumindest in einigen Substrukturen der IRDCs hin und somit auf schon einsetzende Sternentstehungsaktivität. Im Vergleich mit Kernen niedriger Masse besitzen die IRDCs stärkere und vor allem deutlich breitere Linien, was auf einen erhöhten Grad an Turbulenz hinweisen kann. Trotzdem zeigt unsere Analyse, daß die chemischen Häufigkeiten diverser Moleküle in den IRDCs den entsprechenden Häufigkeiten in sehr jungen massearmen Molekülwolkenkernen sehr ähnlich sind. Dies deutet auf ähnliche chemische Anfangsbedingungen für massearme und massereiche Sternentstehungsregionen hin.

Schließlich haben wir die stellare Zusammensetzung und die Umgebungsbedingungen in dem jungen eingebetteten Sternhaufen IRAS 06058+2138 untersucht. Grundlage ist die Analyse aller verfügbaren Beobachtungsdaten, welche einen großen Wellenlängenbereich, vom nahen und mittleren Infrarot bis hin zum Millimeter- und Zentimeterbereich, abdecken. Neue 3D–Infrarotspektroskopie–Daten mit dem VLT–Instrument SINFONI nahmen hierbei eine Schlüsselstellung ein. Wir können den Sternhaufen in drei Teilregionen unterteilen, die sich in unterschiedlichen Stadien der Sternentstehung befinden. Aufgrund des Vergleiches der Alter sowie der relativen Lage dieser Untergebiete folgern wir, daß die Beschaffenheit dieser Region nicht durch einen Akt der sogannten "getriggerten" Sternentstehung gesteuert worden ist. Deshalb nehmen wir an, daß es sich um einen Fall von rein sequentieller Sternentstehung handelt. Mit dieser Arbeit untermauern wir auch die Wichtigkeit eines multispektralen Ansatzes für solche Beobachtungsstudien. Hiermit können sowohl die stellare Population als auch noch sehr tief eingebettete Objekte simultan untersucht werden, was eine zuverlässigere Rekonstruktion der Sternentstehungsabfolge für solche komplexen Sternhaufen ermöglicht.

Abstract

The goal of this thesis work is to investigate the initial conditions and the early phases of the formation of high–mass stars by means of dedicated observational studies. We consider two object classes: infrared dark clouds (IRDCs), and a subsequent stage characterized by the presence of young embedded (proto-)stellar clusters.

First, we estimate masses and column densities for a completely new sample of southern IRDCs, utilizing our own millimeter continuum emission maps as well as *Spitzer* satellite data. The parameters we derive show that IRDCs from our sample have the potential to form not only low- and intermediate-mass stars, but can also be the birth places of massive stars. In particular, the comparison of our results with previously obtained data for low-mass starless cores shows a clear trend for IRDCs to have systematically higher column densities. The interpolated IRDC peak column densities exceed the threshold for the onset of massive star formation previously advocated by theoretical studies. We also critically evaluate the limitations of the applied emission and extinction methods.

Second, we investigate the physical conditions and the chemical composition of the dense gas within the IRDCs of our sample by means of a multi–line molecular spectroscopy analysis. All the clouds have complex HCO^+ line profiles, and we detect SiO emission in some clouds. These findings mark the presence of infall and outflow motions in at least some parts of the IRDCs, and hence, ongoing star formation. In comparison with low-mass starless cores, the IRDCs have broader and more intense lines. Thus, they may be characterised by more turbulent conditions. Nevertheless, we find a tendency for the IRDCs to have molecular abundances similar to the case of low-mass starless cores. This indicates similar chemical initial conditions for low- and high-mass star-forming regions.

Finally, we study the stellar composition and environmental conditions in the young embedded cluster IRAS 06058+2138. We perform an analysis of all the available data, covering the near- and mid-infrared as well as the centimeter and millimeter wavelength range. In particular new VLT/SINFONI integral–field spectroscopy data have played a pivotal role. We identify three star-forming clusters at different evolutionary stages. Comparing the relative ages of these clusters and their relative locations, we conclude that triggering could not have led to the cluster configuration we see in the region. Thus, we assume a merely sequential star-formation scenario for this region. With this study, we also demonstrate the importance of a multi–wavelength approach. Combining data at different wavelengths allows us to investigate both the more evolved stellar population, as well as very young embedded objects, and hence, to reconstruct the star-forming history of structured cluster environments.

To my great-grandma and grandpa.

Acknowledgements

I would like to acknowledge my supervisors, Prof. Thomas Henning and Dr. Hendrik Linz and Dr. Arjan Bik for their great help during my PhD work. Also, I am thankful to my co-authors and colleagues: Bringfried Stecklum, Igor Zinchenko, Henrik Beuther, and Maxim Voronkov. Without their effort this work would never have appeared. Of course, I am very grateful to IMPRS Heidelberg for the financial support, and especially to the IMPRS coordinator Christian Fendt for his help. I would like to thank the non-scientific staff of the Max Planck Institute for Astronomy; their help in practical questions was very valuable and made my scientific work much more efficient and life – easier. I also wish to thank Eric Herbst, Jürgen Steinacker, Sarah Ragan, Bhargav Vaidya and Paul Boley for useful discussions and Sergej Koposov for the assistance in software installation. Above all, I am deeply appreciative to all my friends and family for their great support during my PhD.

Contents

List of Figures

List of Tables

1

Introduction

One of the key challenges in stellar astrophysics is to understand the formation and earliest evolution of high-mass stars. These objects play a major role in shaping the interstellar medium due to their strong UV radiation fields and stellar winds, and enrich their environment with heavy elements as they explode as supernovae. Massive stars are the only objects which we can observe and study in other galaxies. Despite their importance, there are many unresolved problems concerning both theory and observations (Beuther et al., 2007; Zinnecker & Yorke, 2007).

In particular, the mechanism by which such massive stars form is not clear. The main problem is posed by the radiation pressure from the star, which, at least in simplistic spherically symmetric configurations, would eventually quench the accretion process so that the forming star were not able to gain mass beyond 8...10 $M_\odot$. Currently, two principle high-mass star formation scenarios exist. The first mechanism is the so-called monolithic collapse (McKee & Tan, 2002, 2003). This mechanism is similar to the low-mass scenario, but several parameters are scaled–up. As in the case of low-mass stars, in this mechanism the central star accretes through a circumstellar disk. However, the accretion rate invoked here is two orders of magnitude higher. The presence of outflows and jets in this model let the radiation preferentially escape through the outflow cavities (Krumholz et al., 2009), although the relevance of non–axialsymmetric effects is under debate (see Kuiper et al., 2010a). The second mechanism is competitive accretion, which suggests that lower-mass companions compete with a high-mass star for the same gas reservoir (Bonnell et al., 1997, 1998) and hence the final stellar masses are determined by the subsequent accretion of unbound gas from the clump, and that the cluster environment sets important boundary conditions for star formation (Bonnell & Bate, 2006; Clark et al., 2008).

Theoretical modeling now can include more and more effects (e.g., turbulence, ionising radiation, magnetic fields etc.), 3D configurations and better spatial resolution (e.g. Kuiper et al., 2010b; Peters et al., 2010; Smith et al., 2010). To test and improve theoretical models we need a clear observational picture, especially in the early phases, to constrain the models sufficiently. However, observations of massive stars have their own difficulties. Massive stars are typically distant and mostly form in clusters, which requires high spatial resolution observations and thus makes it difficult to distinguish single objects. The high dust extinction is a further complication for the observation of the initial stages and the already formed embedded young clusters.

Observationally, several evolutionary stages of massive stars can be identified. The earliest stage is represented by cold massive clumps with embedded dense cores. One manifestation of this stage are cold and dense infrared dark clouds (IRDCs). IRDCs show a large spread in masses, from around hundred to several thousands of solar masses, and sizes from 0.5 to 10 pc. It is assumed that some of them have a potential to harbour massive pre-stellar cores (e.g. Carey et al., 2000; Ragan et al., 2009; Rathborne et al., 2006). The next stage is the class of more evolved high-mass protostellar objects (HMPOs). HMPOs are bright at mid- and far-IR wavelengths and characterized by higher gas temperatures, compared to IRDCs. It is assumed that these objects present one of the early stages of high-mass star formation, where the central protostar has a mass $> 8\ M_\odot$ and is still accreting. This stage can be characterized by the presence of hot molecular cores and hypercompact HII regions. (e.g. Beuther et al., 2007; Sridharan et al., 2002). In the following stage, the star stops accreting and starts to clean up its environment. At this moment the newly born massive star can be detected by its ionising radiation, and is detectable as an ultracompact HII region (UC HIIR). In this thesis we focus on the two stages of massive stars and will discuss it further in more details.

1.1 Infrared dark clouds

One possible means of studying the initial conditions of massive stars is to analyse the so-called Infrared Dark Clouds (IRDCs). IRDCs were first identified by the *In-*

frared Space Observatory (*ISO*; Perault et al., 1996) and *Midcourse Space Experiment* (*MSX*; Egan et al., 1998) as dark extended features against the bright Galactic PAH background at mid-IR (MIR) wavelengths. The chronology of IRDC studies is presented in the Table A.

First millimeter and submillimeter continuum observations allowed to estimate physical parameters of IRDCs. It was found that they have typical sizes between 1 and 10 pc, masses from several hundreds to several thousands solar masses and H_2 column densities between 2 and 10×10^{23} cm^{-2} (e.g. Carey et al., 2000; Ragan et al., 2009; Rathborne et al., 2006).

Apart from continuum observations, molecular line data have been used to characterize the properties of IRDCs. Molecular line observations allow us to obtain additional information about our objects and specify parameters, which have been already known. Ammonia observations by Sridharan et al. (2005) and Pillai et al. (2006a) allowed temperature determination of IRDCs in a range from 10 to 20 K, Simon et al. (2006b), using ^{13}CO J=1–0 molecular line emission, estimated kinematic distances to 313 clouds. Information about temperatures and distances to the clouds let us improve our estimation of their sizes and masses.

Distance determination also allows to reconstruct the Galactic distribution of IRDCs. Simon et al. (2006b) showed that most IRDCs are been associated with the so-called Galactic molecular ring (galactocentric distance of 5 kpc). However, a later study by Jackson et al. (2008) gave new evidence that the IRDC distribution in the first and fourth galactic quadrant more closely follows a galactic spiral arm (the Scutum-Centaurus arm). Since in normal spiral galaxies, OB stars seem to form primarily in spiral arms, the association of IRDCs with a Milky Way spiral arm supports the idea that IRDCs are related to high-mass star formation.

Another aspects of molecular line study are probing the chemical composition and estimation of the IRDCs evolutionary status. Carey et al. (1998) detected H_2CO in 10 clouds, thus confirming the presence of dense gas. Using LVG modeling they estimated H_2CO abundances of $\sim 10^{-10}$. That is a factor of 50 lower in comparison with low-density clouds and can be explained by accretion of gas-phase metals onto dust grains in the cold and dense IRDCs. Sakai et al. (2008) observed N_2H^+(1-0), HC_3N(5-4), CCS(4_3-3_2), NH_3(1,1), (2,2), (3,3) and CH_3OH(7-6) lines toward the massive clumps associated with IRDCs, to determine their evolutionary status and to study the chemical conditions in them. Analysing the CCS and N_2H^+ abundance ratio, they conclude that infrared dark clouds are chemically more evolved than low-mass pre-stellar cores. An estimation of the chemical evolutionary status of IRDCs was performed also by Gibson et al. (2009). Using $C^{18}O$, CS and N_2H^+ abundances, and a chemical evolution code, they showed that cores where all three lines are detected appear to be chemically young ($10^{4.5} < t < 10^{5.5}$ years). Cores where no N_2H^+ emission is detected are suspected to be especially young ($t < 10^2$ years). This suggests that these regions may not have yet formed massive protostars.

While many characteristics of infrared dark clouds were determined during the last ten years, some of their properties are still not well known. Are the physical conditions in the places of massive star-formation the same as in the low-mass star forming regions? What is the chemistry in IRDCs? Is it really different from the chemistry in low-mass dark clouds? We will address these questions in the thesis.

1.2 Young embedded clusters

Apart from the earliest phases we consider the following stage, when massive stars have been formed, but are still being located in a deeply embedded environment. In the cluster environment stars interact with each other via stellar winds, ionizing radiation and outflows, which can trigger star formation, or, on the contrary, destroy cloud cores and circumstellar envelopes around other stars.

We started a program to obtain near-IR spectroscopic data of a sample of high-mass star-forming regions at different evolutionary stages. For this purposes the integral field spectrograph SINFONI at the VLT has been used. Integral-field spectroscopy allows to obtain a spectra of every single pixel in the field. Thus, we can extract the spectra of all stars in the region, determine their spectral class and, finally, an age of the cluster. Furthermore, we can analyse spectra of extended emission and identify outflows and photon dominated regions (PDRs). However, when using only near-IR wavelengths it is difficult to reconstruct the physical processes, which take place in the region. To get more detailed information about the cluster and its surroundings and draw some conclusions about the possible star formation mechanisms, we have to use a multiwavelength approach.

1.3 Structure of the dissertation

This thesis consists of three chapters:

The following two chapters concern of the investigation of the physical properties of IRDCs and their chemical composition. Chapter 2 is devoted to the characterization of the continuum properties of southern infrared dark clouds. First, we cross-correlate 1.2 mm continuum data from SIMBA/SEST with Spitzer/GLIMPSE images to establish the connection between emission sources at millimeter wavelengths and the IRDCs that we observe at 8 μm in absorption. Then, analysing the dust emission and extinction data, we estimate IRDC masses and column densities, which are important quantities in characterizing the initial conditions of massive star formation. We also determine the limitations of the emission and extinction methods. Finally, we compare our results with the previously obtained data for low-mass pre-stellar cores, high-mass cores and with theoretical models.

In the third chapter we continue our IRDC study and investigate their chemical composition. On this purpose, molecular line observations at 3mm toward 15 IRDCs with 22-m Mopra radio telescope were performed. We present the qualitative analysis of the obtained spectra, estimate line parameters and analysis of the HCO^+ and $H^{13}CO^+$ line asymmetries. Using molecular hydrogen column densities estimated in the Chapter 2, we calculate molecular abundances of all species. We show, that abundances of different species in IRDCs are quite similar to the abundances in low-mass pre-stellar objects.

The fourth chapter is devoted to the later evolutionary stage, which is related to the embedded, newly formed massive stars in typical cluster environments. Using near-infrared spectroscopy from the SINFONI spectrograph at the VLT, we obtained spectral data cubes cube with spatial information along the x and y axes and spectral information along the z axis for the young cluster IRAS 06058+2138. From SINFONI near-infrared spectra we derived a spectral classification of all cluster members, detect outflows, investigate the interaction between the cluster and its surroundings (ionization front, photon dominated regions). Supporting Spitzer/IRAC data as well as millimeter SMA data allow to perform the detection of the most embedded objects.

The chapters with scientific results listed above are precluded with an introductory part and finished by concluding remarks about future prospects for the presented work and some more technical appendices.

2

Physical properties of southern infrared dark clouds

Based on *Physical properties of southern infrared dark clouds*, Vasyunina, T., Linz, H., Henning, Th., Stecklum, B., Klose, S., Nyman, 2009, Astronomy and Astrophysics, vol. 499 issue 1, pp. 149-161.

2.1 Introduction

While many characteristics of infrared dark clouds were estimated during last ten years, the number of IRDCs with well characterised properties remains small, especially those observable from the southern hemisphere, where ALMA will play a major role in the near future. To enlarge the sample of well-investigated IRDCs, we selected new sample of clouds in the southern hemisphere and started a program to measure the gas and dust properties of these objects. The present chapter aims at characterizing the continuum properties of southern IRDCs.

Since IRDCs are suppose to be cold, their thermal dust emission shows maximum at millimeter and submillimeter wavelength. For our research we use 1.2 millimeter data from SIMBA at the SEST telescope and 8μm IRAC data from Spitzer. Analysis of the dust emission and extinction allows us to determine masses and column densities of IRDCs, which are important quantities in characterizing the initial conditions of massive star formation.

The organization of this chapter is the following. In Sect. 2.2, we describe our source selection and 1.2 mm continuum observations with the SIMBA/SEST telescope. In Sect. 2.3, we discuss the data reduction and the details concerning the calculation of dust masses and column densities. We also present a comparison between the MIR and millimeter techniques. In Sect. 2.4, we compare our results with previous results for high- and low-mass star-forming region and theoretical models.

2.2 Observations

The IRDCs for our study were selected in the pre–Spitzer era, by visual examination of the MIR images delivered by the MSX satellite. The MSX A band (6.8 – 10.8 μm) was the most sensitive of all the MSX bands and exhibits the highest level of diffuse background emission (due to PAH emission at 7.7 and 8.7 μm), which also produces the highest contrast between bright background and dark IRDCs. We selected a sample of southern IRDCs from the A band images by searching for high contrast and sizes sufficient to fill the main beam of the SEST telescope at 1.2 mm.

The 1.2 mm continuum observations were carried out with the 37-channel bolometer array SIMBA (Nyman et al., 2001) at the SEST on La Silla, Chile between July 16 – 18, 2003. SIMBA is a hexagonal array in which the half–power beamwidth (HPBW) of a single element is about $24''$ and the separation between elements on the sky is $44''$. The observations were completed using a fast–mapping technique without a wobbling secondary (Weferling et al., 2002).

Maps of Uranus were taken to check the flux calibration of the resulting data. To correct for the atmospheric opacity, skydips were performed every 2 – 3 hours. Despite the occurrence of some thin clouds, the observing conditions were good, which is reflected in the zenith opacity values of 0.16 – 0.18. The pointing was checked roughly every two hours and was found to be superior to $6''$. The combination of typically three maps of sizes $560'' \times 900''$ resulted in a residual noise of about 22 – 28 mJy/beam (rms) at the center of the mapped region.

2.3 Data reduction and analysis

We use both 8 μm IRAC data from the Spitzer Galactic Legacy Infrared Mid-Plane Survey Extraordinaire (GLIMPSE, Benjamin et al., 2003) and our 1.2 mm data from the SIMBA bolometer at the SEST telescope to investigate the physical properties of the extinction and emission material.

To derive the masses of the IRDCs, in both cases we need to determine the distances to these clouds. To estimate the (kinematic) distances to our IRDCs, we use the $v_{\rm LSR}$ velocities derived from recent molecular line observations[1] acquired with the Australian MOPRA telescope, which we present in a forthcoming paper. The velocities were transferred to kinematic distances by adopting the improved parameters for the Galactic rotation curve (Levine et al., 2008) for the fourth and first Galactic quadrant. The closest kinematic distance was always assumed. The corresponding distances used in the mass estimations are reported in Table 2.3. We note that these rotation curves provide average properties. The true distribution of material might be more structured, especially in the fourth quadrant, which is indicated in the HI absorption measurements shown in Levine et al. (2008). Furthermore, for objects in the Galactic longitude interval $[305°, 310.5°]$, several velocity systems can occur due to the projection of at least two Galactic arms. The measured velocities, however, place all our IRDCs in that longitude range within the Centaurus arm (3.5 − 5.5 kpc), in agreement with Saito et al. (2001).

2.3.1 Millimeter data

The 1.2 mm data for the IRDC regions from SIMBA at the SEST telescope were reduced using the MOPSI package (developed by R. Zylka, IRAM). All maps were reduced by applying the atmospheric opacity corrections, fitting and subtracting a baseline, and removing the correlated sky noise. Thereby, we followed a three-stage approach as suggested in the SIMBA manual. After a first iteration using all data for the sky–noise removal, the map regions showing source emission are neglected for sky–noise removal in the second iteration. From this second interim map, a source model is derived, which is included in the third iteration. The resulting maps were flux–calibrated using the conversion factor obtained from observations of Uranus. For our July 2003 observations, this factor was around 60 mJy/beam per count.

For estimating cloud masses and column densities we used the following expressions:

$$M_{\rm tot} = \frac{F_{\rm int}\ D^2\ R}{B_v(T)\ \varkappa_\nu}, \tag{2.1}$$

---

[1] The HCO$^+$(1-0) line velocities have been employed for this purpose.

$$N_{\mathrm{H}_2} = \frac{F_{\mathrm{peak}}\ R}{\Omega\ B_v(T)\ \varkappa_v\ \mathrm{m}_{\mathrm{H}_2}}. \tag{2.2}$$

The measured source peak flux density is given by F_{peak}, F_{int} denotes the integrated flux density of the complete source, Ω is the beam solid angle in steradians, $\mathrm{m}_{\mathrm{H}_2}$ is the mass of one hydrogen molecule, D is the distance to the IRDC, R is the gas-to-dust ratio, $\varkappa_v$ is the dust opacity per gram of dust, and $B_v(T)$ is the Planck function at the dust temperature T. We adopt a gas-to-dust mass ratio of 100, and $\varkappa_v$ equal to 1.0 $\mathrm{cm}^2\ \mathrm{g}^{-1}$, a value appropriate for cold dense cores (Ossenkopf & Henning, 1994).

At the present stage, where measured temperatures are unavailable for our sources, we assume a temperature of 20 K, which is a reasonable choice considering investigations toward other IRDCs (Carey et al., 1998; Pillai et al., 2006c). The derived mass depends on the (assumed) temperature, on the distance to the cloud, and on the grain model. Masses are underestimated if the temperature is lower than the assumed value of 20 K. For example, at 15 K the masses will be higher by a factor of 1.5. In case of a higher temperature in the cloud, e.g., for 30 K, our results must be divided by a factor of 1.7. We further note the quadratic dependence of the derived masses on the distance to the clouds. Hence, the masses will be a factor of 1.2 - 1.8 higher, if the distance is 500 pc more, and lower by the same factor if it is 500 pc less than indicated by the average Galactic rotation curve (see above). The derived masses are inverse proportional to the assumed value of the opacity $\varkappa_v$, which has an uncertainty of at least a factor 2. The column density has no direct dependence on the distance to the cloud, but the temperature dependence is the same as for the masses.

2.3.2 GLIMPSE 8 μm data

The original selection of the IRDCs was completed on the basis of MSX images. In the meantime, the Spitzer satellite has since succeeded MSX and provided a far higher spatial resolution and sensitivity. GLIMPSE images for our regions with a pixel size of $0.6''$ were retrieved from the NASA/IPAC Infrared Science Archive (IRSA) and remosaicked to cover the final field of our 1.2 mm maps of typically $15' \times 15'$ to determine how the IRDCs relate to their closer and further vicinity (see Figs. 2.1–2.3). After bad–pixel removal, a PSF photometry was performed using the STARFINDER program (Diolaiti et al., 2000). This allows us to remove compact foreground objects, and thus

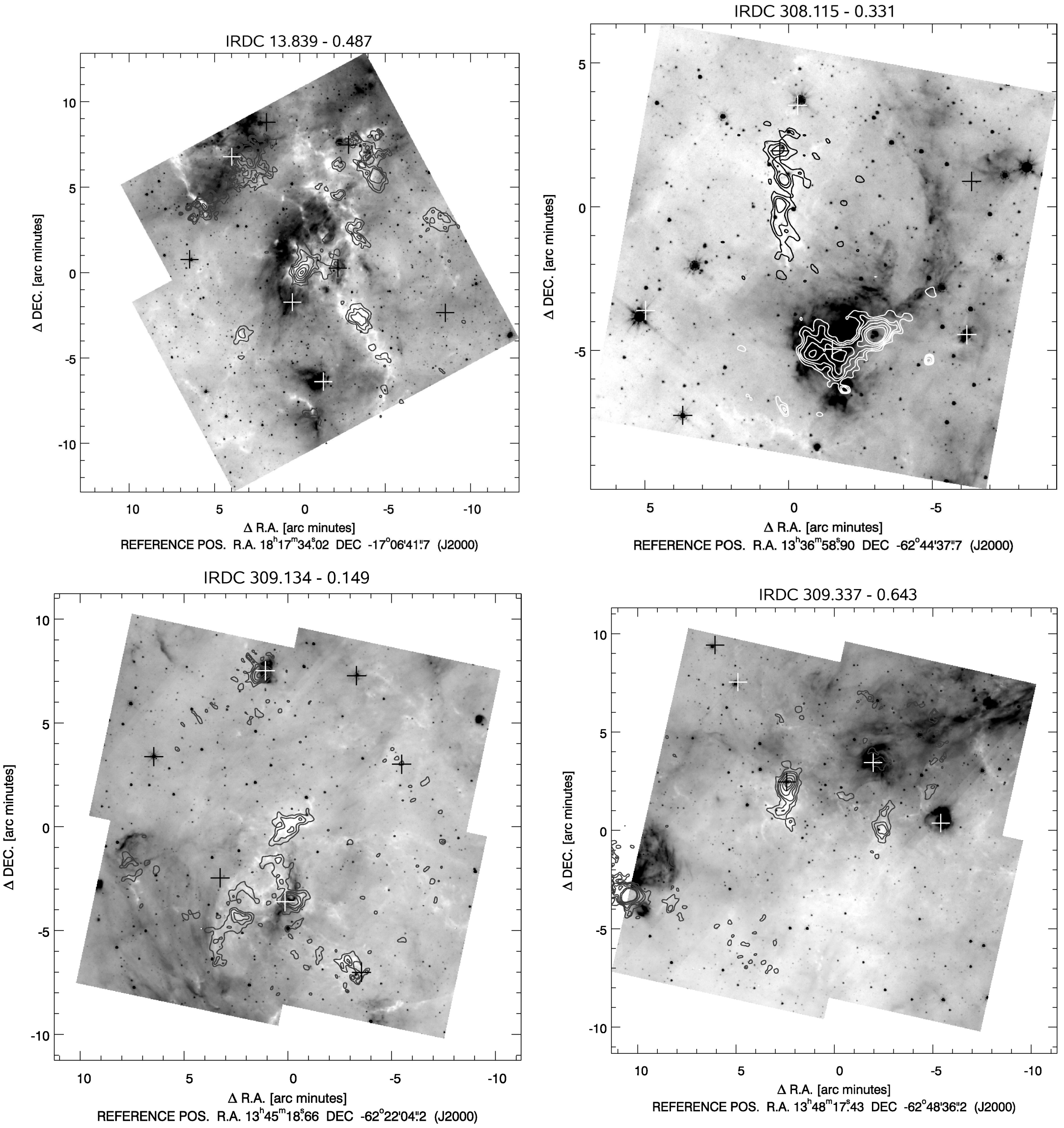

Figure 2.1 Inverse grey-scale 8 micron maps overlaid with 1.2 mm continuum emission. The intensity of a grey-scale image corresponds to the square root of the inverse intensity in mJy. The contours are 60, 108, 156, 240, 360, 480 mJy beam^{-1} in all cases. Crosses denote the position of IRAS point sources.

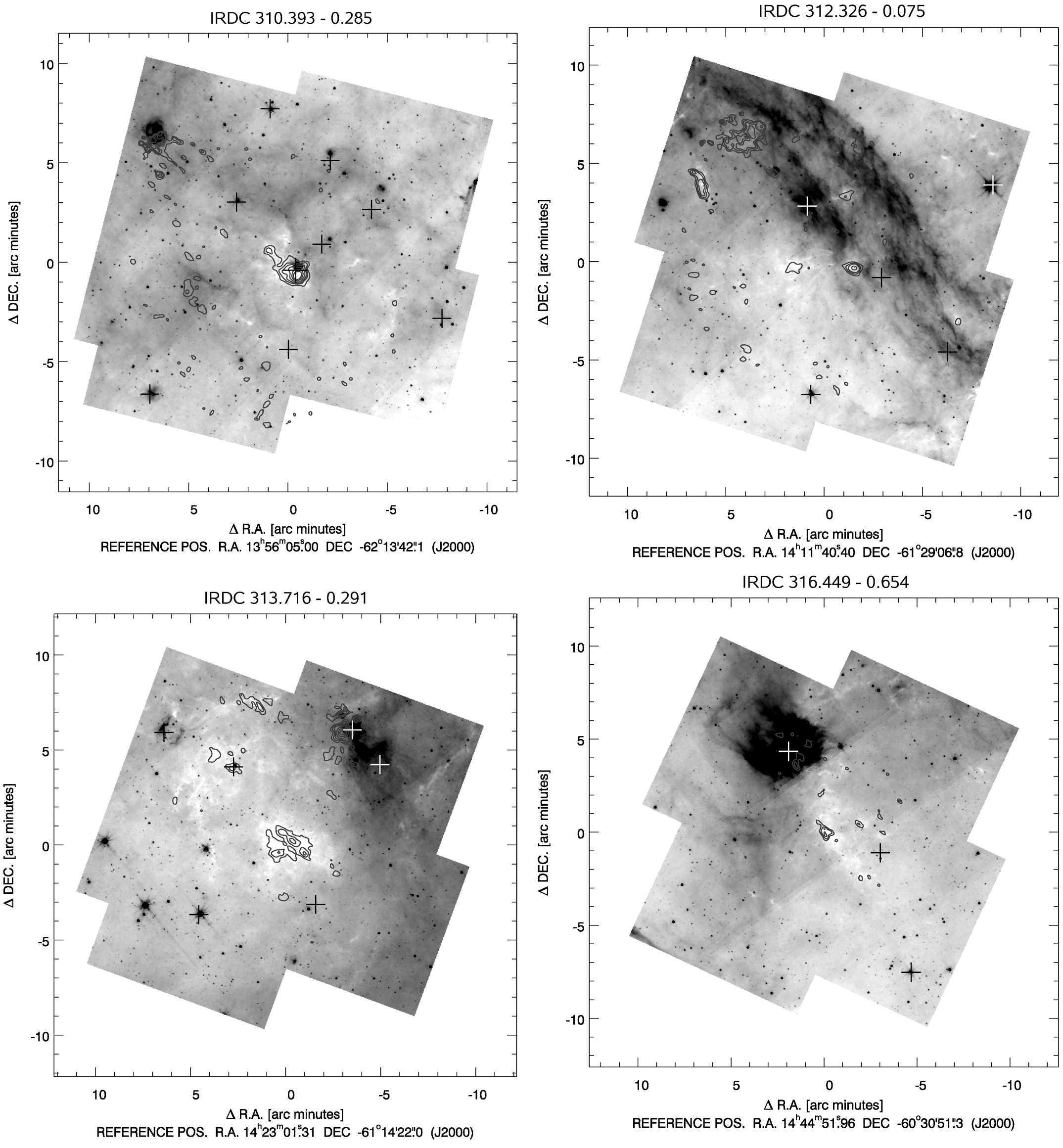

Figure 2.2 Inverse grey-scale 8 micron maps overlaid with 1.2. mm continuum emission. The intensity of a grey-scale image corresponds to the square root of the inverse intensity in mJy. The contours are 60, 108, 156, 240, 360, 480 mJy beam^{-1} in all cases except for IRDC 316.45-0.65 where it is 84, 120, 156, 240, 360, 480 mJy beam^{-1}. Crosses denote the position of IRAS point sources.

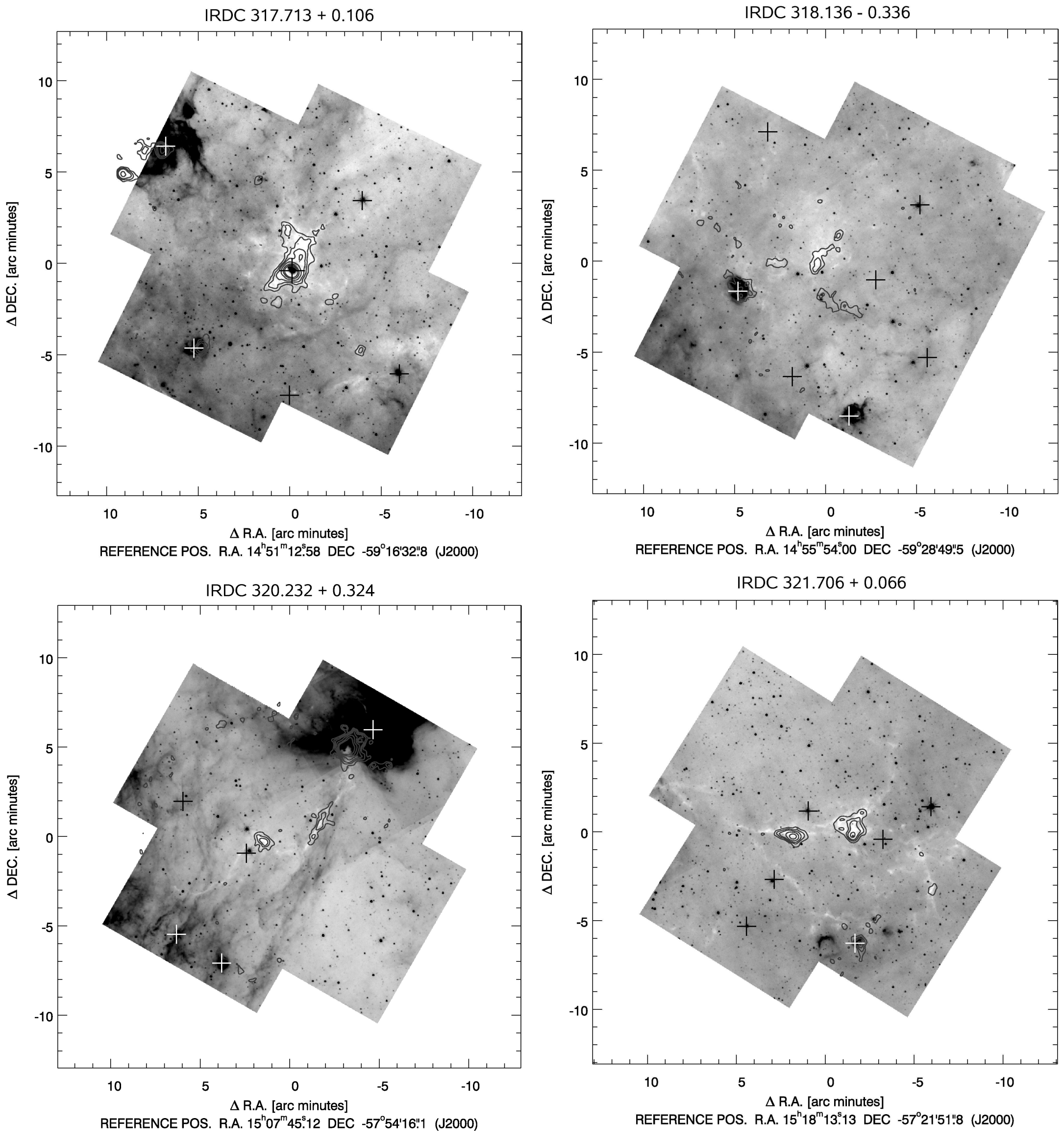

Figure 2.3 Inverse grey-scale 8 micron maps overlaid with 1.2. mm continuum emission. The intensity of a grey-scale image corresponds to the square root of the inverse intensity in mJy. The contours are 60, 108, 156, 240, 360, 480 mJy beam^{-1} in all cases. Crosses denote the position of IRAS point sources.

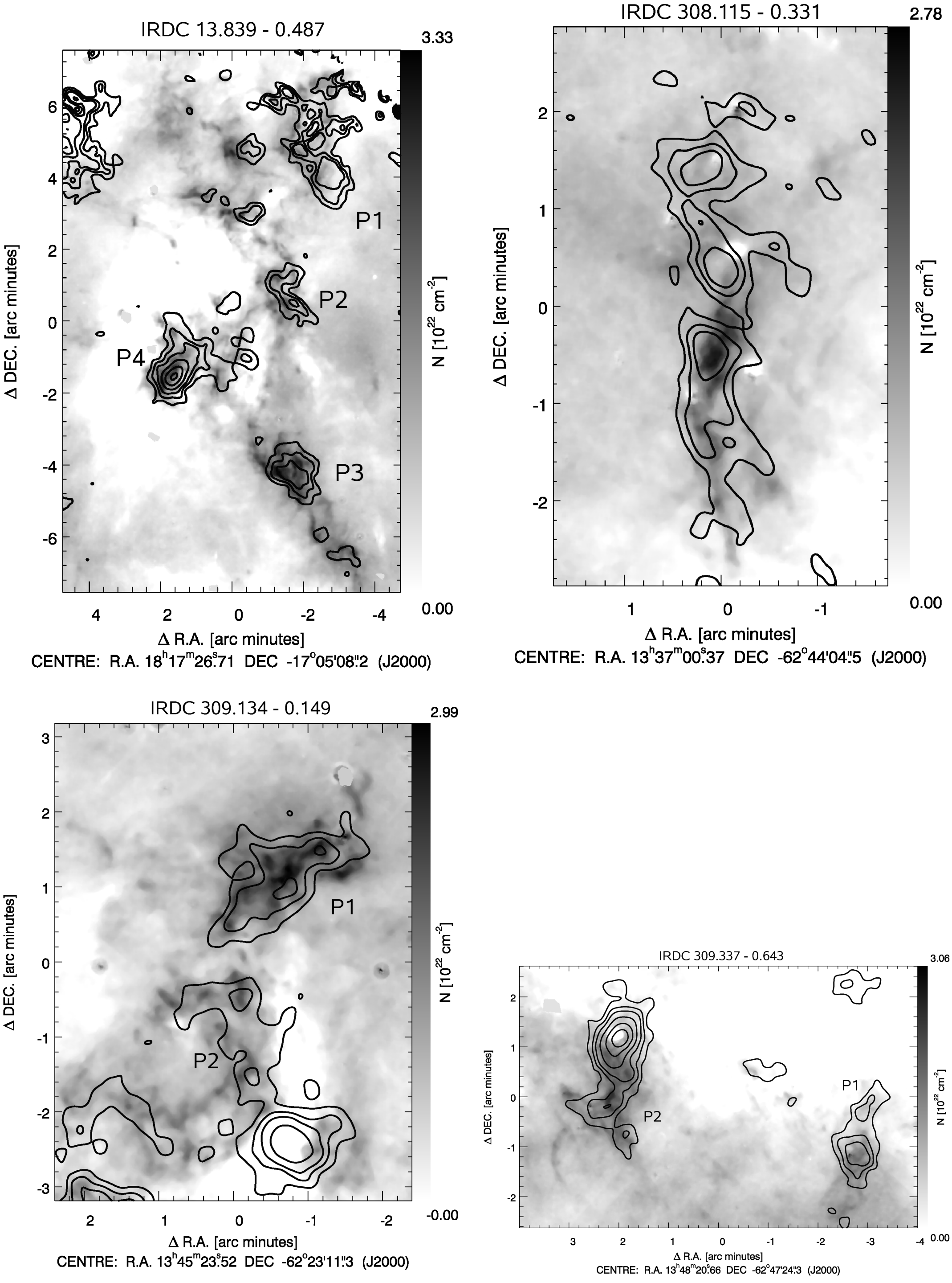

Figure 2.4 Column density maps derived from 8 μm extinction overlaid with 1.2 mm continuum emission as contours. The scaling is indicated in the bar to the right of each image. The contours are 60, 108, 156, 240, 360, 480 mJy beam^{-1} in all cases.

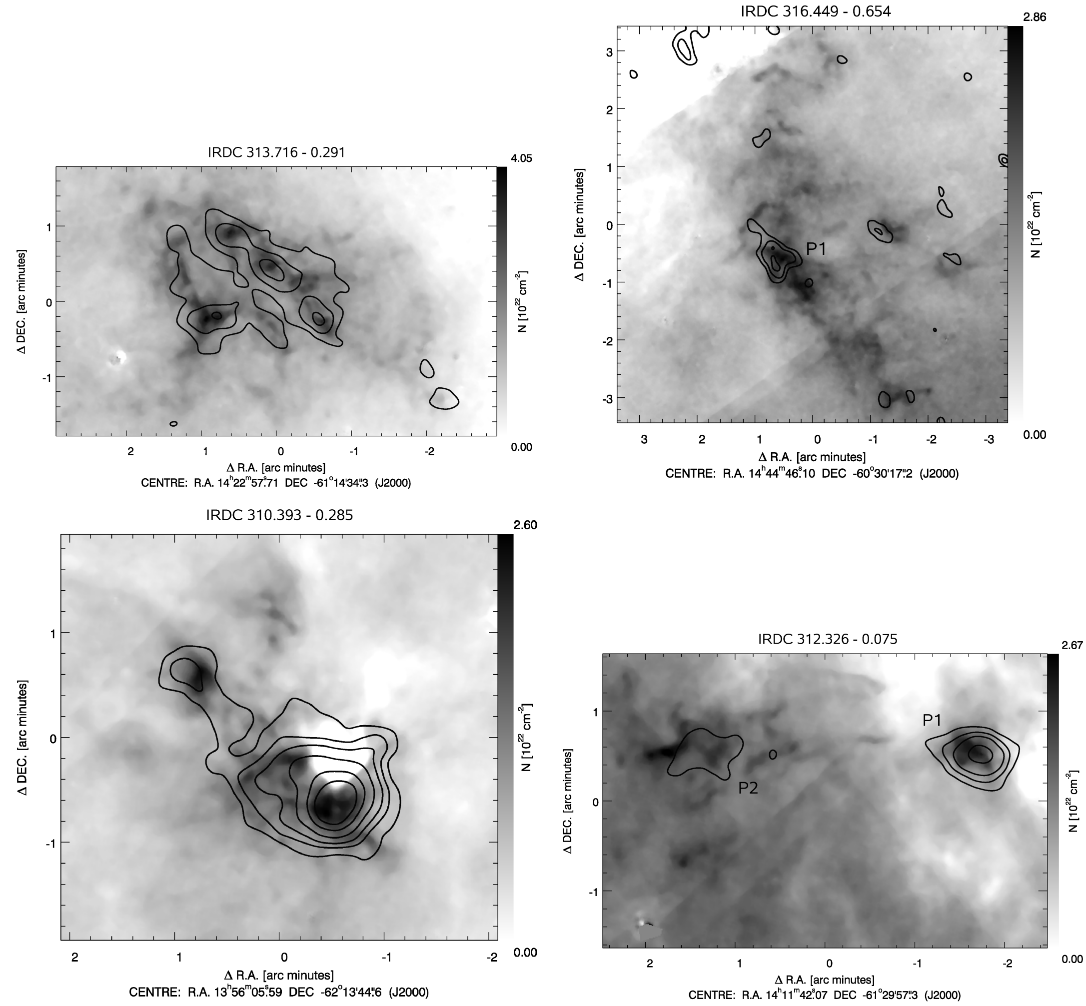

Figure 2.5 Column density maps derived from 8 μm extinction overlaid with 1.2 mm continuum emission as contours. The scaling is indicated in the bar to the right of each image. The contours are 60, 108, 156, 240, 360, 480 mJy beam^{-1} in all cases except for IRDC 316.45-0.65 which is 84, 120, 156, 240, 360, 480 mJy beam^{-1}.

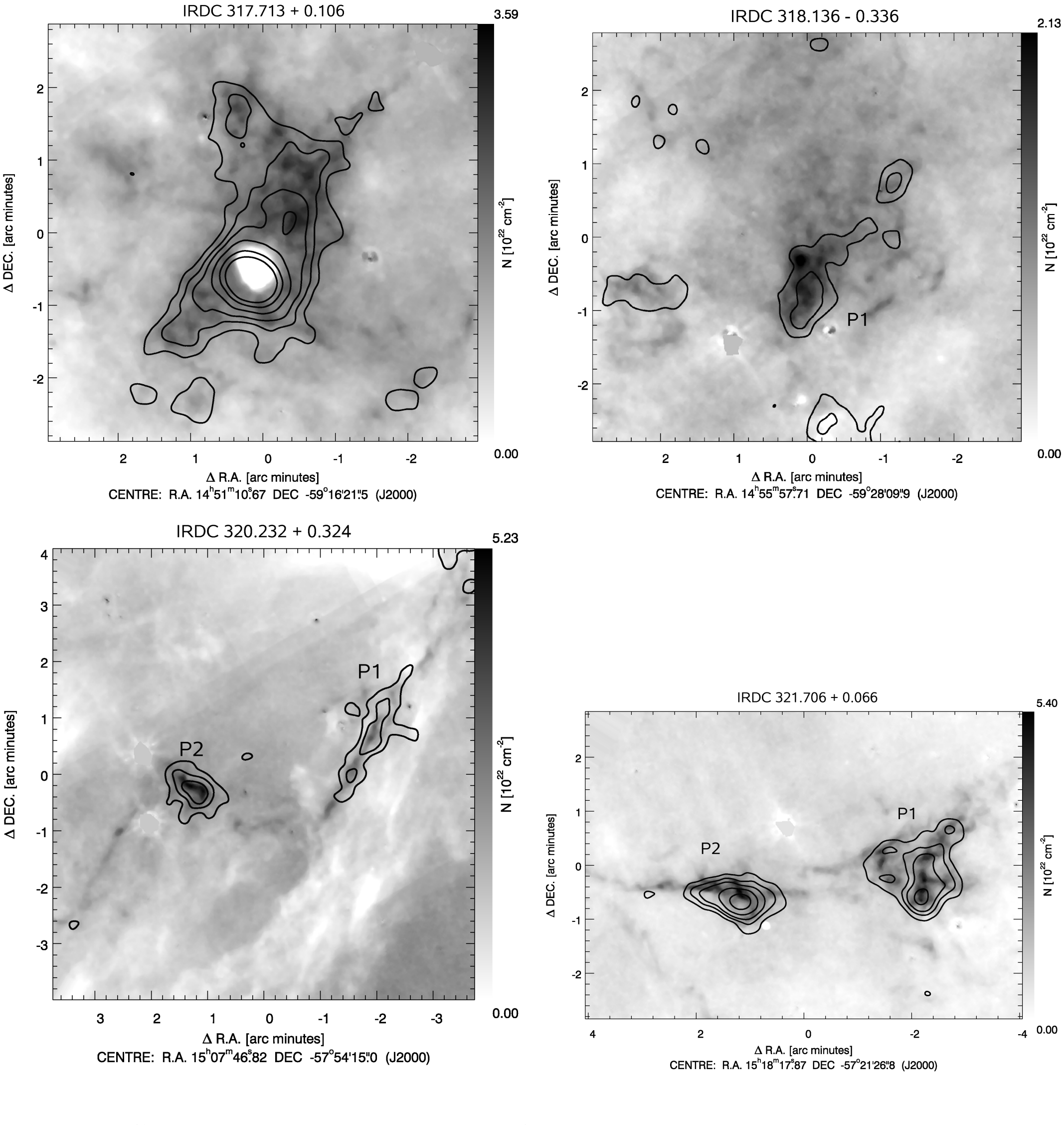

Figure 2.6 Column density maps derived from 8 μm extinction overlaid with 1.2 mm continuum emission as contours. The scaling is indicated in the bar to the right of each image. The contours are 60, 108, 156, 240, 360, 480 mJy beam^{-1} in all cases.

maps of extended emission and absorption structures, and finally column density maps could be extracted in a subsequent step.

Dust masses for the IRDCs were computed by assuming that they are in the foreground and attenuate emission from behind. The optical depth τ is ideally the logarithm of the ratio of two fluxes: (a) the flux from the emission background $I_{\rm back}$ directly behind the IRDC, and (b) the actually measured remnant flux $I_{\rm IRDC}$ from the location of the IRDC. Furthermore, superimposed on the IRDC is an emission contribution from foreground material, $I_{\rm fore}$, which must be subtracted. Since $I_{\rm back}$ cannot be estimated directly, we need a measurable quantity I_0 that can be used as a proxy for $I_{\rm back}$. The optical depth is then given by

$$\tau = \ln\left(\frac{I_0 - I_{\rm fore}}{I_{\rm IRDC} - I_{\rm fore}}\right) \tag{2.3}$$

Following Peretto et al. (2008), we assume that $I_{\rm fore} = I_{\rm zl}$, where $I_{\rm zl}$ is the zodiacal light, which is calculated systematically for every Spitzer observation and available in the image header. For the quantity I_0, we used the average emission level from a patch of MIR emission in the close vicinity of the actual cloud. These emission patches, typically around 1 square arcminute in size, were chosen manually to capture the characteristic emission level for the background approximation of the individual clouds and to exclude strong compact emission sources. The mean and standard deviation of the emission levels within these defined regions were computed to be used as I_0 in Eq. 2.3. The standard deviation obtained here is propagated in the following steps and used to provide formal errors for the derived masses and column densities, as listed in Table 2.3.

After optical depth determination, this quantity is converted into column densities and finally to masses by using the following equations:

$$N_{\rm H_2} = 1.086 \frac{\tau}{\sigma}, \tag{2.4}$$

$$M = {\rm m_{H_2}} \;\; A \;\; N_{\rm H_2}, \tag{2.5}$$

where $N_{\rm H_2}$ is the H_2 molecule column density, ${\rm m_{H_2}}$ is the mass of one hydrogen molecule, A is the area per pixel, and σ is the extinction cross–section per hydrogen molecule. According to the adopted dust–extinction model by Weingartner & Draine (2001, see below), $\sigma = 4.62 \times 10^{-23}\,\mathrm{cm}^2$ for the Spitzer/IRAC band 4 central wavelength of 7.87 μm.

The derived masses depend critically on the adopted extinction–column density calibration, the distance to the targets, and the method for selecting the relevant extinction regions. As a dust model, we used the parametrisation of Weingartner & Draine (2001) for their model B with $\mathrm{R_V} = 5.5$. This particular model was shown to be relevant for massive star–forming regions, e.g., by Indebetouw et al. (2005). It differs from the common dust models (e.g., Draine & Lee, 1984) in that it predicts higher extinction cross–sections particularly for the 4–8 micron wavelength region, a relevant point for the Spitzer extinction maps. We note that these elevated cross–sections are also predicted in connection with ice-coated dust grains and especially if dust coagulation processes are involved (Ossenkopf & Henning, 1994). The chosen dust model finally relates the optical depth (and, equivalently, the extinction magnitude at the used wavelength) to the equivalent column density of hydrogen molecules. The quadratic dependence of the masses on the distance is in the extinction map case the same as for masses derived from the 1.2 mm emission data.

2.3.3 Comparison of techniques

Using the data from two different regions of the spectrum and two different techniques for estimating IRDC parameters, enables us to compare the results and to analyse advantages and disadvantages of both methods (see Table 2.1). The mid-IR data have an effective resolution of around 3″, which is much higher than 24″ for our millimeter data. The estimated total masses and peak column densities have no dependence on the temperature. On the other hand, when using 8 μm data to calculate the optical depth and then the column density in the cloud, we have to estimate the expected flux from the background indirectly. We assume the background flux to be the difference between the average intensity around the cloud and the foreground intensity, although in reality matter hidden by the infrared dark cloud can be inhomogeneous and of either lower or higher intensity. However, the logarithm in Eq. (2.3) to a certain degree mitigates uncertainties in the estimation of the intensities necessary for evaluating Eq. (2.3).
Simon et al. (2006a) used an automated approach where they strongly smoothed the original (MSX) mid-infrared images and basically used these smoothed data to approximate for the quantity I_0 (cf. Eq. 2.3). We tested this approach for one of our

Table 2.1. Comparison of the 1.2 mm emission and 8 μm absorption techniques for deriving masses and column densities.

Properties	1.2 mm	8 μm
Properties	1.2 mm	8 μm
Distance dependence[a]	+	+
Resolution	24″	3″
Sensitive to lower column density filigree structure	-	+
Temperature dependence	+	-
Background and foreground estimation	not necessary	necessary
Sensitive to column densities $\gg 10^{23}\,\mathrm{cm}^{-2}$	+	-

[a] Only for masses

Table 2.2. Comparison of the different observational techniques for IRDC 18223-3.

Data	Resolution (arcsec)	Column density (10^{22} cm $^{-2}$)	Optical depth at 8 μm	Contrast (I_{bg}/I_{IRDC})
8 μm GLIMPSE	3	2.3	0.95	2.5
1.2 mm IRAM[a]	11	5.9	2.4	11
3.2 mm PdBI[b]	5.8 × 2.4	45	19	1.8e+08
1.3 mm SMA[c]	1.3 × 1.4	93	40	1.8e+17

[a] Beuther et al. (2002)

[b] Beuther et al. (2005)

[c] Fallscheer et al. (2009)

clouds but found that unless large smoothing kernels were used, the herewith derived intensity contrasts were systematically smaller than for the method that we employed (Sect. 2.3.2). For very large smoothing kernels ($> 10'$), it is very difficult to control the process. Continuum emission from strong extended emission sources in the surroundings might be folded into the area of the IRDCs, depending on the individual circumstances. Therefore, we refrain from using this smoothing approach to achieve stronger control on the estimation of the quantity I_0.
Uncertainties in the foreground level estimation also affect the resulting masses and column densities. At the moment, we take into account only the zodiacal light contribution, which typically accounts for 15%–20% of the intensity toward the IRDCs. An extreme (hypothetical) case may be that all remaining flux received from the IRDC to the noise level $I_{\rm noise}$ of the GLIMPSE images is produced by another foreground emission contribution (e.g., the PDR surface of the cloud, glowing in PAH emission). After removing all this emission down to $I_{\rm noise}$, the resulting intensity contrast would of course be clearly higher. However, considering typical levels of $I_{\rm noise}$ and $I_{\rm Back}$, our results for the column densities would rise by just a factor of around 3. This is again due to the alleviating effect of the logarithm in Eq. (2.3), acting on the intensity contrast.

While for almost all of our clouds, peak column densities extracted from the GLIMPSE data are slightly higher than the values derived from the millimeter data, this difference does not correspond to the factor of 8 in resolution. Therefore, we compared the peak column densities extracted from different observational data for the previously studied IRDC 18223-3 (Beuther et al., 2002, 2005), located 3.7 kpc from us with a NH_3 rotation temperature of ~ 33 K (Sridharan et al., 2005). For this particular cloud, 1.2 mm IRAM single-dish observations (Beuther et al., 2002), 8 micron Spitzer/GLIMPSE data, and interferometric data at 3.2 and 1.3 mm data obtained with the PdBI and SMA (Beuther et al., 2005, Fallscheer et al. 2009 in prep.) are available, the spatial resolution ranging between 11 arcsec and 1.4 arcsec (Table 2.2). For the GLIMPSE data, we obtained a column–density distribution map according to the algorithm described in Sect. 2.3.2. Together with the 1.2 mm IRAM data shown as contours, this result is presented in Fig. 2.7. The peak column densities for all the millimeter data were calculated using Eq. (2.2), adopting the different beam sizes, and a temperature of 33 K (Sridharan et al., 2005) was always used. The peak flux density for the 3.2 mm PdBI data was taken from the corresponding paper (Beuther et al., 2005), while we

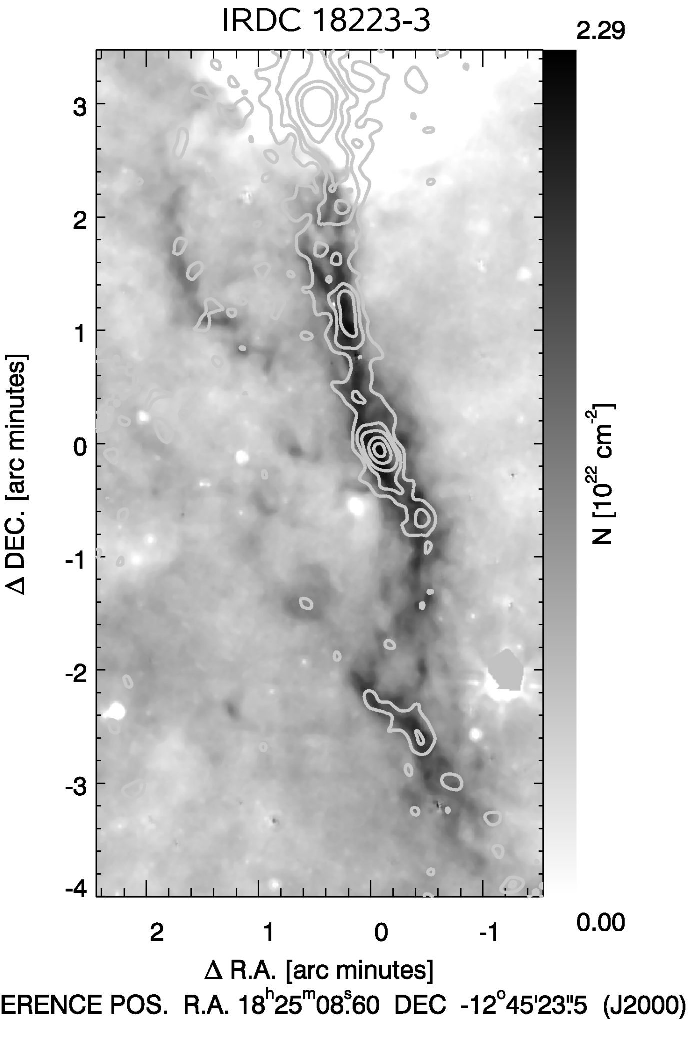

Figure 2.7 Column density map derived from an 8μm Spitzer/GLIMPSE image overlaid with 1.2 mm IRAM continuum emission as contours. The image scaling is indicated in the sidebar. The contours are 38,76,114,190,266 mJy beam^{-1}. The (0,0) position corresponds to the center of the IRDC 18223-3.

(re-)assessed the peak flux densities for the IRAM[1] and SMA data on the related FITS files, kindly provided by H. Beuther and C. Fallscheer. For the dust opacity per gram of dust, as for our SIMBA millimeter data, we always used the same opacity model, appropriate for coagulated dust particles with thin ice mantles (Ossenkopf & Henning, 1994, opacity column 5 in their Table 1). As we can see in Table 2.2, the peak column density derived from the high-resolution millimeter interferometry data is a factor of 40 higher than the one extracted with the mid-IR technique. A factor of a few between the mid-infrared and the millimeter single-dish results for the peak column densities can be accounted for by using other dust opacities/extinction cross sections or more extreme assumptions about the MIR foreground contribution (see above). However, the large difference between the mid-infrared and the millimeter interferometry results indicates a principle limitation of the extinction method in identifying high column density peaks. The realistically attainable intensity contrast at high optical depths determines this limit. In Table 2.2, we list the optical depths and image contrasts at 8 micron that would correspond to the column densities derived from the millimeter data. Obviously, realistic 8 micron images cannot provide such humongously high dynamic ranges required to derive column density levels similar to the interferometry results.

2.4 Results

2.4.1 Morphology of the IRDCs

The morphology of the clouds in our sample range between compact structures (IRDC 312.33-0.07 P1 and P2) and filaments (IRDC 309.13-0.15). They have sizes from $1'$ (IRDC 013.84-0.49 P2 and P3) to $4'$ (IRDC 317.71+0.11), which corresponds to roughly 1–3.5 pc at the distance of these clouds. There is, in general, good agreement between the morphologies of the 1.2 mm emission and the 8 μm extinction structures (see Fig. 2.4-2.6). As a rule, dense areas of extinction material (IRDCs 013.84-0.49, 313.72-0.29 etc.) coincide with relatively bright compact sources at 1.2 mm. For some IRDC complexes, some *emission* peaks at the millimeter wavelengths are associated with mid-IR *emission* sources (IRDCs 309.13-0.15 P2, 309.34-0.64 P2 and 317.71+0.11), which

---

[1] The 1.2 mm peak flux density we find in the IRAM 30-m data is clearly higher than reported in Beuther et al. (2002). In that paper, the millimeter peaks had been fitted with Gaussians which occasionally underestimated the true peak flux densities.

implies that they represent later evolutionary stages than those objects corresponding to 8 micron extinction. Among all clouds there is one particular case, IRDC 310.39-0.28, where the millimeter emission still peaks at the extinction maximum, despite the existence of a bright nearby MIR emission source.[1] The IRDCs 013.84-0.49, 312.33-0.07, 318.13-0.34, 320.23+0.32, and 321.71+0.07 exhibit several separated sources at mm wavelengths, coinciding with dense 8 μm features. We note that IRDC 308.12-0.33 has an elongated shape and three recognizable substructures, one of them corresponding to the extinction maximum at mid-IR wavelengths. IRDC 309.13-0.15 shows two distinct 1.2 mm emission sources, a compact object (P1) coinciding with the MIR extinction region, and another (P2) that has an emission peak corresponding to the 8 μm emission and an elongated tail. Extended millimeter emission, $2' \times 4'$ in size, with at least four substructures is present in IRDC 313.72-0.29. For IRDC 316.45-0.66, we can recognise only one weak 1.2 mm source and diffuse, extended MIR extinction structures.

The positions of known IRAS sources are marked with plus-signs in Figs. 2.1–2.3, where the IRAC 8 μm data are displayed as inverted greyscale images, and contours present the 1.2 mm data. In general, IRAS sources do not correspond to the extinction regions at 8 μm. In contrast, they agree with the locations where MIR emission coincides with millimeter emission peaks or just with the very bright MIR emission sources. In the case of IRDC 317.71+0.11, the kinematic distance to one of the IRAS sources, located at the center of the 8 μm emission, can be derived using the CS (2–1) line velocities reported by Bronfman et al. (1996) toward this IRAS source. The $v_{\rm LSR}$ velocities of this CS measurement and our HCO$^+$ data for the neighbouring IRDC differ by less than 0.5 km/s. The distance to the cloud and the IRAS source is then around 2.9 kpc. Hence, assuming that the dark cloud is related to this IRAS point source, the infrared luminosity of the compound (IR source + IRDC) is $\approx 10^4$ L$_\odot$, using the IRAS approximation formula from Henning et al. (1990), which is the typical luminosity of pre-main-sequence OB stars.

2.4.2 Masses and column densities

Millimeter continuum emission was detected toward all 12 clouds and column density maps were extracted from 8 μm images by using the algorithm described in Sect. 2.3.2.

---

[1] Based on the similar LSR velocities for the MIR source and the extinction region, derived from our recent molecular line observations, both objects are probably associated.

Figures 2.4-2.6 present the column density maps of every region, superimposed on the corresponding 1.2 mm contours. In Table 2.3, the properties of the IRDCs are compiled: name, right ascension, declination, distance, peak flux density, integrated flux density, mass and peak column density of the 1.2 mm sources, and mass and peak column density of the extinction matter. For every cloud in the table, the first line corresponds to the total millimeter flux density as well as the total masses of the emission and extinction matter. The following lines present data for the separate millimeter subclumps, which are labeled with P.

Where appropriate, we distinguished between the separate subclumps at 1.2 mm. In Figs. 2.4-2.6 and Table 2.3, these separate emission sources are named with the designation "P" (e.g. P1, P2). For all of them, we measured peak flux density and integrated flux density, derived masses, and column densities according to Equs. 2.1 - 2.2. In the case of IRDCs 309.13-0.15 (P2), 309.34-0.64 (P2), and 317.71+0.11 (P1) the parts coinciding with strong 8 μm emission features were not taken into account when measuring 1.2 mm flux densities and hence for estimating masses and column densities. The typical range of masses of the separate millimeter sources with $T = 20$ K was 50-1000 $M_\odot$, and the column density range between 0.9 and 4.6 $\times 10^{22}$ cm^{-2}.

In calculating the total masses of the extinction material in individual clumps, we considered regions above 3 sigma, where sigma is in this case the standard deviation in the full extinction maps. The total masses of the IRDCs for extinction matter were found to range from 300 to 1700 $M_\odot$ and the derived peak column densities correspond to values from 2.1 to 5.4 $\times 10^{22}$ cm^{-2}.

2.4.3 Comparison with results for other cores

We compare our results with previously obtained characteristics for low- and high-mass pre-stellar cores.

Comparison with low-mass cores

Extinction mapping has been applied mainly along the lines of the near-infrared colour excess method (e.g., Lombardi, 2008; Lombardi & Alves, 2001) or classical star–count–techniques in the visible or near-infrared (e.g., Dobashi et al., 2005; Froebrich et al., 2005). These approaches are most powerful towards medium-extinction regions. In contrast, the extinction–map method used in the current paper exploits the extinction of mid-infrared extended emission and hence does not rely on the identification

Table 2.3. Properties of the IRDCs.

Name	R.A. (J2000.0)	Decl. (J2000.0)	D (kpc)	I_{Peak} (mJy)	I_{Int} (Jy)	Mass 1.2mm ($M_\odot$)	N (1.2 mm)[1] (10^{22} cm $^{-2}$)	N_0 (1.2 mm)[2] (10^{22} cm $^{-2}$)	Mass (8 μm) ($M_\odot$)	N (8 μm) (10^{22} cm $^{-2}$)
IRDC 308.12−0.33	13 37 01.2	−62 44 40	4.32	225	1.88	580	1.7	60.3	520^{+40}_{-30}	$2.8^{+0.16}_{-0.16}$
IRDC 309.13−0.15	13 45 17.1	−62 21 57	3.92	330[3]	4.39[3]	1150[3]	2.6[3]		1750^{+370}_{-310}	$3.0^{+0.13}_{-0.13}$
P1				162	1.37	360	1.3	41.9		
P2				124	0.96	250	0.9			
IRDC 309.34−0.64	13 48 39.8	−62 47 26	3.46	504[3]	3.69 [3]	750[3]	3.9[3]		750^{+170}_{-150}	$3.1^{+0.24}_{-0.24}$
P1				216	0.94	190	1.7	48.5		
P2				155	0.81	170	1.3			
IRDC 310.39−0.28	13 56 01.7	−62 14 27	4.93	594	2.48	1029	4.6	186.1	1320^{+60}_{-50}	$2.6^{+0.16}_{-0.16}$
IRDC 312.33−0.07	14 11 56.8	−61 29 25	4.05	288	0.77	210	2.3	76.6	290^{+100}_{-60}	$2.7^{+0.33}_{-0.16}$
P1				288	0.46	130	2.3			
P2				92	0.31	90	0.7			
IRDC 313.72−0.29	14 23 05.4	−61 14 48	3.33	172	1.98	370	1.3	35.7	700^{+90}_{-70}	$4.1^{+0.16}_{-0.16}$
IRDC 316.45−0.66	14 44 50.4	−60 30 54	3.01	159	0.96	150	1.3	32.3	430^{+80}_{-70}	$2.9^{+0.16}_{-0.16}$
P1				159	0.58	90	1.3			
IRDC 317.71+0.11	14 51 07.5	−59 16 11	2.9	954[3]	8.00[3]	1150[3]	7.5[3]		1320^{+150}_{-150}	$3.6^{+0.15}_{-0.15}$
P1				250	1.98	280	2.0	47.9		
IRDC 318.13−0.34	14 55 58.4	−59 28 31	2.96	142	2.48	370	1.1	26.9	680^{+160}_{-140}	$2.1^{+0.16}_{-0.16}$
P1				142	1.02	150	1.1			
IRDC 320.23+0.32	15 07 56.7	−57 54 27	1.97	186	1.68	110	1.5	24.6	600^{+320}_{-250}	$5.2^{+0.16}_{-0.16}$
P1				142	1.00	70	1.1			
P2				186	0.68	50	1.5			
IRDC 321.71+0.07	15 18 26.7	−57 21 56	2.14	408	3.12	240	3.2	56.9	$460\ ^{+80}_{-80}$	$5.4^{+0.16}_{-0.23}$
P1				276	1.69	130	2.2			
P2				408	1.43	110	3.2			
IRDC 013.84−0.49	18 17 21.2	−17 09 23	2.66	438	9.38	1130	3.5	77.0	1150^{+130}_{-120}	$3.3^{+0.13}_{-0.13}$
P1				214	2.97	360	1.6			
P2				163	1.12	130	1.3			
P3				192	1.45	170	1.5			
P4				438	3.54	430	3.5			

[1] Peak column density per beam

[2] Extrapolated column density, obtained by applying the correction factor explained in Sect. 2.4.3

[3] This mm peak corresponds to a mid-infrared bright source near to the IRDC.

of stellar background sources. This method can peak into cores of column densities as high as 10^{23} cm^{-2}. It was used in the analysis of low-mass starless cores based on ISOCAM data (Bacmann et al., 2000), which provides an opportunity to compare our results. To compare fairly, two effects must be considered: **(a)** Bacmann et al. (2000) used the standard Draine & Lee (1984) extinction cross sections. These are more than a factor of 3 smaller than the Weingartner & Draine (2001) values we use. We therefore recomputed the peak column densities reported in Bacmann et al. (2000) for the low-mass cores by adopting the Weingartner & Draine (2001) dust–extinction model; and **(b)** for the low-mass cores, which typically reside at distances of less than 300 pc, the linear spatial resolution is much better than in the case of IRDCs with their distances of 2 - 5 kpc. Therefore, the true column density peaks are more sharply resolved in the low-mass case. To assess the effect of poor spatial resolution on our derived peak column densities, we used a synthetic column density map derived in Steinacker et al. (2005) for one of the low-mass cores of Bacmann et al. (2000), namely Rho Oph D (d = 160 pc). We convolved this map with kernels appropriate for emulating the much coarser linear resolution toward our IRDC targets and computed the ratio of the unsmoothed to the smoothed peak column density value. These factors (typically in the range from 1.5 to 3.5) were multiplied by the peak column densities we have originally derived from the IRDC extinction maps.

A comparison between the column densities for low-mass cores and our IRDCs, after taking into account the afore mentioned considerations (a) and (b), is shown in Fig. 2.8. We can see a clear trend of high-mass cores having higher column densities than low-mass objects. This qualitative difference shows that IRDCs are not just distant Taurus-like clouds, but a distinct type of clouds with the potential of forming a distinct type of stars (see below and Sect. 2.4.4).

In step (b), we note that we applied a correction factor that increases the column densities with increasing kinematic distance. To fortify statistically our statement that Infrared Dark Clouds have “stochastically larger” values of column densities than low-mass pre-stellar cores, we used the (Wilcoxon)-Mann-Whitney U one-tailed test (e.g., Wall & Jenkins, 2003). It is a non-parametric test for assessing whether two samples of observations originate in the same distribution or not. It operates well for a small number of observations in one sample. The null hypothesis is that the two samples are drawn from a single population. For the test, we used low-mass column density values from Bacmann et al. (2000) adapted to the Weingartner & Draine (2001) dust extinction model and column densities for IRDCs *without* applying the linear spatial–resolution correction (b) mentioned above.

For both populations, we computed the Rank Sum within the nonparametric Mann-Whitney statistic, usually called U (108 versus 0). The distribution of the U-statistic for the null hypothesis is known and can be found in special tables (e.g., Siegel & Castellan, 1988). We then estimated the probability that the values for low-mass objects and IRDCs originate in the same distribution. The derived probability of lower than 0.005 rejects the null hypothesis and demonstrates that our two samples come from different distributions.

Comparison with high-mass cores

The high-mass clumps that we want to compare have all been observed at 1.2 mm, and comprise the following samples: high-mass starless–core candidates (HMSCs) (Beuther et al., 2002; Sridharan et al., 2005), Infrared Dark Clouds from Rathborne et al. (2006), and results presented in this paper for our 1.2 mm data. To (re-)calculate peak column densities for the first two sets of data, we also used Eq. (2.2). In the case of HMSCs, peak flux densities were taken from Beuther et al. (2002), and distance and temperature estimates for all these objects come from Sridharan et al. (2005). In Rathborne et al. (2006), peak flux densities and distances for all 38 IRDCs are presented. For the calculation, we assume again 20 K for the temperature, and as dust opacity $\varkappa_v$ and gas-to-dust mass ratio we adopt the values 1.0 $\text{cm}^2\ \text{g}^{-1}$ and 100, respectively. Hence, we use the same parameters as for the analysis of our 1.2 mm data, except for the different beam size, which equals $(11'')^2$ in steradians, adapted to the IRAM 30-m telescope.

The measured data remain affected by the convolution with the observational beam, which results in different linear smoothing scales for objects at different distances. To eliminate this smoothing effect, we attempted to extrapolate the measured peak column densities per beam back to their true values, assuming an (analytic) column density profile. But what is an appropriate choice for such a power law? A first idea is to use the data at different beam sizes that we have for IRDC 18223-3 (Sect. 2.3.3). However, it turns out that these data sets provide no unique trend for such a power law. The comparison between the IRAM 30-m data and the SMA data imply a relatively steep power law of $N \sim \text{r}^{-1.75}$, and the comparison with the PdBI data would even indicate a much steeper power law index. The fact that these two data sets do not result in a similar power law may be related to the different degrees to which these observations are able to recover extended emission. Furthermore, at the high spatial resolution of the SMA observations, we begin to see a dense rotation structure (Fallscheer et al. 2009, in prep.) that is distinct from the remainder of the surrounding clump. However, we also compared the column density values of a few other IRDCs, observed both at single-dish and interferometric resolution (Rathborne et al., 2006, 2008). Again, no clear trend for a certain power law range is obvious. According to Johnstone et al. (2003), the column density profile of the filament structure of the famous IRDC G11.11-0.02 should be very steep and may reach $\sim \mathrm{r}^{-3}$. Such a significant difference to commonly observed values might be an additional feature characterizing massive star–forming clumps, especially if filamentary structures are involved. On the other hand, Bacmann et al. (2000) showed that $\mathrm{N} \sim \mathrm{r}^{-1}$ can be a reasonable choice for lower-mass starless cores, and also the single dish mapping of young massive clumps by Beuther et al. (2002) resulted in less steep power laws for the column density quite close to the low-mass core results. Hence, by assuming $\mathrm{N} \sim \mathrm{r}^{-1}$ in extrapolating the true column densities, we can obtain a robust lower limit.

To recalculate all column density values, an artificial column density distribution map was created (by just assuming an analytical $\mathrm{N} \sim \mathrm{r}^{-1}$ profile) with a peak in the centre of the array normalised to 1.0 and the assumption that 1 pixel corresponds to 2000 AU (a typical length scale for fragmentation). Then, for every source from the three high-mass samples mentioned above, this column density distribution map was convolved with a smoothing Gaussian kernel emulating the effect of observing at mm wavelengths with single-dish telescopes (11–24$''$ beam). The kernel size (FWHM) is computed by taking the ratio of the effective linear resolution (in AU) achieved within the observed mm maps to the 2000 AU pixel size from the artificial map. After convolving the artificial map with such a Gaussian kernel, the peak column densities in these synthetic maps become smaller than 1. The correction factor for every source is then the ratio of the original peak column density value (1.0) to the peak column density value after beam convolution. These factors are then applied to the column density values derived according to Eq. (2.2), which then approximates the true peak column density values. These extrapolated values for the new regions reported here are also given in Col. 9 of Table 2.3.

Figure 2.9 summarizes the distribution of the extrapolated peak column densities that we finally obtained. The distribution of the true peak column densities indicates a similar order of magnitude for previously obtained values for the two other samples of massive star–forming regions and our new SIMBA results. Most of the clouds have (extrapolated) column densities in the range from 1.0 to 12.0 $\times 10^{23}$ cm^{-2} with few exceptions reaching 20.0 - 30.0 $\times 10^{23}$ cm^{-2}.

2.4.4 Comparison with theoretical models.

Infrared Dark Clouds, located several kpc away from us, have high masses, volume and column densities, but "high" values alone do not guarantee that they are really the progenitors of massive stars, and we need additional criteria to estimate this possibility. According to Krumholz & McKee (2008), only clouds with column densities of at least 1 g cm^{-2}, which corresponds to 3 $\times 10^{23}$ cm^{-2} in our units, can form massive stars. As we can see in Table 2.3, the direct transformation of observational results for IRDCs from our list indicates peak column densities one order of magnitude lower than this limit. On the other hand, it was shown in Sect. 2.4.3 that the directly–observed peak column densities are still affected by the convolution with the beam of the millimeter observations. After taking this into account, the derived values of the extrapolated column density increase by a factor of 10 or higher (see Fig. 2.9). We can thus, reach the 3 $\times 10^{23}$ cm^{-2} threshold in the case of the infrared dark clouds.

Since we observe not only compact sources, but also very filamentary structures such as IRDC 320.23+0.32 P1, this raises the question, of whether it is possible to form massive stars in these structures. Banerjee & Pudritz (2008) demonstrated that filaments play a dominant role in controlling the physics, accretion rate, and angular momentum of the far smaller-scale accretion disk that forms within these collapsing structures. Large-scale filamentary flows sustain a high accretion rate ($\dot{M} \sim 10^{-2}$ M$_{\odot}$ yr^{-1}) due to the supersonic gas flow onto the protostellar disk. These rates are 10^3 times higher than predicted by the collapse of the singular isothermal spheres and exeed the accretion rates necessary to squeeze the radiation field of the newly–born massive star. Thus, for almost all our clouds, we confirm the possibility of forming massive stars.

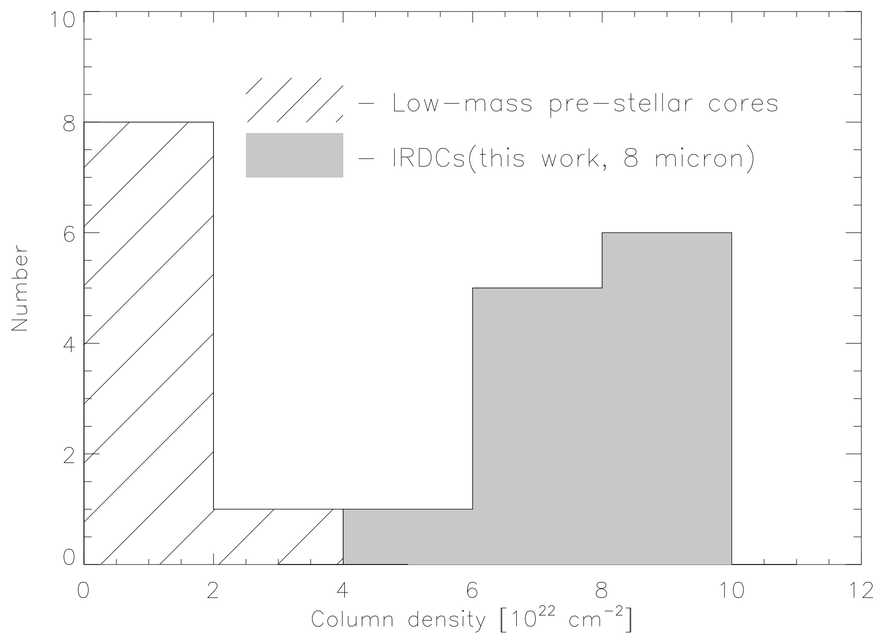

Figure 2.8 Histogram showing the principle distribution of column densities for a collection of low-mass cores from Bacmann et al. (2000) (after taking into account consideration (a) from Sect. 2.4.3) and for the IRDCs presented here (after taking into account consideration (b) from Sect. 2.4.3). The Mann-Whitney-U one-tailed test confirms the clear separation of the two distributions even when the different spatial resolutions (consideration (b)) are not taken into account (Sect. 2.4.3).

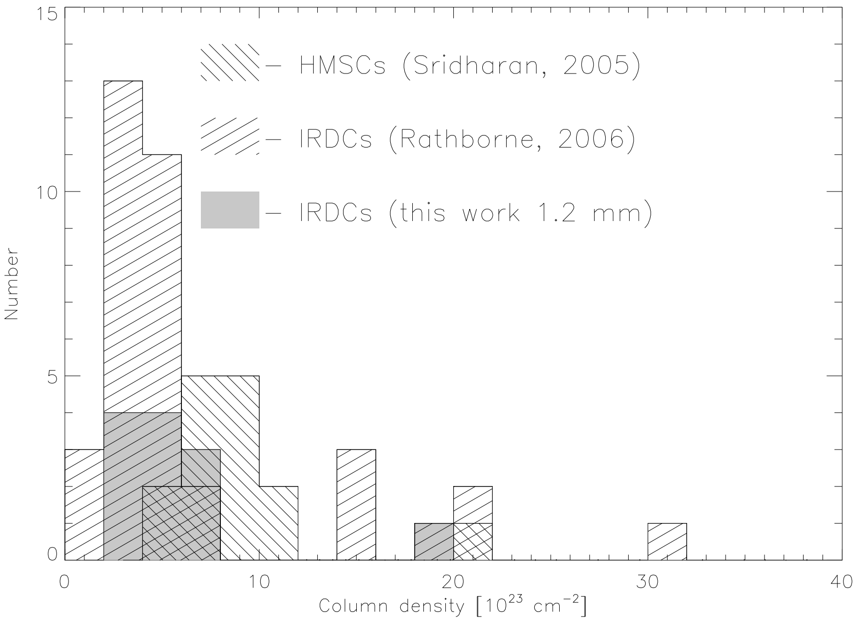

Figure 2.9 Distribution of extrapolated column densities for the HMSCs from Sridharan et al. (2005), the IRDCs from Rathborne et al. (2006), and the IRDCs from the present paper. Note that we have applied the corrections and extrapolations mentioned in Sect. 2.4.3 for all these high-mass cores.

2.5 Conclusions

We have discussed our progress in understanding the properties of Infrared Dark Clouds. A set of 12 clouds located in the southern hemisphere has been selected from the MSX 8.3 micron images. For these clouds, 1.2 mm maps were obtained with the SIMBA bolometer array at the SEST telescope. GLIMPSE mid-infrared images of these regions were retrieved from the Spitzer Archive.

The new sources exhibit a variety of IRDC morphologies, from compact cores to filamentary shaped ones, from infrared quiet examples (no Spitzer 8 μm emission sources) to more active ones. As a rule, our sample shows good agreement between the morphologies of 1.2 mm emission and 8 μm extinction features. The total masses of the IRDCs were found to range from 150 to 1150 $M_\odot$ (emission data) and from 300 to 1750 $M_\odot$ (extinction data). We derived peak column densities of between 0.9 and 4.6 $\times 10^{22}$ cm^{-2} (emission data) and 2.1 and 5.4 $\times 10^{22}$ cm^{-2} (extinction data).

Since the MIR extinction method was used previously for the analysis of low-mass starless cores, we check how our findings relate to the published results. To complete a fair comparison, we used the same dust model and the same spatial resolution in both cases. It is shown, that there is a clear trend for the high–mass cores to attain higher column densities than the low-mass objects. This qualitative difference means that most IRDCs are not just distant Taurus-like clouds, but a distinct type of clouds with the potential to form a distinct type of stars. A simple statistical analysis (the Mann-Whitney-U one-tailed test) confirms this statement also when the different spatial resolutions are not taken into account and thus the IRDC column densities are underestimated.

Using the data from two different regions of the spectrum and applying two different techniques for estimating IRDC parameters enables us to compare these two methods. On the one hand, the extinction technique has some advantages over the millimeter technique. It is a cheap method since GLIMPSE at 8 μm has covered large parts of the Galactic plane in the 4th and 1st quadrant. The GLIMPSE data have a higher spatial resolution than millimeter single-dish data, which reveals the often filigree substructures of the clouds. Furthermore, this method does *not* depend on assumptions about the temperature of the IRDCs in estimating masses and column densities. However, our comparison shows that the extinction method has a principle limitation in distinguishing very high image contrasts and hence of identifying high column density peaks $\gg 10^{23}$ cm^{-2}. Hence, with the extinction method, we can estimate only a lower limit to the column density values, despite the high resolution. The limit is around $A_{\rm V} = 75$ mag when applying the Weingartner & Draine (2001) $R_{\rm V} = 5.5$ B extinction law (corresponding to roughly 200 mag when following the common $R_{\rm V} = 3.1$ extinction law reviewed in Mathis, 1990). High-spatial resolution (sub-)millimeter observations are hence crucial in assessing even higher column density ranges and to identifying the true column density maxima.

To compare column densities extracted with the emission method with previously obtained values for IRDCs and HMPOs, we extrapolated them back to the true peak column densities by assuming a column density profile of $\sim$ r^{-1}, and thus, mitigating the spatial resolution differences within the different samples. The distribution of the true peak column densities indicates a similar order of magnitude for our new SIMBA results and the two other samples of massive star–forming regions. Moreover, the true peak column densities exceed the theoretical limit of 3 $\times 10^{23}$ cm^{-2} (or 1 g cm^{-2}), which has been proposed as a means of identifying potentially high-mass star-forming clouds.

Thus, extracted values for masses and column densities both for emission and extinction matter show a clear difference between IRDCs and known low-mass pre-stellar cores, and confirm our assumptions that Infrared Dark Clouds can present the earliest stages of high-mass star formation.

3

Chemistry in infrared dark clouds

Based on *Chemistry in infrared dark clouds*, Vasyunina, T., Linz, H., Henning, Th., Zinchenko, I., Beuther, H., Voronkov, M. submitted to Astronomy and Astrophysics

3.1 Introduction

In this chapter we go further toward the understanding of the nature of the IRDCs and present our investigations of the chemical composion of southern clouds.

Carey et al. (1998) and Pillai et al. (2006a) mention a difference in the ammonia and formaldehyde abundances and hence a possible chemical difference between low-mass pre-stellar cores and IRDCs. Later, Sakai et al. (2008), analysing the CCS and N_2H^+ abundance ratio, concluded that infrared dark clouds are chemically more evolved than low-mass starless cores.

To investigate the chemical composition of IRDCs and to check, if the molecular abundances in IRDCs are similar to the low-mass pre-stellar cores or not, we perform molecular line observations in the 3 mm band with the Mopra single-dish radio telescope. Combining molecular line data and H_2 column densities from the previous chapter we estimate molecular abundances and compare them with results for low-mass pre-stellar cores. Analysis of molecular lines provides not only information about chemistry, but also about physical processes in molecular clouds. For instance, the presence of SiO emission and HCO^+ extended wings are evidences for outflow activity in a cloud. Specific line shapes can indicate infall motion. The detection or non-detection of some species helps to determine the evolutionary status of our targets.

The chapter is organized in the following way. In Sect. 3.2 we describe our target selection, the selected molecular lines, observational and technical details. In Sect. 3.3 we present the results of the qualitative analysis of obtained molecular line spectra, line parameters and abundance estimates. We discuss the obtained results in Sect. 3.4 and conclude in Sect. 3.5.

3.2 Target and line selection, observations and data reduction

3.2.1 Target selection

A sample of 15 southern infrared dark clouds was selected by visual examination of the MSX 8.3 μm images for the presence of high-contrast dark clouds. 1.2 mm continuum data were obtained for these objects with the SIMBA/SEST telescope. Together with millimeter data we used 8 μm IRAC data from the Spitzer Galactic Legacy Infrared Mid-Plane Survey Extraordinaire (GLIMPSE, Benjamin et al., 2003) to investigate the physical properties of the extinction and emission material (see Vasyunina et al., 2009). Based on our millimeter and mid-IR data and taking into account single-dish beam sizes at millimeter wavelengths, we select several points for observations in every cloud. The criterion for selection was the presence of either a 1.2 mm emission peak, a 8 μm emission peak, or a 8 μm extinction peak. Such a criterion let us cover IRDCs at the different evolutionary stages. Millimeter emission and mid-IR extinction indicate the presence of cold gas, typical for more quiescent regions. A typical source of 8 μm emission usually contains a small infrared cluster and, therefore, is likely to be at a more advanced evolutionary stage than most dark regions in this IRAC band. The targets are listed in Table 3.1. 3-color Spitzer/GLIMPSE images of IRDCs together with the telescope and beam positions are presented in the on-line material Fig. B.1-B.3.

3.2.2 Line selection

In order to probe the dense and cold gas in IRDCs, we need appropriate tracers. The 3-mm band offers a large selection of molecular transitions. In particular, rotational transitions with low quantum numbers are accessible. In the following, we introduce the 3-mm lines we have chosen for our study.

N_2H^+: This species is known to be a selective tracer of quiescent gas (e.g., Caselli et al., 2002) and is particularly suitable for studying the structure and kinematics of cold star-forming cores. The hyperfine structure allows to reliably measure the optical depth. N_2H^+ is known to be a "late depleter", thus it is not strongly affected by freeze out on grain surfaces (which prevents the use of the more common CO or CS transition). This makes it a robust tool for scrutinizing the highly structured interiors of massive star–forming regions where warm massive protostars might co–exist with younger cold and massive cloud cores. N_2H^+ has been - detected in both low- and high- mass starless cores and infrared dark clouds (e.g., Fuller et al., 2005; Lee et al., 2001; Pirogov et al., 2003; Ragan et al., 2006).

^{13}CS: This molecule is a very good tracer of dense gas (e.g., Bronfman et al., 1996) due to its high dipole moment. It was detected in low-mass starless cores (e.g., Tafalla et al., 2002) and high-mass star forming regions (e.g., Jones et al., 2008). In contrast to N_2H^+, in cold dark clouds the CS emission vanishes toward the core center due to depletion, but can be used to trace layers surrounding the central cores.

CH_3CN: This molecule is considered to be a tracer of warm and dense regions (e.g., Araya et al., 2005; Kalenskii et al., 2000; Viti, 2005). Chemical models involving only gas phase reactions as well as models which take into account grain-surface chemistry, show that CH_3CN is only detectable in an environment with elevated temperatures (see Purcell et al. (2006) and references therein). It was detected in more evolved massive star-formation regions, like Sgr B2 (Jones et al., 2008) or G305.2+0.2 (Walsh & Burton, 2006), thus confirming the theoretical predictions. We include CH_3CN in our "cold-gas-survey", because among infrared dark points we have quite a significant number of regions, where star-formation processes might have already started.

HC_3N: This molecule belongs to an important group of interstellar molecules - the cyanopolyynes, $HC_{2n+1}N$. and is a valuable tracer of physical conditions in molecular clouds. Since its first detection in space (Turner, 1971) HC_3N has been found in every type of molecular cloud from giant molecular clouds associated with H II regions to circumstellar envelopes. It was shown that HC_3N transitions have low optical depth and indicate the presence of denser gas than other high density tracers (Bergin et al., 1996).

HNC: This molecule is a commonly used tracer of dense gas in molecular clouds. The abundance ratio HCN/HNC strongly depends on the temperature and in the case of the Orion molecular cloud decreases from 80 near the warm core to 5 on the colder edges (Goldsmith et al., 1986; Schilke et al., 1992). The recent theoretical work by Sarrasin et al. (2010) confirmed that this ratio should be around one for cold molecular clouds. This line is a triplet, but the spread of the hyperfine components is only 0.21 MHz or 0.4 km/s.

HCO^+ and $H^{13}CO^+$: HCO^+ is known to be a good tracer of the dense gas especially of embedded molecular outflows (e.g., Codella et al., 2001; Hofner et al., 2001). HCO^+ is an abundant molecule, with abundances especially enhanced around regions of higher fractional ionization. It is also enhanced by the presence of outflows where shock-generated radiation fields are present (Rawlings et al., 2004, 2000).

The emission from the $H^{13}CO^+$ isotopologue is mostly optically thin and traces similar gas densities as HCO^+. A comparison between the generally optically thick HCO^+ line and the optically thin $H^{13}CO^+$ line yields information on the bulk motion of the gas in the region.

HCN and $H^{13}CN$: This molecule has been suggested as ubiquitous high density gas tracer. Moreover, the HCN molecule is known to be a good tracer of infall motions in low-mass star-forming regions. However, for the high-mass cores this can be different. Here HCN may become an unreliable infall tracer because of a higher level of turbulence (Redman et al., 2008) and outflow signatures (Zhang et al., 2007).

HNCO: Zinchenko et al. (2000) showed that HNCO integrated intensities correlate well with those of thermal SiO emission in massive clouds. This can indicate a spatial coexistence of the two species and may hint to a common production mechanism, presumably based on shock chemistry.

C_2H: Chemical models predict that C_2H is only well centered on the sources when they are very young. At later stages it gets destroyed in the central cores, but is replenished in the outer shells (Beuther et al., 2008).

SiO: It can trace shocked gas potentially associated with energetic young outflows. Hence, this line can reveal star formation activity even for cores where no Spitzer/MIPS sources are apparent (e.g., Lo et al., 2007). For a few of our IRDCs we have indications from Spitzer/GLIMPSE imaging that shocked gas exists, often, but not exclusively, at the edges of the IRDCs. Tracers are the "green fuzzies" found in the 4.5 μm GLIMPSE channel (Chambers et al., 2009; Cyganowski et al., 2008) and generally attributed to pure rotational IR lines of H_2 (De Buizer & Vacca, 2010).

CH_3C_2H: A good tracer of dense gas appropriate for early stages of star forming regions (Bergin et al., 1994). This molecule can be used as a good thermometer in a dense environment.

The covered molecular lines and transitions are summarized in Table 3.2.

3.2.3 Mopra observations and data reduction

The observations were made with the 22-m Mopra radio telescope, operated by the Australia Telescope National Facility (ATNF), in the position switching mode. In total we spent 7 minutes on source and 7 minutes on the OFF position. Our targets are dense molecular condensations within larger molecular clouds with often widespread molecular emission. Therefore, we refrained from using one standard OFF position throw. Instead, OFF positions were chosen individually for every target region and were approximately 8-10′ away from the source.

The Mopra spectrometer (MOPS) offers zoom mode configurations with the possibility to observe up to 16 sub-bands of 138 MHz each within a total frequency range of 8.3 GHz. This set up delivers a velocity resolution of $\sim$ 0.11 km/s.

The observations were carried out on 9-11 May 2008 with the 3mm band receiver. We put the central frequency for the 8.3 GHz block to 89270 MHz and thus covered the range from 85 to 93 GHz. In this range we distributed 13 zoom windows, which covered the lines listed in Table 3.2.

System temperature measurements were performed every 30 minutes and a pointing scan every hour. Typical system temperatures (measured with the common chopper-wheel technique) during the observations were 170-210 K. At Mopra observatory, SiO masers are used to correct the telescope pointing, giving a pointing accuracy better than 10″. The main beam of the telescope varies between 36″ at 86 GHz and 33″ at 115 GHz and the main beam efficiency varies between 0.49 at 86 GHz and 0.44 at 100 GHz (Ladd et al., 2005)

Mopra data are originally stored in RPFITS format. Using the ATNF Spectral line Analysis package (ASAP), we transformed these raw data into ascii files which were then fed into GILDAS for further analysis. The typical rms level in the obtained spectra is about 0.12−−0.16 K. We give 1σ errors in Tables D-D.

Table 3.1. List of observed IRDCs.

Name	R.A. (J2000.0)	Decl. (J2000.0)	distance[a] (kpc)	T[c] (K)	N(H_2)[d] $*10^{22}$cm^{-2}	category[e]
IRDC308.13-1	13 37 01.582	-62 44 34.01	4.8	13.5	1.0	Q
IRDC308.13-2	13 37 00.418	-62 43 41.01	4.0	13.5	1.0	M
IRDC308.13-3	13 37 02.163	-62 43 39.01	4.0	13.5	1.0	M
IRDC309.13-1	13 45 17.521	-62 22 02.84	3.9	16.3	0.6	M
IRDC309.13-2	13 45 22.610	-62 23 27.48	3.9	14.7	0.5	M
IRDC309.13-3	13 45 16.775	-62 25 37.25	3.9	35.4	0.4	A
IRDC309.37-1	13 48 38.532	-62 46 17.55	3.4	31.4	0.9	A
IRDC309.37-2	13 47 56.116	-62 48 33.46	3.4	15.7	0.8	A
IRDC309.37-3	13 48 39.383	-62 47 22.39	3.4	15.7	0.7	Q
IRDC310.39-1	13 56 01.359	-62 14 18.29	4.2	27.4	1.2	A
IRDC310.39-2	13 56 00.759	-62 13 59.80	4.2	27.4	1.2	A
IRDC312.36-1	14 11 27.752	-61 29 27.18	4.5	13.5	1.1	A
IRDC312.36-2	14 11 56.773	-61 29 25.78	4.0	14.4	0.3	Q
IRDC313.72-1	14 22 53.158	-61 14 41.00	3.3	19.9	0.4	A
IRDC313.72-2	14 22 57.151	-61 14 10.84	3.3	19.9	0.4	A
IRDC313.72-3	14 23 02.720	-61 13 39.64	3.3	19.9	0.3	Q
IRDC313.72-4	14 23 04.533	-61 14 46.00	3.3	19.9	0.4	Q
IRDC316.72-1	14 44 19.000	-59 44 29.00	2.7	26.1	1.2	M
IRDC316.76-1	14 44 56.000	-59 48 08.00	2.7	22.6	4.1	A
IRDC316.72-2	14 44 15.400	-59 43 20.00	2.7	24.3	1.3	Q
IRDC316.76-2	14 45 00.500	-59 48 44.00	2.8	23.2	4.8	A
IRDC317.71-1	14 51 06.905	-59 16 11.03	3.0	15.6	1.2	Q
IRDC317.71-2	14 51 10.975	-59 17 01.73	3.0	16.6	3.5	A
IRDC317.71-3	14 51 19.667	-59 17 43.77	3.2	15.6	0.6	Q
IRDC320.27-1	15 07 56.251	-57 54 32.11	2.1	15.3	0.8	Q
IRDC320.27-2	15 07 31.616	-57 53 27.24	2.2	16.1	0.5	Q
IRDC320.27-3	15 07 35.077	-57 54 13.98	2.1	16.1	0.4	Q
IRDC321.73-1	15 18 26.387	-57 22 00.14	2.2	22.0	1.0	M
IRDC321.73-2	15 18 01.693	-57 22 02.00	2.2	11.7	1.7	M
IRDC321.73-3	15 18 01.065	-57 21 24.48	2.1	11.7	1.7	A
IRDC013.90-1	18 17 33.378	-17 06 36.70	2.5	12.9	2.6	M
IRDC013.90-2	18 17 19.350	-17 09 23.69	2.4	13.4	1.1	Q
IRDC316.45-1	14 44 51.515	-60 30 55.00	3.1	15.4	0.7	M
IRDC316.45-2	14 44 47.095	-60 31 30.89	3.1	14.2	0.5	M
IRDC318.15-1	14 55 57.704	-59 29 04.12	3.0	17.6	0.5	M

Table 3.1 (cont'd)

Name	R.A. (J2000.0)	Decl. (J2000.0)	distance[a] (kpc)	T[c] (K)	N(H_2)[d] $*10^{22}$cm^{-2}	category[e]
IRDC318.15-2	14 55 58.334	-59 28 30.52	2.9	17.6	0.4	Q
IRDC309.94-1	13 50 54.970	-61 44 21.00	5.3[b]	48.8	5.2	A

Note. — Columns are name, right ascension, declination, distance, kinetic temperature, H_2 column density and type according to mid-IR classification.

[a] At first, to estimate the kinematic distances to our IRDCs, we used HCO^+ line velocities (see Vasyunina et al., 2009). But more detailed investigation showed that HCO^+ lines, as a rule, have complex line shapes and the $v_{\rm LSR}$ positions can be shifted up to 2 km/s in comparison with its optically thin isotopologue $H^{13}CO^+$. We cannot use $H^{13}CO^+$ for distance determination, since it is much weaker and we detected it not in all cases. Thus, for distance determination we decided to use N_2H^+, which is optically thin and distinguishable for all regions except IRDC309.37-2. Despite the significant difference in velocities (up to 2 km/s) between HCO^+ and N_2H^+, the kinematic distances did not change drastically compared with the values in Vasyunina et al. (2009).

[b] From Saito et al. (2001)

[c] Temperatures were derived based on (1,1) and (2,2) ammonia transitions observed with the the 64-m Parkes radio telescope (Linz et al. in prep.).

[d] To estimate H_2 column densities in every point we used 1.2 mm data from SIMBA/SEST adopting the Mopra telescope beam size.

[e] ”A” indicates ”active” cores, ”M” - ”middle”, ”Q” - ”quiescent”.

Table 3.2. Observed molecular species.

Molecule	Transition	Rest frequency (GHz)	A ($*10^{-5}s^{-1}$)	g_u	E_u (K)	Comments
CH_3C_2H	5_3-4_3	85.442 600	0.129778	44	77.37	Tracer of dense gas,
	5_2-4_2	85.450 765	0.170373	22	41.22	good thermometer
	5_1-4_1	85.455 665	0.194760	22	19.53	
	5_0-4_0	85.457 299	0.202908	22	12.30	
$H^{13}CN$	1_1-0_1	86.338 735				Tracer of dense gas,
	1_2-0_1	86.340 167	2.8	9	4.14	infall motions
	1_0-0_1	86.342 256				
$H^{13}CO^+$	1-0	86.754 330	2.8	3	4.16	Tracer of dense gas
SiO	2-1	86.847 010	2.0	5	6.25	Trace shoked gas
C_2H	1-0 3/2-1/2 F = 2-1	87.316 925	0.152757	5	4.19	Tracer of early stages of star formation
HNCO	$4_{0,4}$-$3_{0,3}$	87.925 238	0.878011	9	10.55	Indicate the presence of denser gas, than other high density tracers
HCN	1_1-0_1	88.630 4157				Tracer of dense gas,
	1_2-0_1	88.631 8473	2.4	9	4.25	infall motions
	1_0-0_1	88.633 9360				
HCO^+	1-0	89.188 526	3.0	3	4.28	Tracer of dense gas, outflows
HNC	1_0-0_1	90.663 450				Tracer of dense gas
	1_2-0_1	90.663 574	2.7	3	4.35	
	1_1-0_1	90.663 656				
HC_3N	10-9	90.978 989	5.81300	21	24.02	Indicate the presence of denser gas, than other high density tracers
CH_3CN	5_4-4_4	91.959 206	2.27824	22	127.60	Tracer of warm and
	5_3-4_3	91.971 465	4.05228	44	77.58	dense regions
	5_2-4_2	91.980 089	5.31863	22	41.84	
	5_1-4_1	91.985 316	6.07995	22	20.39	
	5_0-4_0	91.987 089	6.33432	22	13.25	
^{13}CS	2-1	92.494 303	1.41254	10	6.66	Tracer of dense gas
N_2H^+	1_{11}-0_{01}	93.171 621				Tracer of quiescent gas,
	1_{11}-0_{22}	93.171 917				”late depleter”
	1_{11}-0_{10}	93.172 053				

Table 3.2 (cont'd)

Molecule	Transition	Rest frequency (GHz)	A (*10^{-5}s^{-1})	g_u	E_u (K)	Comments
	1_{21}-0_{21}	93.173 480				
	1_{21}-0_{32}	93.173 777	3.8534	27	4.47	
	1_{21}-0_{11}	93.173 967				
	1_{01}-0_{12}	93.176 265				

Note. — Columns are species, transition, rest frequency, Einstein A coefficients, degeneracy, energy of the upper lewel, comments.

3.3 Results

3.3.1 Qualitative assessment

Figure 3.1 presents the average spectrum of an infrared dark cloud. To produce it we shifted the spectra of all our IRDCs to the same reference velocity and averaged spectra for each species with equal weight. The "average spectra" technique enables us to reduce the noise level and recognize weak lines, which are not detectable in the single spectra. Spectra for every single point are available in the on-line material (see Fig. C.1-C.19). For all IRDCs we have quite strong and clear detections of the HNC, HCO^+ and HCN molecules. In all cases we see a non-gaussian shape of HCO^+ with "shoulders" or double-peaked profiles. We will discuss the asymmetries of HCO^+ in comparison with the optically thin $H^{13}CO^+$ line in Sect. 3.3.3 in more detail.

N_2H^+ is detected everywhere, except for IRDC309.37-2. As it was expected, we cannot distinguish all 7 hyperfine components because of the large line width. While one hyperfine component (1_{01}-0_{12}) constitutes a distinct line peak, the other six transitions merge into two satellites.

HC_3N, HNCO and C_2H show rather weak emission and were detected in 18, 13 and 24 positions, respectively.

We detected very weak ^{13}CS(2-1) emission in three clouds. However, according to Ragan et al. (2006) and Jackson et al. (2008), CS is a common molecule in IRDCs. In some of our sources Jackson et al. (2008) detected only rather weak CS(2-1) emission

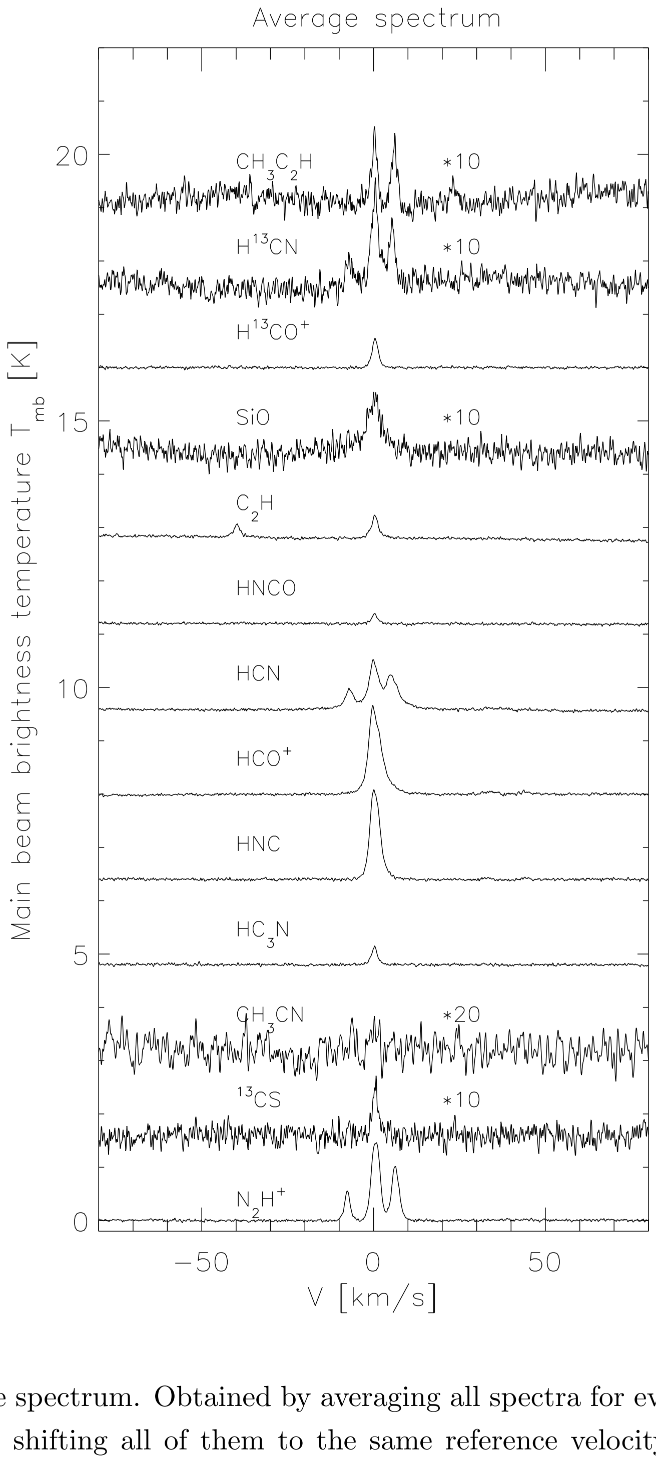

Figure 3.1 Average spectrum. Obtained by averaging all spectra for every species with equal weight after shifting all of them to the same reference velocity. Several weak detections are amplified by a factor of 10, and CH_3CN is amplified by a factor of 20 for plotting.

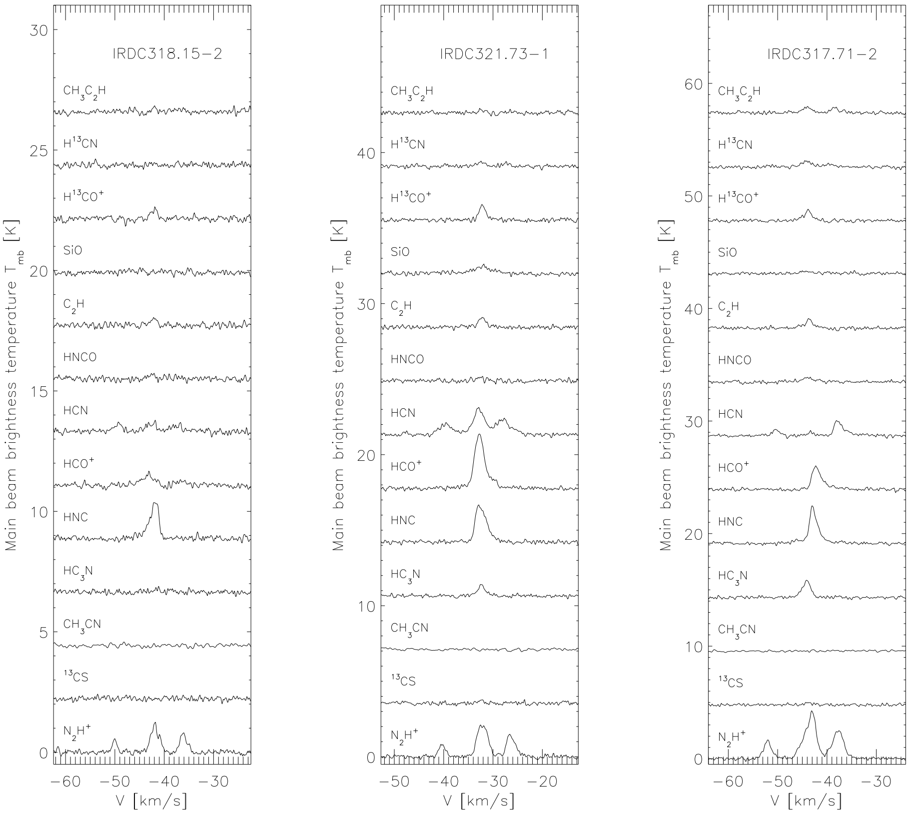

Figure 3.2 Line spectra for different mid-IR categories of IRDCs. (left) "Quiescent" cloud, (middle) "Middle" cloud, (right) "Active" cloud.

(0.4 - 1.02 K). Therefore, if we assume that ^{13}CS is 50 times less abundant than CS, the low ^{13}CS detection rate and weak emission can be understood. Depletion of CS can also play a significant role here (Beuther & Henning, 2009).

Even in the most evolved regions IRDC316.76-1 and IRDC316.76-2, where strong mid-IR and millimeter emission are present, we did not detect CH_3CN as a typical hot core tracer. Since CH_3CN emission arises from a warm and compact region, one explanation of this non-detection can be the low spatial resolution of the telescope and relatively low signal to noise ratio in our spectra. Using the "average spectra" technique we were able to reduce the noise level and to find very weak CH_3CN emission (see Fig. 3.1). This detection indicates that CH_3CN is present at least in some parts of our clouds, but there is an abundance deficit for this molecule in IRDCs. This result is in agreement with the previous work by Beuther & Sridharan (2007).

Another complex molecule CH_3C_2H was detected only in IRDC316.76-1 and 2 and shows very weak emission in IRDC316.72-1, IRDC316.72-2 and IRDC316.76-2. According to Cyganowski et al. (2008) and Chambers et al. (2009) it is more likely to see SiO, as an outflow tracer, in the clouds, where there is emission both at 4.5 and 24 μm. However, we detected SiO lines with extended line wings only in three regions with mid-IR emission: IRDC313.72-1, IRDC313.72-2 and IRDC316.76-1. Other potentially interesting regions with emission in mid-IR either show very weak SiO emission (IRDC317.71-2, IRDC309.94-1), or no SiO emission at all (IRDC309.37-1, IRDC310.39-2). The strongest SiO line was detected in the IRDC321.73-1. Within the Mopra beam this region contains a very weak source at 24 μm and so weak emission at GLIMPSE 4.5 μm that it was not identified as extended green objects (EGOs) in Cyganowski et al. (2008). We classify this object as "middle" (see below). Detection of SiO emission in such source indicates that absence or extreme weakness of mid-IR emission does not mean that star formation processes are not taking place in a cloud (cf. Lo et al., 2007) and shows the necessity of spectral line observations to identify outflows and star formation activity in molecular clouds.

Based on mid-infrared SPITZER data, Chambers et al. (2009) subdivided infrared dark clouds cores in to "active" and "quiescent". Cores were classified as "active", if they showed emission both at 8 and 24 μm, and as "quiescent" if they contained neither IR emission signatures. We added a "middle" stage to this classification whenever detect emission at 24 micron only and not at the shorter wavelength (see Table 3.1). In

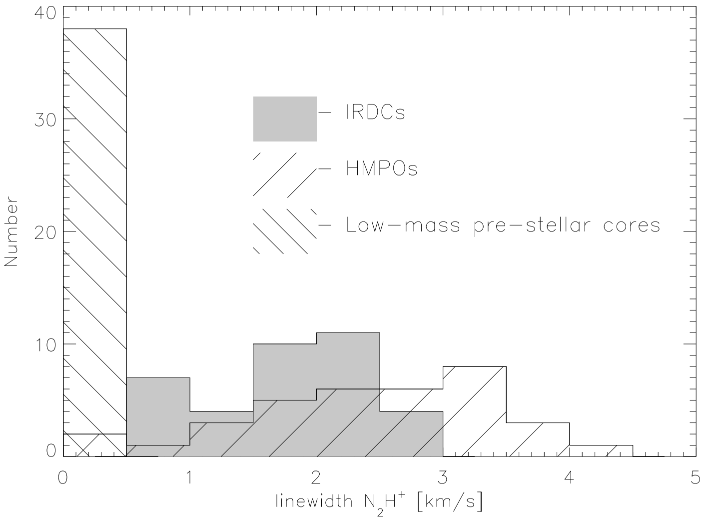

Figure 3.3 Distribution of N_2H^+ line width for our IRDCs sample, more evolved regions from Pirogov et al. (2003) and low-mass starless cores from Lee et al. (2001).

the Fig. 3.2 we presented the spectra for typical clouds from every category. Chambers et al. (2009) have shown that "active" cores have smaller sizes, higher densities and more pronounced water and methanol maser activity than the "quiescent" cores. However, from the qualitative analysis of the Mopra spectra, we do not see clear molecular signatures of any of these three categories of sources.

3.3.2 Line parameters

For the lines, where there is no hyperfine splitting (^{13}CS, HC_3N, HCO^+, HNCO, SiO, $H^{13}CO^+$), where the ratio of the hyperfine components is well known (N_2H^+), or for which we cannot resolve it (HNC), we estimate integrated and peak line intensities, LSR velocities and full linewidths at half maximum (Tables D-D). For other lines we estimated only integrated areas, measured by summing the channels between suitable velocity limits under the line (Table D). To make use of the derived parameters of detected lines we chose N_2H^+. This line is optically thin, the optical depth, which we derive fitting its hyperfine structure, does not exceed 0.5 for the most of the clouds. Therefore, N_2H^+ is less affected by optical depth effects and has a relatively simple line shape. In addition, 97% of the clouds show N_2H^+ emission. We find that line widths vary in range from 0.6 to 2.8 km/s and are in agreement with the results obtained by Ragan et al. (2006), where the line width was 0.5-4.0 km/s with the mean value 2.2 km/s, integrated intensities from 0.5 to 7 K km/s with the mean value 2.2 K km/s.

Comparing line parameters for "quiescent", "middle" and "active" regions, we can see that there is a trend to have larger line widths and higher integrated intensities in more evolved objects. The mean line widths are 1.4, 1.7 and 2.2 km/s and the integrated intensities are 4.7, 7.1 and 20.6 K km/s for "quiescent", "middle" and "active" sources respectively. These results are in good agreement with Chambers et al. (2009) who concluded that "active" sources are more evolved and present further evolutionary stages in comparison with "quiescent" sources.

Since N_2H^+ is widely detected in low- and high-mass starless and protostellar cores we used this line to compare line parameters for different types of objects (see Fig. 3.3). In low-mass starless cores (Lee et al., 2001) strong N_2H^+ emission was detected in 75% of the objects. Lines in low-mass regions are narrow with line width in the range of 0.2-0.4 km/s, and a mean value of 0.3 km/s, which allowed to distinguish all 7 hyperfine components. Integrated intensities in the case of low-mass objects are 0.4-6 K km/s (Crapsi et al., 2005). In comparison with IRDCs, low-mass pre-stellar cores show narrower lines. This behavior indicates that more turbulent processes take place in IRDCs. Clumping, which can easily be hidden within a $36''$ beam, can only partly explain such high values (Pillai et al., 2006a). The linewidth - size relationship also cannot explain high line width values in IRDCs. Heyer et al. (2001) report that a clear line width - size relation is just observed in larger clouds complexes of $>$ 10 pc in size. The IRDC clumps targetted by us are much smaller with typical sizes of around 1 pc. Furthermore, previous studies have already indicated that the line widths in high-mass star-forming clumps are much higher than would be predicted by the usual relations between line width and size determined from regions of lower mass (e.g. Shirley et al., 2003).

High-mass protostellar objects show N_2H^+ emission in all selected targets (Fuller et al., 2005; Pirogov et al., 2003). In comparison to low-mass cores, these targets have broader lines 0.5-3.5 km/s and very high integrated intensities 5-100 K km/s.

We also utilized N_2H^+ to estimate kinematic distances to our objects (see Table 3.1). In case of IRDC309.37-2 the N_2H^+ line was not detected and we used HCO^+ to estimate the distance. Since we observed several points within one cloud, distance determination helps us to confirm that clumps with associated mid-IR emission in

IRDC309.37, IRDC310.39 and IRDC371.71 are connected with the other "dark" parts of the respective clouds and are not just a projection effect.

In contrast to N_2H^+, the HCN hyperfine component intensity ratio is not a constant value. Afonso et al. (1998) show for low-mass dark clouds, that HCN hyperfine components can have different intensity ratios in different sources. In IRDCs, for most of the clouds we detected that the ratios F=2-1 to F=0-1 and F=2-1 to F=1-1 components are larger than 1. There are only two cases (IRDC317.71-1 and IRDC317.71-2), where the F=0-1 and F=1-1 components are stronger than the central F=2-1 component. Such hyperfine anomalies can be caused by foreground absorption in low-excitation molecular gas in the cloud.

3.3.3 HCO^+ and $H^{13}CO^+$ line profiles

As was already mentioned, the HCO^+ lines show a non-gaussian profile in almost all clouds. In some cases even its isotopoloque $H^{13}CO^+$ has a complicated line shape. Moreover, we see a significant shift, up to 2 km/s, between the peak positions of the optically thick HCO^+ line and optically thin $H^{13}CO^+$. A quantitative estimate of this asymmetry could provide us with information about dynamical processes in the clouds.

The most common way to extract line asymmetries is based on the comparison of optically thin and optically thick line positions: $\delta V = (V_{thick} - V_{thin})/\Delta V_{thin}$ (Mardones et al., 1997). This estimate was widely used both for low- and high mass star formation regions. (Fuller et al., 2005; Lee et al., 2001; Pirogov et al., 2003; Purcell et al., 2006). Using this criterion, we can subdivide our IRDCs in to "blue shifted" clouds with $\delta V < 0$ and "red shifted" clouds with $\delta V > 0$. The blue excess could be due to infall motions and red excess expanding motions or outflow. Among the sources, where both HCO^+ and $H^{13}CO^+$ were detected, we identified 19 "blue shifted" and 13 "red shifted" clouds. However, in the case of massive star formation, large line widths lead to quite small δV values in comparison with measurements errors. Therefore, we cannot rely on this criterion for the characterization of the dynamical state of IRDCs.

Another method to estimate line asymmetries quantitatively was described in Myers et al. (1996). They used an analytic two layer radiative transfer model to obtain theoretical spectra, compare them with the wide range of observed double-peak profiles and extract a formula for infall speed (see Eq. 9 from Myers et al. (1996)). This method allows us to estimate the infall velocity in a cloud by measuring blue and red peak

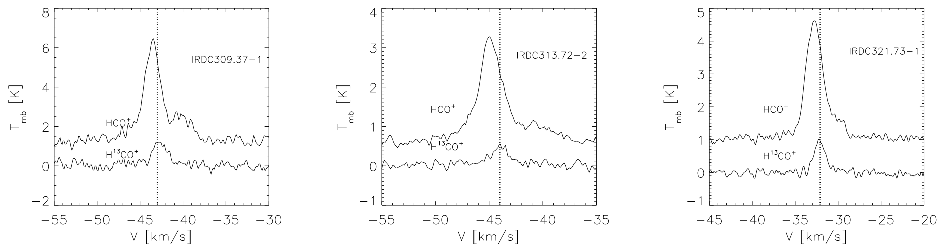

Figure 3.4 Samples of the HCO$^+$ and H^{13}CO$^+$ line profiles.

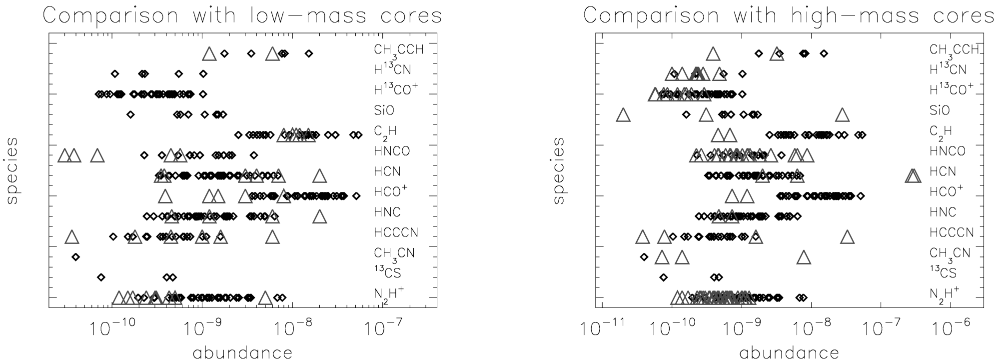

Figure 3.5 (left) Comparison of the molecular abundances of the IRDCs with low-mass pre-stellar cores. Diamonds indicate our IRDC abundances, triangles indicate low-mass pre-stellar cores. (right) Comparison of the molecular abundances of the IRDCs with HMPOs. Diamonds indicate our IRDC abundances, triangles indicate HMPOs. On the both panels the upper limit abundance value for CH$_3$CN was estimated from the average spectrum.

parameters of the optically thick line. Among all our targets we selected 3 clouds with clear red shoulders in HCO$^+$ and non-complicated shape of H^{13}CO$^+$ (see Fig. 3.4). The estimated infall velocities are around 2 km/s. This value is much higher than the sound speed in such an environment - 0.3 km/s, or a typical infall speed for low-mass starless cores 0.05-0.09 km/s (Lee et al., 2001).

3.3.4 Derived quantities: column densities and abundances

To estimate column densities we assume LTE conditions and optically thin emission and use the following equation:

$$\begin{aligned} N_{\rm tot} &= \tfrac{8\pi}{\lambda^3 A}\tfrac{g_l}{g_u}\tfrac{1}{J_\nu(T_{ex})-J_\nu(T_{bg})}\tfrac{1}{1-exp(-h\nu/kT_{ex})}\times \\ &\times \tfrac{Q_{rot}}{g_l exp(-E_l/kT_{ex})}\int T_{\rm mb}dv, \end{aligned} \quad (3.1)$$

where λ is the rest wavelength of the transition, A is the Einstein coefficient, g_u is the upper state degeneracy, $J_\nu(T_{ex})$ and $J_\nu(T_{bg})$ are the equivalent Rayleigh-Jeans excitation and background temperatures, Q_{rot} is the partition function, and E_l is the energy of the lower level (Lee et al., 2009). In our calculations for g_u, A and E_l we used values from The Cologne Database for Molecular Spectroscopy (CDMS) (Müller et al., 2005, 2001) (Table 3.2). For the excitation temperatures T_{ex} in all cases, except HCO^+ and $H^{13}CO^+$ (see below), we assume ammonia kinetic temperatures (Linz et al. in prep.) (Table 3.1). We calculate the partition function Q_{rot} for every source by interpolating data from the CDMS for the particular source temperature T_{ex}.

Integrated intensities $\int T_{\rm mb}dv$ for every species, were measured by summing the channels between suitable velocity limits under the corresponding molecular line (Table D).

The optically thin assumption is suitable for most of our lines: N_2H^+, ^{13}CS, HC_3N, HNCO, C_2H, SiO, $H^{13}CO^+$, $H^{13}CN$, CH_3C_2H. In case of optically thick emission (HCN, HCO^+, HNC) Eq. 4.4 gives only a lower limit. However, the presence of an optically thin isotopoloque let us estimate more realistic values for HCO^+. Using an algorithm described in Purcell et al. (2006) and assuming that HCO^+ is optically thick, $H^{13}CO^+$ is optically thin and their relative abundance ratio $X = [HCO^+]/[H^{13}CO^+]$ equals 50, we calculated HCO^+ column densities for the sources, where both HCO^+ and $H^{13}CO^+$ lines were detected. We do not apply the same algorithm for the pair HCN-$H^{13}CN$, since $H^{13}CN$ is detected only in four objects. In spite of non-detection of CH_3CN in any single spectra, the "average spectra" technique let us recognize the very weak CH_3CN (5_0-4_0) and CH_3CN (5_1-4_1) lines (see Fig 3.1). We use this average spectra to estimate the integrated intensity $\int T_{\rm mb}dv$ and derive the upper limit column density for this species.

To transfer column densities to abundances we use the N(species)/N(H_2) ratio, where N(H_2) values were estimated from the 1.2 mm SIMBA/SEST data (Vasyunina et al., 2009) adopting the Mopra telescope beam size (see Table 3.1). In the case of CH_3CN we use the average value for the molecular hydrogen column density of 1.2×10^{22} cm^{-2} and derived upper limit for CH_3CN abundances of $4.0.\times10^{-11}$. Abundances for other species are presented in Table 3.3.

For our column density and abundance estimates, systematic errors play the dominant role. One aspect is the assumption that all lines are optically thin. In case of moderately optically thick lines, the true column densities might be higher by a factor of $2-3$ for our objects. We also utilize kinetic temperatures derived from ammonia observations as excitation temperatures. This can give another factor of 2-5 to the estimated values. Systematic errors are also present in the molecular hydrogen column densities, derived from the millimeter continuum measurements, where we made assumptions about the dust model and equal gas and dust temperatures. All these assumptions give rise to a systematic error of an order of magnitude in molecular abundances which we obtained.

3.3.5 Are the objects really cold?

To estimate kinetic temperatures in our clouds we observed the ammonia (1,1) and (2,2) inversion transitions with the Parkes radio telescope. These transitions are known as a good thermometer for cold, dense gas. We derived kinetic temperatures for most IRDCs between 10 and 30 K (Linz et al. in prep.). Ammonia observations show the presence of cold gas in IRDCs. However, the Parkes telescope beam is $72''$ or approximately 1 pc at the typical IRDCs distances. With the Mopra telescope (telescope beam $36''$) we can trace a smaller volume and use other molecular lines to identify warmer regions.

One way is to consider the HCN/HNC abundance ratio. This ratio strongly depends on the temperature and in the case of the Orion molecular cloud decreases from 80 near the warm core to 5 on the colder edges (Goldsmith et al., 1986; Sarrasin et al., 2010; Schilke et al., 1992). For our IRDC sample the estimated HCN/HNC abundance ratio values are not higher than 3. This confirms, that we deal with quite cold clouds.

Beside ammonia, symmetric top molecules like CH_3C_2H can be used as probes of kinetic temperature in molecular clouds (Bergin et al., 1994). We detect CH_3C_2H in 5 targets. In two objects the 5_2-4_2, 5_1-4_1 and 5_0-4_0 components are clearly seen. This allows us to estimate rotational temperatures in these regions, using the algorithm given in Bergin et al. (1994). Derived temperatures equal 17 K for IRDC317.71-2 and

38 K for IRDC316.76-1. The temperature for IRDC317.71-2 is similar to the value we have from ammonia observations, whereas the temperature for IRDC316.76-1 is 15 K higher. This indicates that in some clouds a warmer component can be present in addition to cold gas. In the case where there is also a warm gas component and the real gas temperature in some targets is higher, we underestimated molecular abundances. The abundances for IRDC316.76-1 with T=38 K become a factor of 1.2-1.7 higher. However, taking into account all our assumptions and the still large telescope beam, this difference is still within the error limit.

3.3.6 Special objects

In this subsection we present infrared dark clouds, where line spectra show some unique features.

IRDC317.71 In this cloud (Fig 3.2) at points 1 and 2 we detect a different ratio of HCN hyperfine components from other IRDCs: F=0-1 and F=1-1 components are stronger than the central F=2-1. $H^{13}CO^+$ emission peak is shifted to the blue side in comparison with HCO^+ and corresponds to the extinction in the optically thick component. The HCN/HNC abundance ratio is lower than 1. The point 2 is one of the five locations where CH_3C_2H was detected. As we can see from the previous section, the CH_3C_2H excitation analysis shows the presence of a warmer gas component thus indicating a more evolved star forming region.

Most probably the HCN spectrum can be explained by foreground absorption in low-excitation molecular gas. Similar hyperfine anomalies are frequently seen in cold dark clouds where they are explained in this way (absorption in the envelope). The same effect is probably seen in HCO^+. The HCO^+ line asymmetry apparently indicates the velocity shift of the foreground absorption. If attributed to the envelope, this shift indicates an expansion. In addition, HCO^+ perhaps traces a contribution from an outflow.

IRDC321.73 In IRDC321.73-1 (Fig 3.2), in spite of no emission in GLIMPSE bands and only a very weak source at 24 μm, we detected clear SiO emission. This indicates the presence of a shock and, probably, outflow activity in this region. The presence of the red HCO^+ shoulder may be an evidence of infall motion. The other two points in this cloud (IRDC321.73-2 and IRDC321.73-3) show a more complicated than average shape of HCO^+. The rest of the lines, even optically thin like N_2H^+, also have non-gaussian shapes. This can be explained by the presence of several kinematic components.

Table 3.3. Abundances of the IRDCs.

Name	N_2H^+	^{13}CS	HC_3N	HNC	HCO^+	HCN	HNCO	C_2H	SiO	$H^{13}CO^+$	$H^{13}CN$	CH_3C_2H	category[a]
IRDC308.13-1	5.5(-10)			8.6(-10)	6.3(-09)	1.0(-09)				1.2(-10)			Q
IRDC308.13-2	2.9(-10)			4.9(-10)		6.0(-10)		4.3(-09)					M
IRDC308.13-3	2.2(-10)			5.4(-10)		6.8(-10)							M
IRDC309.13-1	1.1(-09)			9.7(-10)	3.7(-08)	1.5(-09)		5.0(-09)		7.4(-10)			M
IRDC309.13-2	7.5(-10)			9.1(-10)		1.5(-09)							M
IRDC309.13-3	9.0(-10)			6.2(-10)	2.8(-08)	2.0(-09)				5.6(-10)			A
IRDC309.37-1	7.7(-09)		7.3(-10)	4.9(-09)	2.4(-08)	6.1(-09)	3.7(-09)	4.7(-08)		4.9(-10)			A
IRDC309.37-2				2.8(-10)		6.3(-10)							A
IRDC309.37-3	1.0(-09)			1.4(-09)	1.7(-08)	1.9(-09)				3.4(-10)			Q
IRDC310.39-1	2.3(-09)		6.2(-10)	2.0(-09)	1.3(-08)	3.3(-09)	3.5(-10)	1.6(-08)	1.6(-10)	2.7(-10)			A
IRDC310.39-2	1.0(-09)		3.9(-10)	1.3(-09)	8.9(-09)	2.4(-09)		1.3(-08)		1.7(-10)			A
IRDC312.36-1	7.5(-10)		1.0(-10)	8.2(-10)	1.1(-08)	1.2(-09)	7.2(-10)	4.7(-09)		2.2(-10)			A
IRDC312.36-2	5.1(-10)			1.0(-09)	5.1(-08)	1.2(-09)				1.0(-09)			Q
IRDC313.72-1	3.1(-09)		1.5(-09)	3.7(-09)	2.4(-08)	4.6(-09)	2.1(-09)	2.4(-08)	1.5(-09)	4.8(-10)			A
IRDC313.72-2	3.2(-09)	4.7(-10)	1.1(-09)	3.5(-09)	2.3(-08)	4.6(-09)	1.7(-09)	1.8(-08)	1.6(-09)	4.6(-10)			A
IRDC313.72-3	3.4(-09)			4.8(-09)	2.1(-08)	5.3(-09)	1.9(-09)	1.5(-08)	1.4(-09)	4.3(-10)			Q
IRDC313.72-4	2.5(-09)			3.3(-09)	1.8(-08)	3.8(-09)			5.7(-10)	3.7(-10)			Q
IRDC316.72-1	3.4(-09)		3.9(-10)	4.4(-09)	3.0(-08)	5.2(-09)	1.4(-09)	2.9(-08)		6.1(-10)	5.4(-10)	8.1(-09)	M
IRDC316.76-1	6.8(-09)	4.0(-10)	1.0(-09)	6.3(-09)	1.1(-08)	6.8(-09)	1.5(-09)	5.3(-08)	7.0(-10)	2.2(-10)	1.0(-09)	1.5(-08)	A
IRDC316.72-2	1.8(-09)		2.3(-10)	2.2(-09)	2.2(-08)	2.5(-09)		1.6(-08)		4.5(-10)		7.6(-09)	Q
IRDC316.76-2	1.1(-09)	7.5(-11)	2.4(-10)	1.2(-09)	5.7(-09)	1.7(-09)		1.6(-08)		1.1(-10)	2.1(-10)	1.7(-09)	A
IRDC317.71-1	1.2(-09)		1.7(-10)	8.4(-10)	1.0(-08)	5.0(-10)	8.1(-10)	5.6(-09)		2.1(-10)			Q
IRDC317.71-2	9.7(-10)		3.6(-10)	5.0(-10)	4.7(-09)	3.3(-10)	5.3(-10)	3.6(-09)		9.5(-11)	1.0(-10)	3.4(-09)	A
IRDC317.71-3	7.9(-10)			7.2(-10)	8.6(-09)	6.2(-10)			5.2(-10)	1.7(-10)			Q
IRDC320.27-1	4.8(-10)			6.9(-10)	1.5(-08)	1.0(-09)				3.0(-10)			Q
IRDC320.27-2	4.6(-10)			4.1(-10)		6.7(-10)							Q
IRDC320.27-3	1.9(-10)			3.6(-10)		4.3(-10)							Q
IRDC321.73-1	2.0(-09)		5.1(-10)	1.8(-09)	1.3(-08)	3.1(-09)		1.4(-08)	1.0(-09)	2.7(-10)			M
IRDC321.73-2	4.2(-10)		6.1(-10)	7.2(-10)	4.3(-09)	9.1(-10)		4.0(-09)		8.7(-11)			M
IRDC321.73-3	5.8(-10)		4.6(-10)	8.9(-10)	5.9(-09)	1.0(-09)		3.3(-09)		1.1(-10)			A
IRDC013.90-1	2.9(-10)		1.5(-10)	4.0(-10)	3.8(-09)	4.2(-10)		2.5(-09)		7.6(-11)			M
IRDC013.90-2	2.9(-10)			2.4(-10)	6.1(-09)	3.4(-10)				1.2(-10)			Q
IRDC316.45-1	1.4(-09)		6.8(-10)	1.3(-09)	1.6(-08)	1.2(-09)	2.2(-10)	8.1(-09)		3.2(-10)			M
IRDC316.45-2	1.7(-09)			1.9(-09)	3.5(-08)	1.7(-09)	9.4(-10)	1.1(-08)		7.0(-10)			M
IRDC318.15-1	1.2(-09)			1.7(-09)	2.0(-08)	1.6(-09)		1.2(-08)	-	4.1(-10)			M
IRDC318.15-2	1.5(-09)			1.8(-09)	3.4(-08)	1.4(-09)		9.3(-09)		6.9(-10)			Q
IRDC309.94-1	1.5(-09)		3.4(-10)	8.9(-10)	3.5(-09)	1.2(-09)	7.3(-10)	9.1(-09)		7.1(-11)	2.3(-10)		A
Average abundances													
IRDCs	1.6(-09)	3.1(-10)	5.4(-10)	1.6(-09)	1.7(-08)	2.0(-09)	1.2(-09)	1.4(-08)	9.5(-10)	3.4(-10)	4.2(-10)	7.2(-09)	
low-mass	7.7(-10)		1.5(-09)	6.9(-09)	3.7(-09)	5.8(-09)	2.3(-10)	1.1(-08)				3.6(-09)	

3.4 Discussion

Carey et al. (1998) and Pillai et al. (2006a) mention a difference in the ammonia and formaldehyde abundances and hence a possible chemical difference between low-mass pre-stellar cores and IRDCs. To study the chemical conditions in IRDCs, Sakai et al. (2008) observed N_2H^+(1-0), HC_3N(5-4), CCS(4_3-3_2), NH_3(1,1), (2,2), (3,3) and CH_3OH(7-6) lines toward the massive clumps associated with IRDCs. They estimated the CCS and N_2H^+ abundance ratio and used low-mass prestellar core abundances from Benson et al. (1998) for the comparison. The result of this analysis showed that IRDCs have lower N(CCS)/N(N_2H^+) ratio values and hence, they can be chemically more evolved than low-mass starless cores. However, Sakai et al. (2008) used particular low-mass objects for the comparison and did not take into account the starless cores L1512 and L63, where N(CCS)/N(N_2H^+) ratio is low and is in agreement with values obtained for their IRDC sample.

We compare our IRDCs abundances with the data available in the literature for low-mass starless clouds and more evolved high-mass objects. We also analyse the dispersion of the particular abundance values. With such a comparison we want to determine if the molecular abuncances in IRDCs are similar to the low-mass starless cores, or whether they show signatures of more evolved evolutionary stages.

To make a comparison with low-mass cold clouds, we used molecular abundances from Padovani et al. (2009), Tafalla et al. (2006), Jørgensen et al. (2004) and Ohishi et al. (1992) (Fig. 3.5 left panel). Comparing the dispersion of the abundance values we find that for some species, like HC_3N, there is a large spread in abundance for the low-mass sample, but higher and lower values occur with regard to the IRDC values. For HNCO, new results by Marcelino et al. (2009) show that HNCO abundances for low-mass prestellar cores seem to be low (when computed adopting the H_2 column densities mentioned in Table 3 of Marcelino et al. (2010)), but cores like L183 and TMC-1 reach HNCO abundances just a factor of around 2 to 3 lower than the IRDC average value. The same situation, in principle, is found for HCO^+, where an overlap between the low-mass core and IRDC HCO^+ abundances exist for the objects L183 and TMC-1 (both attaining 8.0×10^{-9} according to Ohishi et al. (1992)). There is a tendency for higher abundances in IRDCs compared to low- mass cores for N_2H^+.

Table 3.3 (cont'd)

Name	N_2H^+	^{13}CS	HC_3N	HNC	HCO^+	HCN	HNCO	C_2H	SiO	$H^{13}CO^+$	$H^{13}CN$	CH_3C_2H	category[a]
high-mass	5.2(-10)		8.7(-09)	6.0(-10)	9.6(-10)	1.5(-07)	1.8(-09)	5.7(-10)	9.4(-09)	1.4(-10)	2.2(-10)	1.8(-09)	

[a] "A" indicates "active" cores, "M" - "middle", "Q" - "quiescent".

However, also here we found with L1544 a prominent example of a low-mass prestellar core with a rather high N_2H^+ abundance of 5.0×10^{-9} (Jørgensen et al., 2004).

The difference between mean abundances of IRDCs and low-mass objects is a factor of 2-3 for all species and around 5 in the extreme case of HNCO (see Table 3.3). Taking into account a large spread in abundances for every molecule within our IRDCs sample and systematic errors (see Sect. 3.3.4), such differences in average abundances between the low-mass starless cores and IRDCs cannot be used to claim a clear and unequivocal chemical distinction between the two groups of objects.

The next class of objects, which is interesting for the comparison with our results, is the class of more evolved high-mass protostellar objects (HMPOs). HMPOs are bright at mid- and far-IR wavelengths and characterized by higher gas temperatures, compared to IRDCs. It is assumed that these objects present one of the early stages of high-mass star formation, where the central protostar has a mass > 8 $M_\odot$ and is still accreting. (e.g. Beuther et al., 2007; Sridharan et al., 2002). For the comparison we use data from Blake et al. (1987), Helmich & van Dishoeck (1997), Pirogov et al. (2003) and Zinchenko et al. (2009, 2000). HMPOs and IRDCs have different physical conditions (e.g. temperatures) and, hence, are expected to show different chemistry.

From our comparison we can see, that high-mass protostellar objects show higher mean HC_3N and HCN abundances, since some HMPOs have extremely high abundances of these species. C_2H, on the contrary, has the mean abundance a factor of 20 lower in the case of HMPOs. We did not detect CH_3CN emission in any single IRDCs spectra. However, using the "average spectra" technique we reduce the noise level and find very weak CH_3CN emission and estimate its upper abundance limit. This upper limit is lower in comparison with the HMPOs abundances from single-dish studies by (Helmich & van Dishoeck, 1997) and (Blake et al., 1987) (see Fig. 3.5 right panel). Previous theoretical (Nomura & Millar, 2004) and observational (Beuther & Sridharan, 2007) studies of high-mass star forming regions showed that a low amount of CH_3CN is typical for the earliest evolutionary stages. The average abundances of HC_3N, HCO^+, HCN and C_2H for IRDCs and HMPOs differ by a factor of $16-75$. These differences are significant, even when considering all of the included assumptions and uncertainties.

Another criterion that we use to determine the chemical status of IRDCs is the HCN/HNC abundance ratio. For the low-mass prestellar cores from Tafalla et al. (2006), Jørgensen et al. (2004) and Ohishi et al. (1992) this ratio is ≤ 1. Values of the HCN/HNC abundance ratio for HMPOs are higher and reach values up to 13 (see Helmich & van Dishoeck (1997) and Blake et al. (1987)) and are around 80 in the extreme regions like Orion (Goldsmith et al., 1986; Schilke et al., 1992). We find the HCN/HNC abundance ratios for our IRDCs ~ 1. This value is in agreement with the theoretical predictions for the cold clouds (Sarrasin et al., 2010) and values for the low-mass starless cores.

Considering that complex organic molecules are typical for more evolved and warmer objects (Helmich & van Dishoeck, 1997), and assuming that the HCN/HNC abundance ratio strongly depends on temperature and is enhanced in active star-forming cores (Goldsmith et al., 1986; Schilke et al., 1992), our results support the idea that IRDCs present rather low mass star-less core chemistry than HMPOs chemistry. However, the number of low-mass starless cores and HMPOs, which we used for the analysis, may be not sufficient in a strict statistical sense. Therefore, to make more solid statement about the evolutionary status of IRDCs and be more confident, we need to extend the line samples, add sulfur bearing species, and perform further studies, including chemical modeling.

Beside the comparison with low- and high-mass cloud abundances, we also compare molecular abundances of "quiescent", "middle" and "active" regions within our IRDC sample. In accordance with recent results by Battersby et al. (2010), we do not detect any significant difference among these three categories.

3.5 Conclusions

In this paper, we present 3 mm molecular line observations with the 22-m Mopra radio telescope. In total 13 molecular lines were observed for all IRDCs. The results of our study can be summarized as follows:

1. Using H_2 column densities from the previous investigation, we estimate molecular abundances of all species. We show that there is a tendency for the IRDCs to have molecular abundances similar to the low-mass starless core rather than to the HMPOs abundances. However, the derived abundances come with uncertainties of around one order of magnitude. Furthermore, also the comparison abundances for low–mass cores and HMPOs can be affected by considerable uncertainties,

especially, when abundances have been computed in the literature by combining heterogeneous data sets (regarding beam sizes etc.). To make more solid statements about the evolutionary status of IRDCs therefore calls for subsequent systematical studies.

2. According to the classification of Chambers et al. (2009), we subdivided our clouds to "quiescent" and "active" and added "middle" class to them. We have found a trend for more evolved regions to have higher line widths and integrated intensities. However, we do not detect clear evidence of different chemistry in these three groups.

3. Comparison of the line width and integrated intensities of the IRDCs and low-mass dark clouds show several times higher values for IRDCs. Broader and more intense lines mean that in IRDCs we have more turbulent conditions in comparison with low-mass clouds.

4. We detect the SiO emission in some clouds and complicated shapes of the HCO^+ emission line profile in all IRDCs, which indicates the presence of infall and outflow motions and the beginning of star formation activity, at least in some parts of the IRDCs.

5. The analysis of the two available CH_3C_2H excitation diagrams and detection of the very weak CH_3CN (5_0-4_0) and CH_3CN (5_1-4_1) lines on the "average spectra" indicate the presence of a warm gas component in some IRDCs. However, these warm regions are compact and cannot be resolved with single-dish observations.

4

Near-infrared spectroscopy of the IRAS 06058+2138 cluster

4.1 Introduction

The previous two chapters of this thesis are devoted to investigations of the physical and chemical properties in the earliest stages of massive stars. In this chapter, I consider a later stage related to the embedded, newly formed massive stars in typical cluster environments.

In particular we focus on the young embedded cluster - IRAS 06058+2138 (AFGL 5180, G188.95+0.89). It is located in the outer Galaxy - in the Gemini OB1 molecular cloud complex and associated with the H II region Sh 247 (Carpenter et al., 1995a,b). IRAS 06058+2138 shows evidence of OH, H_2O and methanol maser emission (Caswell et al., 1995; Henning et al., 1992; Szymczak et al., 2000). CO observations by Snell et al. (1988) showed the presence of an outflow in this region. The spatial resolution of both masers and the CO data do not let us associate them with the particular IR source. However, VLBI observations (Minier et al., 2001) indicate that the 6.7 and 12.2 GHz methanol masers are located at the neck of the infrared nebula, at the position of the near infrared source NIRS 1, which is believed to power an outflow (Tamura et al., 1991). Klein et al. (2005) mapped regions around bright far-IR sources in the millimeter continuum in order to identify massive cold cloud cores. They found that the (sub)mm core of IRAS 06058+2138 is located $20''$ away from the near- and mid-IR sources. Hence Klein et al. (2005) identify this region as a "pre-protostellar candidate". High-resolution mid-IR images by Longmore et al. (2006) showed that the central source AFGL 5180 has a multiple nature and hides four young embedded objects. As a by-product of the near-IR speckle imaging of the AFGL 5180, Alvarez et al. (2004) find another binary at a distance of $12.''8 \pm 0.''1$ from their target. Leistra et al. (2006) and Devine et al. (2008) used near-IR JHK photometry to probe the stellar population, extinctions and ages of several clusters including IRAS 06058+2138. Based on the slope of the K-band luminosity function, and the disk fraction of YSOs, they determined the age of the cluster to be $\sim 2.5 \pm 3$ Myr. From the CO molecular line observations, the distance of 1.5 kpc to this cluster was determined by Snell et al. (1988). For our study we use the results of the recent H_2O maser parallax observations by Oh et al. (2010), who determined a more precise distance of 1.76 ± 0.11 kpc.

The previous studies already showed the presence of outflows, maser emission and young stellar objects in IRAS 06058+2138, indicating active star formation in the cluster. The aim of this study is to investigate star-formation mechanism, using information at different wavelengths. To have a more clear picture of the physical processes which take place here, we combined near-IR SINFONI data with mid-IR Spitzer/IRAC data from the archive and 1.37 mm continuum SMA maps (Javier Rodon, PhD thesis). The near-IR data provide us with a spectroscopic classification of the stellar content of IRAS 06058+2138. The millimeter and mid-IR data give us additional information about more embedded and, hence younger objects.

This chapter is organized as follows: in Sect. 4.2 we discuss the SINFONI and IRAC observations along with respective data reduction. The large scale structure of the region and its morphology at different wavelengths is describe in Sect. 4.3. Sect. 4.4 is devoted to the investigation of the excitation mechanisms in the molecular hydrogen emission regions. Based on the obtained stellar spectra, we study the stellar content of the cluster in Sect. 4.5. In Sect. 4.6 we discuss possible star-formation scenarios for the region and make an investigation about the outflow activities. Sect. 4.7 summarizes the main conclusions of this chapter.

4.2 Observations and data reduction

4.2.1 SINFONI observations and data reduction

Observations of IRAS 06058+2138 were performed in the near-infrared H- and K-bands using the Integral Field spectrograph SINFONI (Bonnet et al., 2004; Eisenhauer et al., 2003) on UT4 (Yepun) of the VLT at Paranal, Chile. We used the non-AO mode of SINFONI together with the widest field of view ($8'' \times 8''$). These settings provide us with a spatial resolution of $0.25''$ per slitlet. The typical seeing during the observations was $0.7''$ in K. The H+K grating let us cover both H and K bands simultaneously with spectral resolution of R=1500 in a single exposure.

IRAS 06058+2138 was observed with a detector integration time (DIT) of 30 s per pointing to guarantee a good signal-to-noise ratio (S/N $\sim$ 70) for the early B-type stars within this cluster. The observations were centered on the central star AFGL 5180 at coordinates: α (2000) = $06^h\ 58^m\ 53.4^s$, δ (2000) $=+21^\circ\ 38'\ 28.3''$. Since the region is much larger than the field of view of SINFONI, we observed this area using a raster pattern, covering every location in the cluster at least twice. The offset in the east-west direction was $4''$ and the offset in the north-south direction was $6.75''$. A sky frame was taken every 3 minutes using the same DIT as the science observations. The sky positions were chosen manually, based on existing NIR imaging in order to avoid contamination. Immediately after every science observation, a telluric standard of B spectral type was observed, matching as close as possible the airmass of the object. This star is used for the removal of the telluric absorption lines as well as for flux calibration. For each observing block we chose one star as telluric standard. These were Hip050780, Hip026132, Hip032108, Hip040105 and Hip043964.

Data reduction was performed by Arjan Bik (see Bik et al. (2010) for a detailed description), using the SPRED software developed by the MPE SINFONI consortium (Abuter et al., 2006; Schreiber et al., 2004). As a result a 3D cube was produced with spatial information along the x and y axes and spectral information along the z axis.

4.2.2 IRAC data reduction

We include archival data, originally obtained with the *Spitzer* satellite (Werner et al., 2004) on March 26, 2005 (Program P03603, AOR key 11268096). These observations were conducted with the IRAC instrument (Fazio et al., 2004) in the 3.6, 4.5, 5.8, and

8.0 μm filters towards the massive YSO AFGL 5180 in the center of the IRAS region. In order to prevent saturation of the central bright emission region, these observations have been performed in SUBARRAY mode, where only parts of the IRAC detectors are being read out repeatedly, but with a very short elementary frame time of 0.1 s. The usable field of view is then around 48 arcsec in size for the used dither pattern. The total duration time for the observations were 742 s. We started from the bcd files and used the EASYMOSAIC script within the MOPEX data reduction environment to produce final mosaics in the four filters with the standard $1.''2$ pixel size.
Simple aperture photometry has been performed on these mosaics by using the ATV tool within IDL. The results have been converted to Jy and aperture corrections according to the IRAC Instrument Handbook[1] have finally been applied.

4.3 Morphology of the region

IRAS 06058+2138 is part of the GEM OB1 molecular cloud complex, which consists of several massive star-forming regions, supernova remnants, a bipolar reflection nebula and HII regions. Fig. 4.1 presents the large-scale structure of the ^{12}CO emission in the molecular complex. The brightest molecular emission was found near the optical HII region Sh 247. Based on the ^{12}CO(1-0) and ^{13}CO(1-0) observations, Carpenter et al. (1995a) claimed that the filament to the east from the HII region is associated with it and suggested a triggered star-formation scenario. The CS(2-1) observations (Carpenter et al., 1995b) allowed to identify denser cores within this filament. These denser cores are also well seen in the submillimeter SCUBA map (Fig 4.1; Right panel). On this figure, the background is the SCUBA 850 μm map (Di Francesco et al., 2008), contours are NRAO VLA Sky Survey (NVSS) continuum data at 1.4 GHz (Condon et al., 1998). The upper core corresponds to IRAS 06061+2151, the filament on the south to IRAS 06056+2131 and the central compact core to our cluster IRAS 06058+2138.

Near-IR observations allow us to investigate not only the stellar content of the region, but also thermal emission from the molecular cloud dust. In the Fig. 4.2 (upper panel) we present a 3-color composite SINFONI image, where blue is FeII (1.64 μm, line+continuum), green is H_2 (2.12 μm, line+continuum) and red is Brγ (2.16 μm, line+continuum). In the center of the region there is a a very bright NIR point source

---

[1] http://ssc.spitzer.caltech.edu/irac/iracinstrumenthandbook/

- AFGL 5180 (NIRS 1 from Tamura et al., 1991). To the east of this source, lies the already formed cluster, which is surrounded by a molecular hydrogen bubble. Within the bubble there is also a region with strong FeII and H_2 emissions. Further, we designate it the "hour-glass" region. Two very red sources are located in the northern and in the southern parts of this region. These objects were observed by Bik et al. (2006) and classified as young stellar objects. At the right side (west) from the AFGL 5180 there is Brγ emission and two H_2 features, which look like bowshocks.

The contour lines on the Fig. 4.2 (upper panel) correspond to the 1.37 mm SMA continuum data. At the millimeter wavelength we can identify a large embedded cluster in the southern part of the region. There are no NIR continuum sources associated with it, however we can see faint molecular hydrogen emission there. Next to the millimeter cluster there is a chain of separate millimeter point sources, which is not covered by NIR SINFONI maps. Further to the north there are two other millimeter sources very close to each other. The brightest of them coincides with AFGL 5180.

The high-resolution imaging by Alvarez et al. (2004) and Longmore et al. (2006) in the near- and mid-IR wavelength respectively, showed that at least two of our sources have a multiple nature. Near-IR speckle imaging showed that the brightest star (marked by star-sign in the Fig. 4.2, lower panel) inside the molecular hydrogen bubble has two binary components, separated by $0.''3 \pm 0.''1$. Then, mid-IR data allows us to identify four objects within the AFGL 5180. The positions of these sources are marked with crosses on the Fig. 4.2 (lower panel).

In addition to the near-IR and millimeter data, we use also mid-IR Spitzer/IRAC maps from the archive. The IRAC maps centered on AFGL 5180 and cover most of the near-IR cluster. They give us information about the sircumstellar matter of the YSOs and possible presence of deeply embedded sources. In the Fig. 4.3 (top panel) 3-color Spitzer/IRAC composite image (blue is 3.6 μm, green is 4.5 μm and red is 8.0 μm) is presented. The region to the left of AFGL 5180 is predominated by 8 μm emission. The region to the right, on the contrary, is bright only at 3.6 and 4.5 μm. As it was shown by Cyganowski et al. (2008) and Chambers et al. (2009), 4.5 μm emission indicates the presence of outflows and shocks related to the beginning of the star formation process. The 8.0 μm emission is most likely PAH emission excited by the UV radiation of the star inside the bubble. Except extended emission at mid-IR we can identify three point sources. Their position relative to the near-IR and millimeter clusters are presented

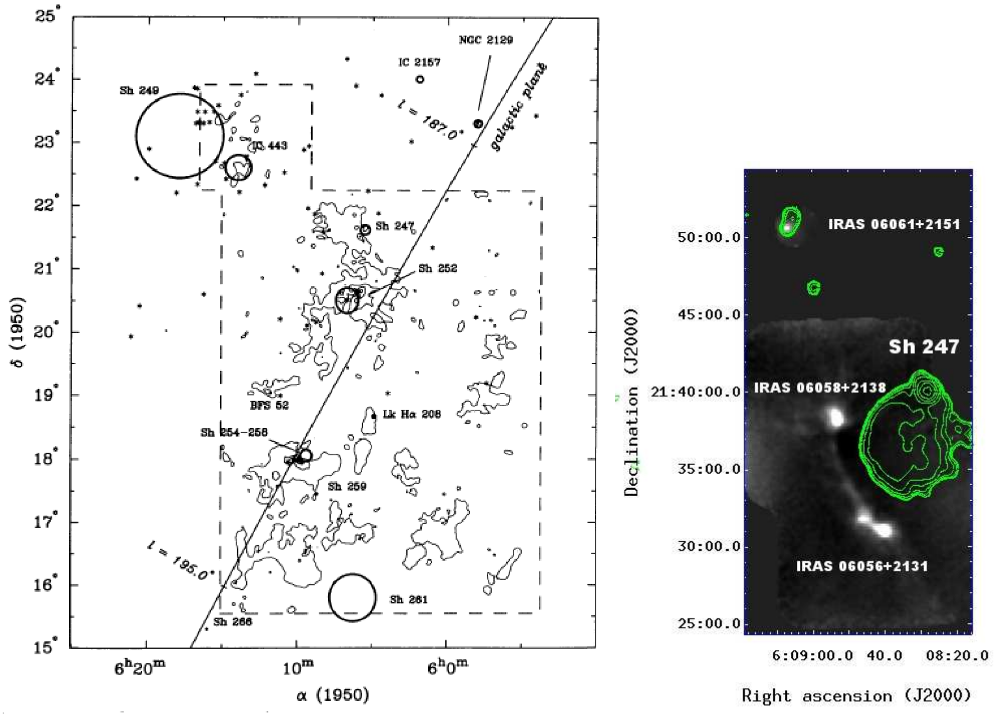

Figure 4.1 Left panel: ^{12}CO map of the Gemini OB1 molecular cloud from Carpenter et al. (1995a). Circles mark the positions and sizes of optical HII regions. The dashed line outline the mapped region. Right panel: SCUBA 850 μm map of the Sh 247 region and surroundings overlaid with NRAO VLA Sky Survey (NVSS) continuum data.

in Fig. 4.3 (bottom panel), where the background is the 3-color SINFONI composite image and contours are the 3.6 μm Spitzer/IRAC data. The brightest source in the center is AFGL 5180. On the east there is a faint source inside the molecular hydrogen bubble coinciding with the IRAS source position. The third source in the southern part corresponds to the position of the millimeter cluster. In these images we can also see that 3.6 μm emission corresponds to the Brγ emission on the west side of the region and forms an "outflow cone" with the H_2 bowshocks inside.

4.4 Molecular hydrogen regions

In IRAS 06058+2138 we identify several regions of the molecular hydrogen emission. There are two bowshocks on the right side (west), first detected by Davis et al. (1998),

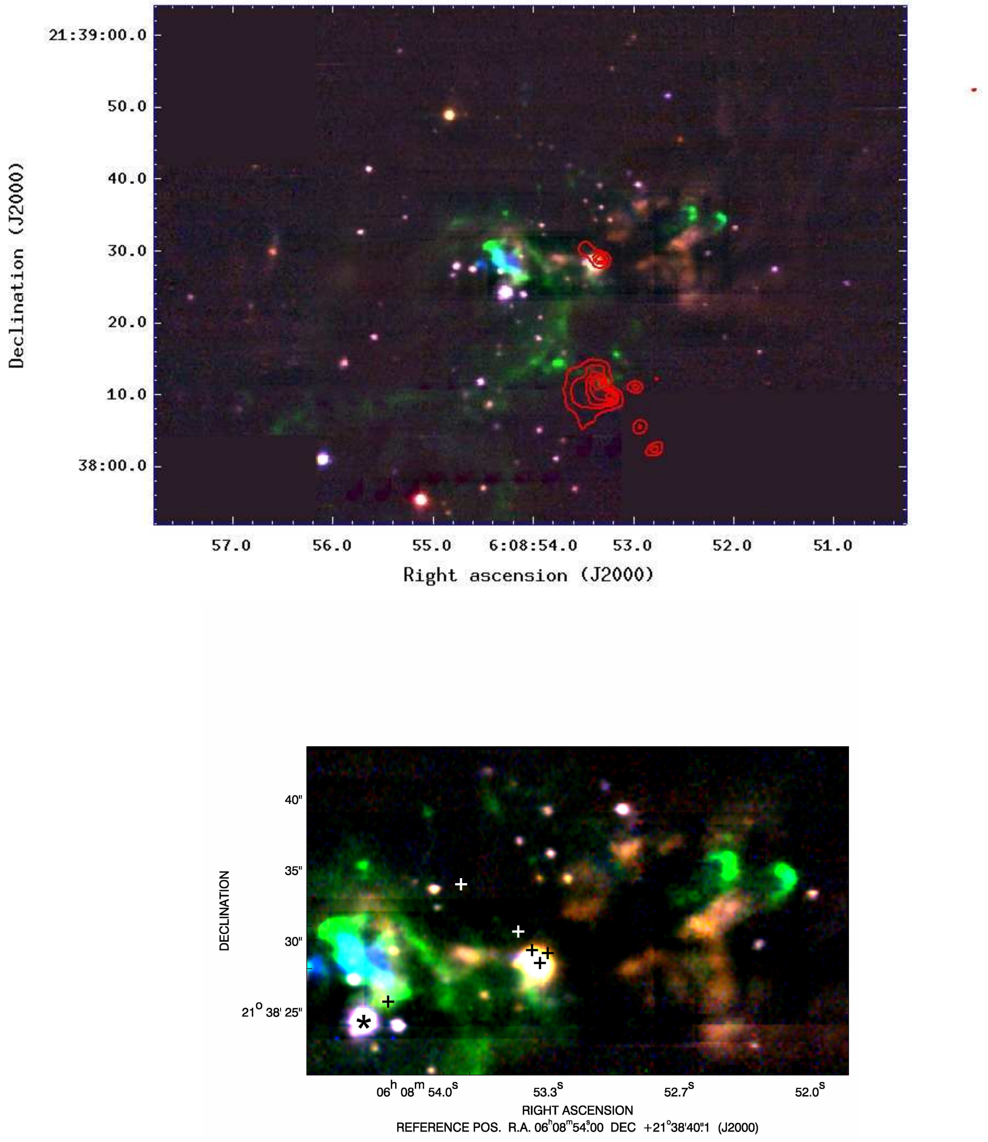

Figure 4.2 Upper panel: the 3-color composite SINFONI image. Blue is FeII (1.64 μm, line+continuum), green is H_2 (2.12 μm, line+continuum) and red is Brγ (2.16 μm, line+continuum). Contour lines are 1.37 mm SMA continuum data. Lower panel: zoomed in 3-color composite SINFONI image. Blue is FeII (1.64 μm, line+continuum), green is H_2 (2.12 μm, line+continuum) and red is Brγ (2.16 μm, line+continuum). Crosses denote position of the mid-IR sources from Longmore et al. (2006). Star marks the binary source from Alvarez et al. (2004).

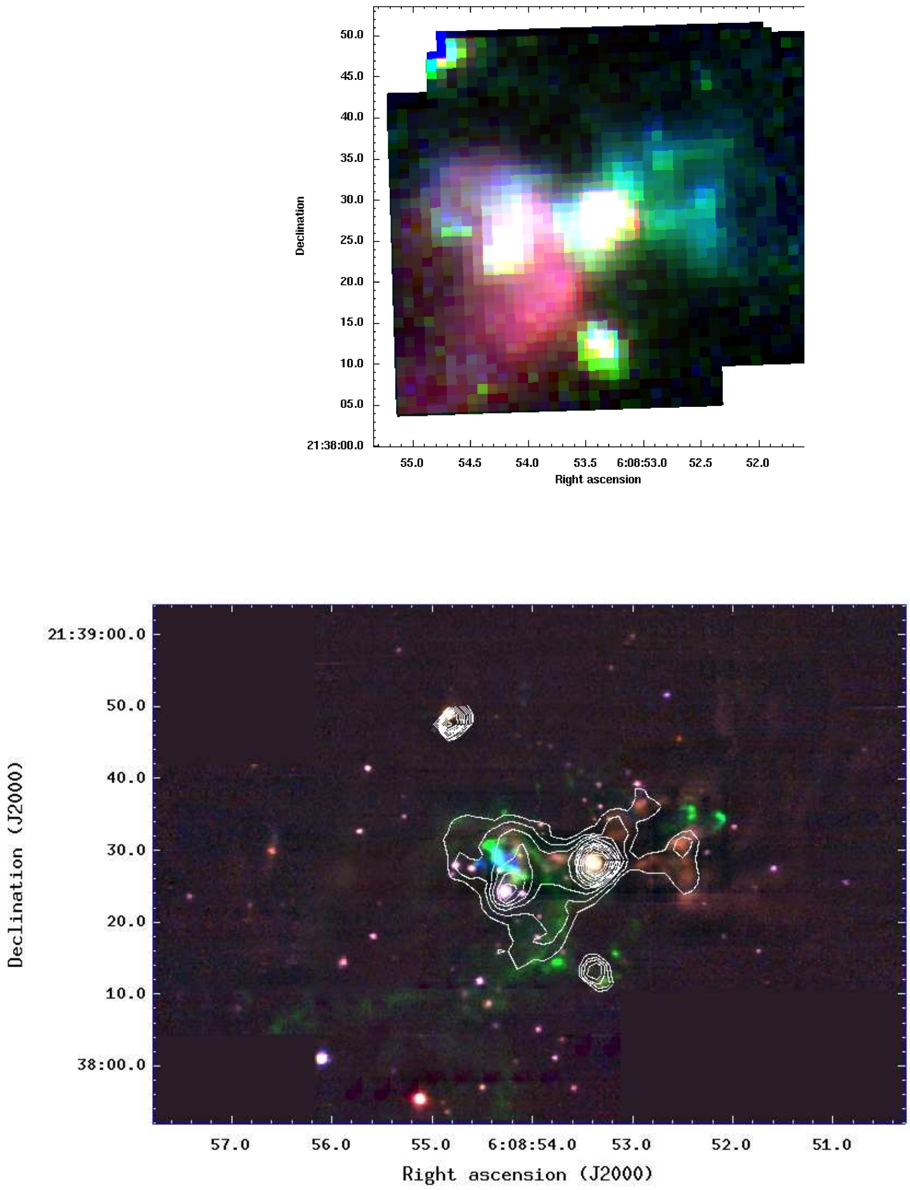

Figure 4.3 Upper panel: the 3-color composite Spitzer/IRAC image of IRAS 06058+2138. Blue is 3.6 μm, green is 4.5 μm, red is 8.0 μm. Lower panel: the 3-color composite SINFONI image. Blue is FeII (1.64 μm, line+continuum), green is H_2 (2.12 μm, line+continuum) and red is Brγ (2.16 μm, line+continuum). The contour lines are the 3.6 μm Spitzer/IRAC data.

the "hour-glass" shape region, associated with FeII emission, a large arc, and two point sources in the vicinity of the millimeter blob. Fig. 4.4 shows the location of these regions.

Molecular hydrogen emission arises in photon dominated resions (PDRs) and can also trace outflows (shocks). Since these two mechanisms populate different levels, the line diagnostics in NIR H- and K-band allow us to discriminate between these two emission mechanisms. There are several methods to characterize the H_2 emission: to analyse 1-0S(1)/2-1S(1) and 1-0S(1)/3-2S(3) ratios, to estimate the orto-to-para ratio or to perform an excitation analysis. Martín-Hernández et al. (2008) showed that analysis of an excitation diagram is the most reliable and simple way to clarify the origin of the H_2 emission.

For every selected region we extracted H- and K-band spectrum from our 3d cubes (see Fig. 4.4). In the interval from 1.45 μm to 2.45 μm we would expect to find up to 27 H_2 lines. For every detected line we estimate the line flux, line intensity and finally, column density of the upper level according to the following formula:

$$N_j = \frac{4\pi\lambda_j I}{A_j hc}, \tag{4.1}$$

where λ_j is the rest wavelength, I is the corresponding line intensity in ergs s^{-1} cm^{-2} sr^{-1}, A_j is the Einstein A-coefficient for the corresponding transition from Turner et al. (1977). In the case when H_2 is in LTE, the energy levels will be populated with a unique temperature. Thus, the relative column densities of any two levels can be expressed by the following ratio:

$$\frac{N_i}{N_j} = \frac{g_i}{g_j} e^{\frac{-(E_i-E_j)}{T_{ex}}}, \tag{4.2}$$

where g_i and g_j are the degeneracies, E_i and E_j are the energy of the corresponding upper levels in Kelvin. Energy levels are taken from the Joint Astronomy Centre (JAC) data base, where they were calculated using Dabrowski & Herzberg, (1984). From equation 4.2 we can estimate the excitation temperature by plotting the logarithm of the column density and the appropriate statistical weight ratio against the upper level energy. The slope of the straight line fitted to the data equals to -1/T_{ex}. Using the formulae from Zhang et al. (1998) we calculate total column densities for all H_2 regions. Together with the estimated temperatures they are presented in the Table 4.1.

In Fig. 4.5 we show excitation diagrams for the six regions. In these diagrams different symbols indicate different vibrational levels, the solid line in all plots gives us the fit to all data points, the dashed line fits only the 1-0 S transitions. In the case of point sources 1 and 2 and two bowshocks, all points can be fitted with one line, i.e. represented by a single temperature. The shock1 and shock2 regions are located within the cone, which is formed by 3.6 μm continuum and Brγ emission and, both regions associated with FeII emission (see Fig. 4.3). Taking this into account, we conclude that both of them are thermally excited. In the case of the point sources we cannot make any conclusion about an excitation mechanism in it, since we detect only 1-0 lines and their shape can be caused both by shock emission and fluorescence.

For the "hour-glass" region we expect to find a single-temperature solution since it is coincides with strong FeII emission and its shape may indicate presence of an outflow. However, the excitation diagram shows clearly two temperature components. In such a case, we conclude that both mechanisms may excite the molecular hydrogen emission. For the arc a single-component model does not fit the data. The 1-0 levels show excitation temperature T_{ex}=1440 K. The inclusion of the higher 2-1 and 3-2 levels increases the best-fitting temperature to T_{ex}=2950 K. Such behavior indicates that the most likely excitation mechanism in the arc is fluorescence.

An additional parameter which can help us to understand the nature of the molecular hydrogen regions is their velocity. Shock 1 and shock 2 have a redshifted velocities, while "hour-glass" region has a blueshifted velocity. Both point sources are blueshifted, with point 1 having the largest value of -26±11 km/s.

4.5 Stellar content

In this section we will use near-IR SINFONI spectroscopy data to make a spectral classification of the cluster members. To make a first impression about the stellar population in the region, we use previously obtained near- and mid-IR data. In the Fig. 4.6, we present K vs. (J-K) color-magnitude diagram (CMD) for IRAS 06058+2138. Data for this diagram were taken from Bik (2004), who obtained J- and K-band images using SOFI at the NTT telescope. Different symbols in the plot indicate stars of different spectral types, as discussed further in this section. Star symbols correspond to the featureless stars, triangles - to the YSOs, squares to the late type stars, the diamond

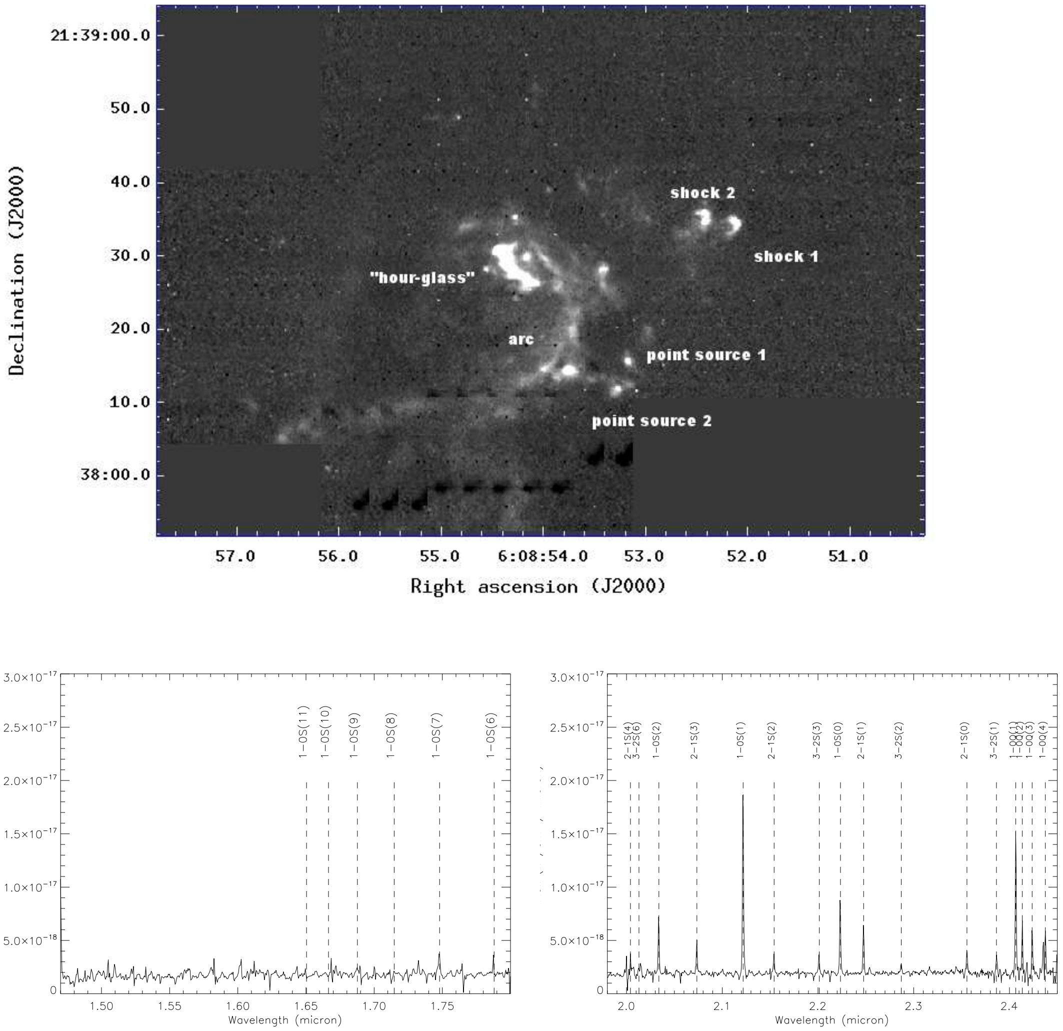

Figure 4.4 Molecular hydrogen map indicating the position of interesting regions (upper panel). Molecular hydrogen spectra for the large arc in H- (left lower panel) and K-bands (right lower panel). Dashed lines in the lower plots indicate different vibrational transitions.

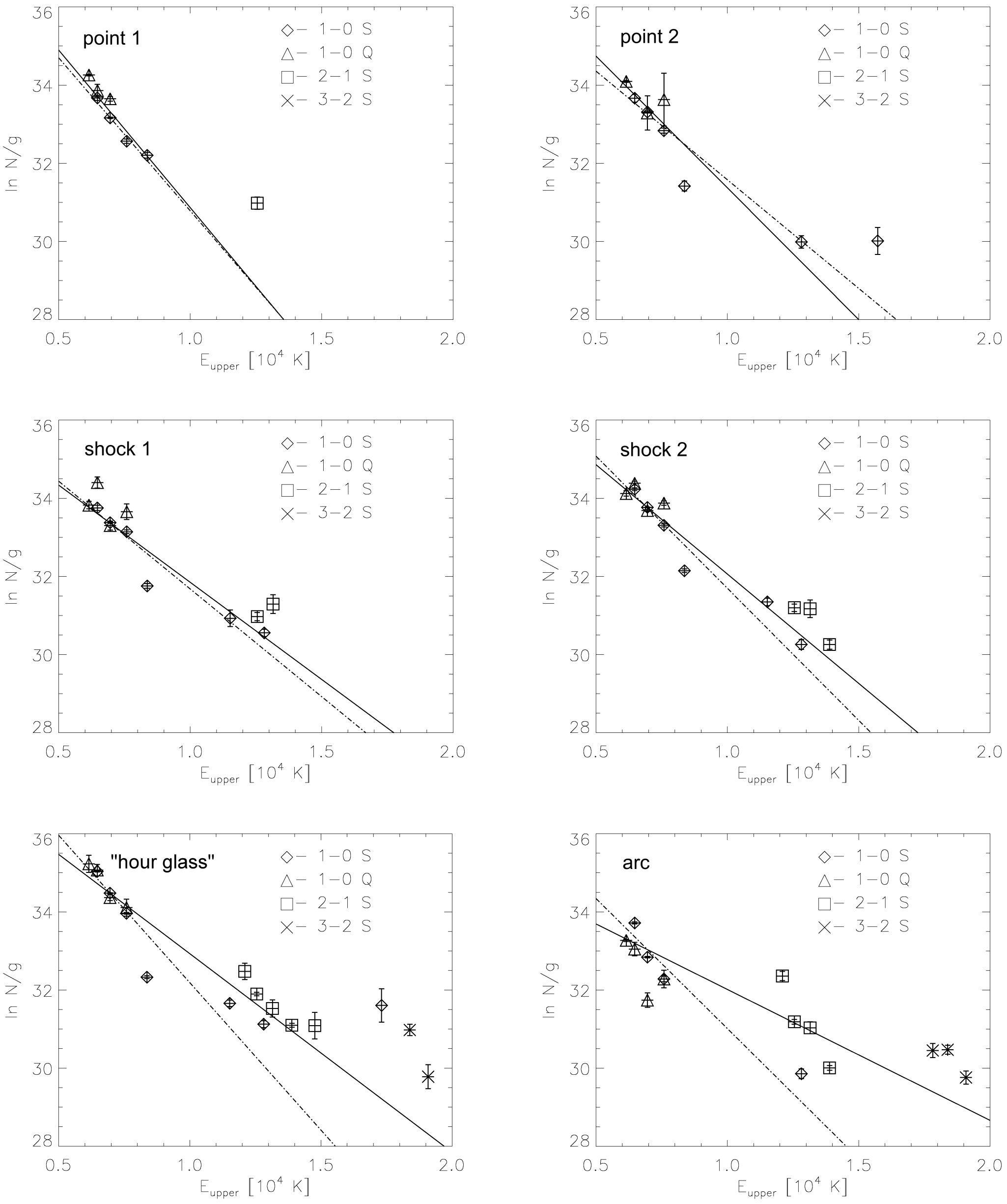

Figure 4.5 Excitation diagrams for six H_2 regions: point source 1 and point source 2 (two upper panels), shock 1 and shock 2 (two middle panels), "hour-glass" region (lower right panel) and the large arc (lower left panel). In all diagrams the solid line corresponds to the single temperature fit, the dashed-dotted line fits only 1-0 S transitions. Using the excitation analysis we cannot determine explicitly the excitation mechanism for point sources 1 and 2. Analysis of the shock 1 and 2 regions suggests that they are thermally excited and thus, can be outflows. In the case of the "hour-glass" region, most likely that both thermal and non-thermal emission affect this region, while for the arc the excitation diagram suggests that the main excitation mechanism is UV fluorescence.

Table 4.1. Physical properties of the molecular hydrogen regions.

Region	T_{rot} (K)	$N(H_2)$ (cm^{-2})	v_{lsr} (km/s)
point 1	1200±50	$1.7\pm0.5\times10^{18}$	-26±11
point 2	1300±70	$1.4\pm0.4\times10^{18}$	-8±11
shock 1	2000±90	$4.7\pm0.8\times10^{17}$	9±13
shock 2	1780±50	$8.8\pm1.1\times10^{17}$	9±11
"hour-glass"	1850±30	$1.6\pm0.2\times10^{18}$	-10±10
arc	2560±50	$2.2\pm0.1\times10^{17}$	-3±11

to the OB star. The CMD shows a large spread in J-K colors: from 0 to 8 mag. Such large variations in color may indicate large extinction variations in the region. Objects, which are located around J-K=1 mag, probably are foreground stars with very little extinction. In the plot we can see several bright objects with K ∼ 10 mag. However, the most of the stars are quite faint and have K-band magnitude higher than 14 mag.

In the mid-IR Spitzer/IRAC image we identify three point sources (see Fig 4.3). Central source corresponds to the AFGL 5180, the source on the south to the millimeter cluster and the third to the OB star inside the molecular hydrogen bubble. To analyse the stellar content in Spitzer/IRAC images, Megeath et al. (2004) and Allen et al. (2004) proposed a color criterium. In the case of IRAS 06058+2138, all objects have [3.6]-[4.5]>0.8 and [5.8]-[8.0]>1.1 Thus, we classify all three mid-IR sources as protostars (class 0 and I objects).

From the near-IR SINFONI spectroscopy data, we identified 166 point sources in the cluster. Using J- and K-band photometry data, we select the brightest stars with high signal-to-noise ratio. This reduces our sample to 31 stars. Among them, we identify one B star, 9 late type stars and 3 stars with a strong red slope and Brγ emission line in the spectra. The rest of the 18 stars we determine as featureless. Most of them have quite low signal-to-noise ratio, what do not allow us to recoqnize any features in their spectra. Also some part of the featureless spectra corresponds to bright extended emission rather than to point sources. The location of the classified stars is shown in the Fig. 4.7. Their parameters are presented in Table 4.3.

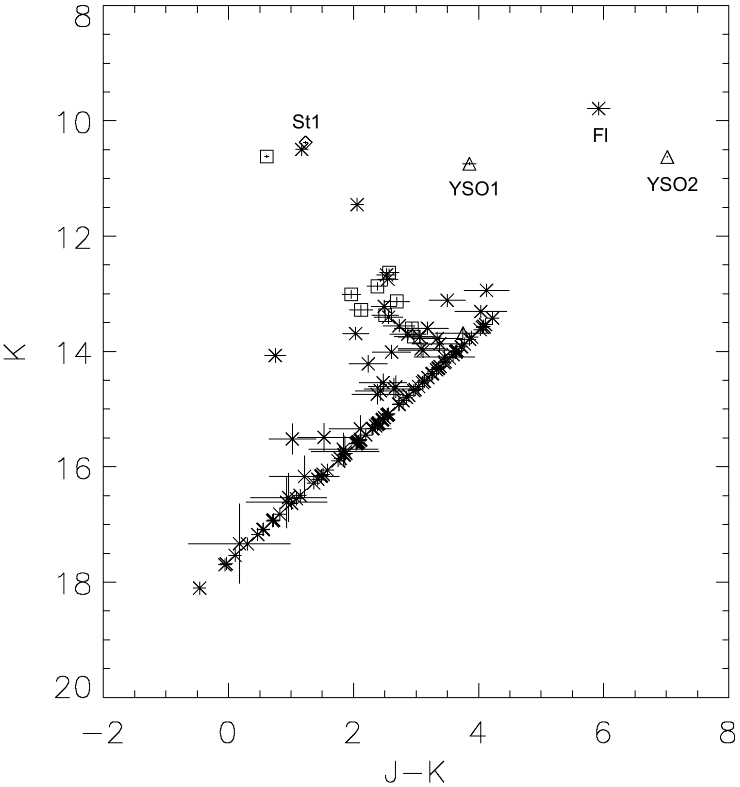

Figure 4.6 K vs. (J-K) color-magnitude diagram. Different symbols indicate different spectral types. Star symbols correspond to the featureless stars, triangles - to the YSOs, squares - to the late type stars, diamond - to OB star. Classification of the stars is presented in Sections 4.5.1-4.5.3.

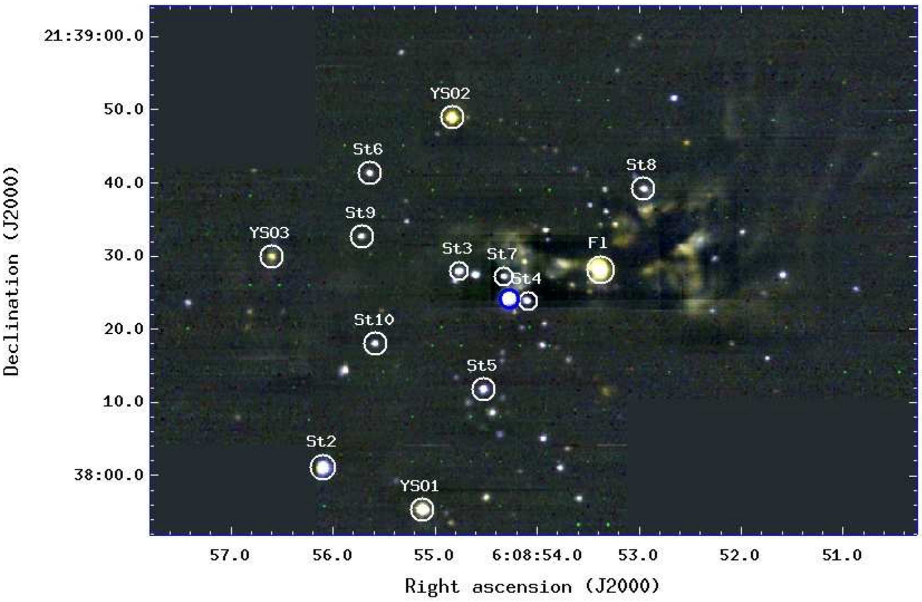

Figure 4.7 3-color composite SINFONI image. Blue is continuum at 1.64 μm, green is continuum at 2.12 μm and red is continuum at 2.16 μm. The circles mark the position of the classified stars. The blue circle corresponds to the St1 star.

4.5.1 OB-stars

The main features in OB star spectra are the HeI and HI (Bracket series) absorption lines. We identify only one object, which has such a spectra. The star is located inside the molecular hydrogen bubble and its position is marked with a blue circle in the Fig. 4.7. Alvarez et al. (2004), using near-IR speckle imaging, showed that this star is double with a fainter second companion. Figure 4.8 shows the normalized H- and K-band spectrum of this source. The dashed lines in the plot indicate the position of the Br10-13 and Brγ lines. In both bands, HeI absorption lines are not detected. We measure the equivalent width of the Bracket lines (see Table 4.2) and use the classification scheme by Hanson et al. (1996, 1998) to determine the spectral class of the star. This results in a B4V-B8V spectral type.

4.5.2 Late-type stars

Among all detected stars we identify 9 of them as late-type stars. Their spectra in H- and K-bands are presented on the Fig. 4.9. For stars from F to M spectral type

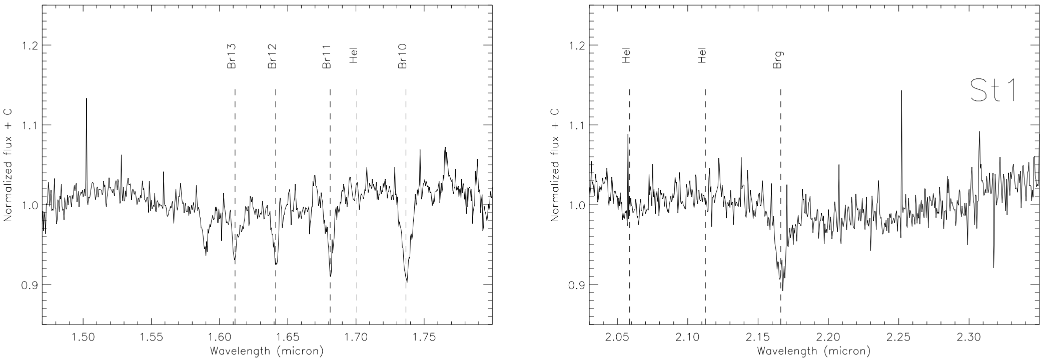

Figure 4.8 Normalized spectra of the OB star in H- (left) and K-bands (right). Dashed lines indicate the position of the Br10-13, Brγ and HeI lines.

Table 4.2. Parameters of OB star.

Star	Br11 (1.68 μm)	Brγ (2.166 μm)	Spectral type
St1	5.6 Å	9.5 Å	B4V-B8V

the most prominent lines in the H band are MgI absorption lines, in the K band - series of CO absorption lines dominate the spectrum. In some spectra together with absorption features we can see also molecular hydrogen emission lines (e.g. stars St4, St7). This emission comes from the surroundings of the stars. To classify late type stars we compare the SINFONI H and K-band spectra with the reference spectra. As a reference, we use data from Cushing et al. (2005) and Rayner et al. (2009). Based on these spectra, we classified three objects as pre-main sequence stars and others as main sequence stars (Table 4.3). Their positions are marked with circles in the Fig. 4.7.

Knowing the spectral type of stars we can plot them in the HR diagram, thus, estimating age of the cluster and characterize its stellar content. But before we have to perform several intermediate steps to determine their effective temperatures and absolute magnitudes. We apply the relation from Kenyon & Hartmann (1995) for main sequence stars and from Hillenbrand (1997) for PMS stars, to convert spectral type into effective temperature. To determine the absolute magnitudes we use the following equation:

$$M_k = (m_k - A_k) + 5 - 5\log_{10} d, \tag{4.3}$$

as the distance to the cluster, we adopt d=1760pc (Oh et al., 2010). An extinction A_k value can be expressed as:

$$A_k = 0.61884[(m_j - m_k) - (m_j - m_k)_0], \tag{4.4}$$

where $(m_j - m_k)_0$ is intrinsic color from Koornneef (1983), $(m_j - m_k)$ is a measured value from Bik (2004). The resulting HR diagrams are presented in the Fig. 4.10. On the left panel, the solid lines correspond to pre-main sequence evolutionary tracks from Da Rio et al. (2009) for 1.5, 2 and 3 solar masses. Comparing position of the late type stars on the diagram with the evolutionary tracks, we see that our objects have masses around 1.5 - 2 $M_\odot$. On the right panel, the solid lines show the isochrones from Da Rio et al. (2009) between 0.3 and 10 Myr. Most of the points span between 1 and 3 Myr. However, a small number of classified stars to not let us to determine age of our cluster more precise.

4.5.3 Young Stellar Objects and featureless stars

Among the 31 selected stars with high S/N we distinguish three objects with the strong red slope and Bracket emission lines in the spectra (YSO1, YSO2, YSO3). and one very bright object with featureless spectra (AFGL 5180). All four sources show extremely high J-K values on the K vs. (J-K) diagramm (Fig.4.6). Star YSO1 and star YSO2 have been observed before by Bik et al. (2006) and were identified as Young Stellar Objects (YSOs). The SINFONI spectra confirm the young nature of these objects. YSO1 shows the most remarkable spectra (see Fig. 4.11). There are bracket lines in the H-band and strong Brγ emission at 2.12 μm. Around 2.4 μm there are also the Pfund lines. The pfund lines in the K-band are only emitted at high density ionized gas ($N_e \sim 10^8$ cm^{-3}), since they come from very high transitions in the hydrogen atom. The electron falls down from level 30 to level 5. The level 30 in the atom needs to be populated, which only happens if the density is high. The other bracket lines are coming from level 14 at maximum, and need a bit less dense material. These lines could be formed in the ionized surface of the disk around the massive Young Stellar objects.

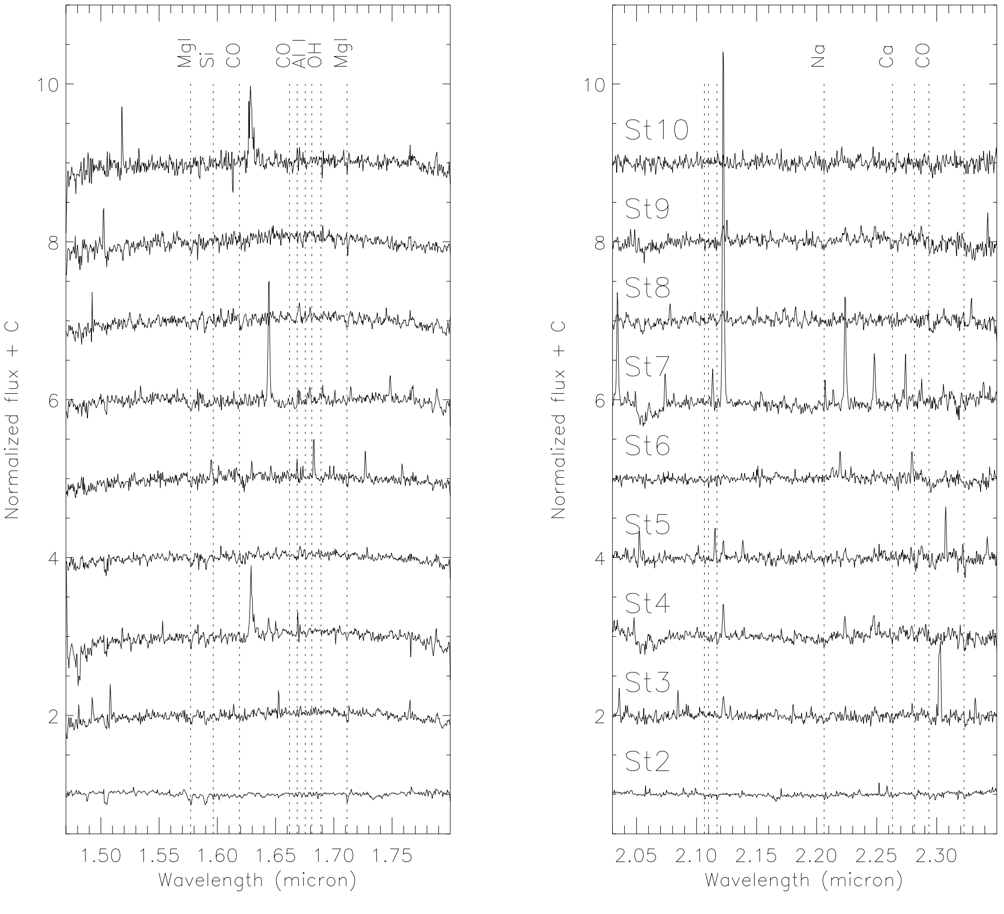

Figure 4.9 Normalized spectra of the late type stars in H- (left) and K-bands (right).

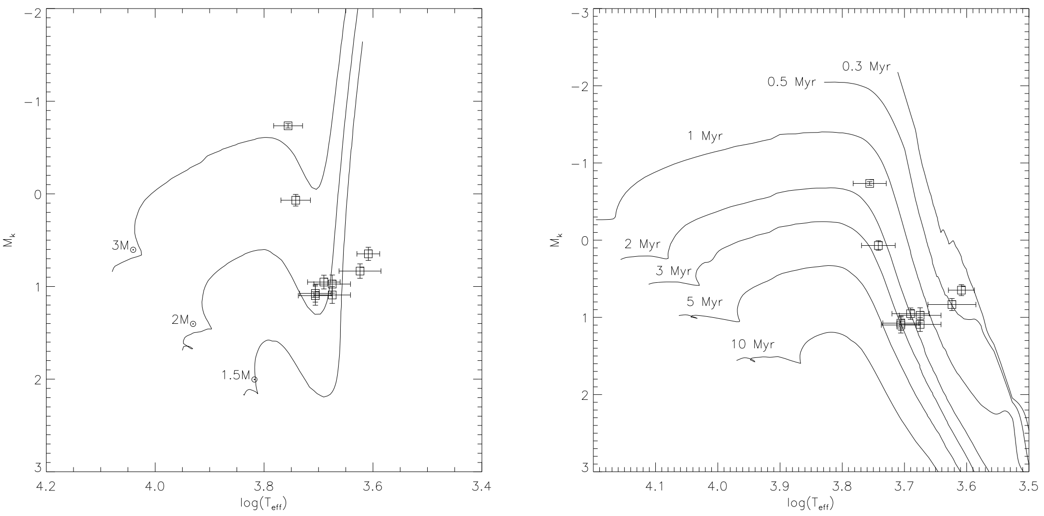

Figure 4.10 HR diagrams. The K-band magnitudes are corrected for the extinction and distance. Squares represent late type stars. Solid lines are the pre-main sequence evolutionary tracks from Da Rio et al. (2009) (left panel). The same data, but overplotted with the isochrones from Da Rio et al. (2009) (right panel).

Table 4.3. Photometric and spectroscopic properties of the sources located in the SINFONI field of view.

Star	R.A. (J2000.0)	Decl. (J2000.0)	K (mag)	J-K (mag)	Sp. type	T$_{eff}$ (K)
St1	06:08:54.2	21:38:24.0	10.37±0.02	1.23±0.03	B4-8 V	17000 - 11900
St2	06:08:56.1	21:38:01.1	10.61±0.02	0.61±0.03	G6.5±1 V	5700±360
St3	06:08:54.7	21:38:27.9	12.63±0.06	2.56±0.15	G8±1 V	5520±355
St4	06:08:54.1	21:38:23.8	12.87±0.07	2.37±0.16	K7±1 V	4060±200
St5	06:08:54.5	21:38:11.6	13.01±0.07	1.96±0.14	K2±1 V	4900±350
St6	06:08:55.6	21:38:41.4	13.13±0.07	2.69±0.20	K6±2 III	4205±390
St7	06:08:54.3	21:38:27.0	13.28±0.09	2.12±0.18	K1±2 V	5080±350
St8	06:08:52.9	21:38:39.2	13.37±0.09	2.50±0.21	K3±2 III	4730±380
St9	06:08:55.7	21:38:32.5	13.60±0.09	2.93±0.28	K3±2 V	4730±380
St10	06:08:55.5	21:38:18.0	13.74±0.10	2.96±0.31	K1±2 III	5080±380
YSO1	06:08:55.1	21:37:55.5	10.74±0.02	3.85±0.11		
YSO2	06:08:54.8	21:38:49.0	10.62±0.00	7.01±0.00		
YSO3	06:08:56.6	21:38:30.0	13.68±0.10	3.75±0.44		
Fl	06:08:53.3	21:38:28.1	9.78±0.01	5.91±0.18		

YSO2 locates in the nothern part of the cluster. As in the case of YSO1, in the YSO2 spectrum we detect series of Bracket emission lines in the H-band and Brγ emission in the K-band, but they are weaker. YSO2 is at the corner of our Spitzer/IRAC map. However, there is mid-IR emission on the edge of the image, which coinsides with the near-IR object. The star YSO3 has a more noisy spectra and shows weaker Brγ line, however on the 3 color image (see Fig. 4.2) it appears as a point source with elongated Brγ emission in the north-south direction. Such shape can indicate the presence of an outflow.

The brightest featureless star is the previously studied AFGL 5180. This source shows emission also at millimeter and mid-IR wavelengths. According to the mid-IR color-color criteria it can be classified as a protostar. Longmore et al. (2006), using high-resolution mid-IR observations, showed that this source has multiple nature and hide several young embedded objects. In the Fig. 4.2 (lower panel) we zoom to this source and mark the position of Longmore sources with crosses. Objects G188.95:1 1, G188.95:1 2 and G188.95:1 3, in their notation, coincide with the near-IR featureless object. G188.95:1 4 is located several arcseconds away and there is no infrared counterpart for it. However, it corresponds to the position of the millimeter secondary source. Around this multiple system we detect signatures of several outflows. It is two bowshocks on the west, FeII and Brγ extended emission along the outflow cone and the "hour-glass" region (e.g. Fig. 4.3). The millimeter source also associated with SiO emission (Javier Rodon, PhD thesis). Thus, we can conclude that stars are actively form in this region and one (or several) of the mid-IR objects from Longmore et al. (2006) may drive outflow(s).

The IRAS 06058+2138 point source is located inside the molecular hydrogen bubble. It was detected also in mid-IR survey by Longmore et al. (2006) at 7.9-18.5 μm. According to their study, we indicate the position of the source in the Fig. 4.2. In this image and also in Fig. 4.7 we can see thant in the near-IR wavelength there are several weak objects nearby the IRAS source, but it is not possible to connect neither of them with it. In Spitzer/IRAC colors we identify elongated emission source, which corresponds to the position of IRAS 06058+2138. With the color-color criteria we identify this object as a protostar. Probably, at 3.6-8.0 μm also OB star contributes in the emission. However at 8.0 μm emission peak is clearly shifted in the direction of the IRAS source position. Thus, we can conclude, that IRAS 06058+2138 is deeply

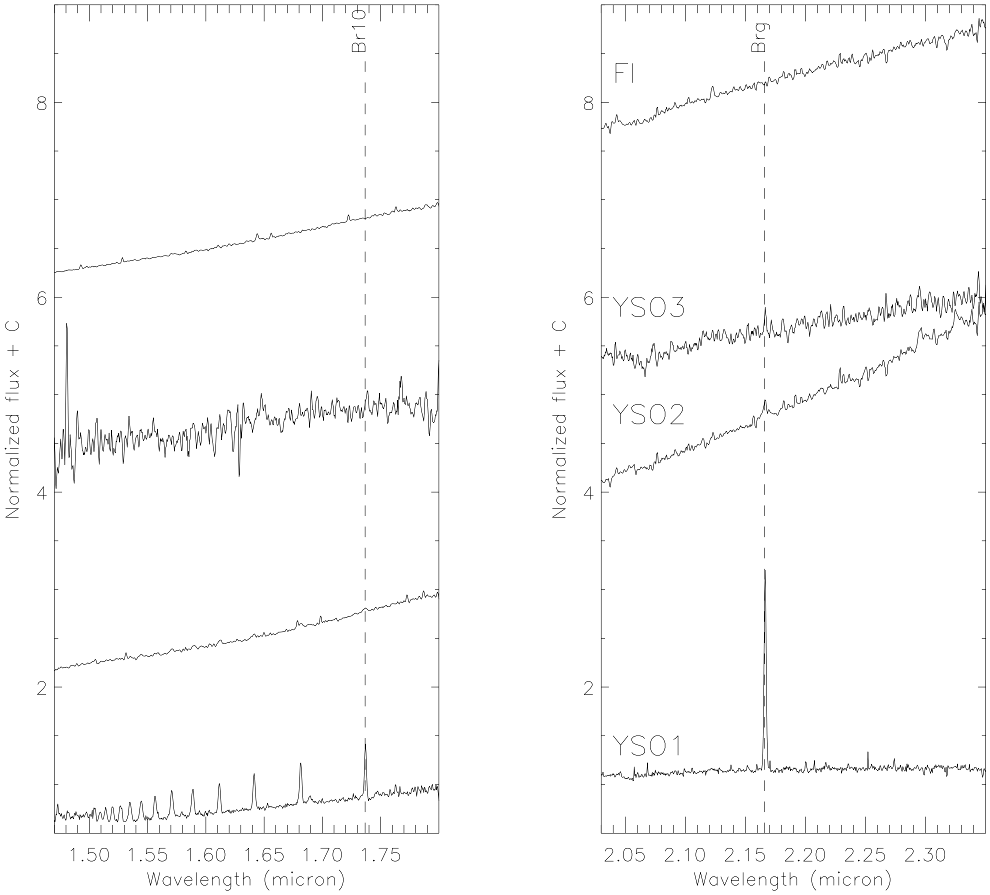

Figure 4.11 Normalized spectra of the two YSOs and featureless star in H- (left) and K-bands (right).

embedded source, dominated by far- and mid-IR emission and not clearly visible in near-IR.

4.6 Discussion

In the previous sections we have described the morphology and the stellar content of IRAS 06058+2138. We identified three star-forming regions: a young millimeter cluster, AFGL 5180, associated with outflows and a more evolved cluster on the east, surrounded by the molecular hydrogen bubble. Here, based on the obtained results, we discuss the outflow activities and possible star-formation mechanism of the region.

4.6.1 What is the outflow(s) direction and where is the driving source?

The outflow in the region was first detected by Snell et al. (1988). Their single-dish observations showed the presence of the blueshifted ^{12}CO emission near AFGL 5180. However, the redshifted emission was confused by a second velocity component, and the geometry of the outflow could not be determined. Then, using infrared polarization images, Tamura et al. (1991) identified two bipolar nebulae, and hence, two outflows, around NIRS 1 (AFGL 5180). They also conclude, that this near-IR source drives both outflows. Following study showed that NIRS 1 hides several sources (Longmore et al., 2006), which makes the whole picture more complicated.

Taking into account results from the previous observations and analyzing the SINFONI, SMA, and Spitzer/IRAC data, we can now determine, which of the mid-IR sources drives an outflow and better determine its direction. In the Fig. 4.3, we can see that structure at the right side from the AFGL 5180, which was identified by Tamura et al. (1991) as bipolar nebulae, coincides with 3.6 μm Spitzer/IRAC emission and Brγ emission. This structure forms an "outflow cone" with H_2 bowshocks inside. Also, on the opposite side from the AFGL 5180, we detect quite strong FeII emission. The H_2 analysis of the "hour-glass" region nearby show, that both UV fluorescence and shock may affect this region. This signature indicates the presence of the outflow. Investigation of the velocity structure shows that two bowshocks on the west are redshifted, while the region near FeII emission, on the contrary, has systematically blueshifted velocities, which is in agreement with the Snell et al. (1988) detection.

Thus, we identify one outflow component, moving away from us, in the direction of two H_2 bowshocks. The second outflow component points to the FeII region and moves toward us. We assume the weaker millimeter counterpart, which is associated with SiO emission, as a driving source. However, we also do not exclude the possibility that the three sources hidden within AFGL 5180 may give contribution to this outflow, or even drive their own outflows in other directions.

4.6.2 Triggered star-formation?

Based on molecular line observations, Carpenter et al. (1995a,b) suggested that the dense cores along S247 (see Fig. 4.1) were formed in "swept-up shells of molecular gas". Thus, proposing that star formation in IRAS sources 06061+2151, 06058+2138 and 06056+2131 was triggered by the expanding HII region. In this case, star formation in IRAS 06058+2138 cluster would go from the west to the east. Now, using our multi-wavelength data, ranging from near-IR to millimeter, we can test the hypothesis about triggered star formation scenario in this region.

Using near-IR SINFONI, mid-IR Spitzer and millimeter SMA data, we can identify three places of star formation. The first and most evolved region is the cluster within the H_2 bubble, where stars have been already formed. We identified 9 of them as late type G and K type pre and main sequence stars. The brightest binary component shows spectra typical for B4-8 V star and can be an exciting source for the large molecular hydrogen bubble around. The second region is the bright near-IR multiple system (AFGL 5180 or NIRS 1 in previous studies) on the edge of the H_2 bubble. It consists of several embedded objects and shows presence of outflows. Since stars are still actively forming here, we assume that this region is younger. The youngest third region is the millimeter cluster on the south-west associated with strong SiO emission. It corresponds to the mid-IR emission source but is not visible at near-IR wavelength. From the analysis of these three regions we can conclude, that in IRAS 06058+2138 star-formation goes not from the west to the east, but in the opposite direction - from the east to the west. This would suggest that star-formation cannot be caused by expanding HII region on the west side of the cluster.

Thus, the presence in IRAS 06058+2138 of several star-forming regions at different evolutionary stages indicates sequential star formation. However, the location of these regions cannot be explained by a triggering scenario.

4.7 Conclusions

In this chapter we presented a multiwavelength study of the young cluster IRAS 06058+2138. We combined SINFONI integral field spectroscopy data with mid-IR Spitzer/IRAC images and SMA millimeter continuum maps. The results of our study can be summarized as follows:

In IRAS 06058+2138, we can distinguish three regions of star-formation at different evolutionary stages. The central bright near-IR source AFGL 5180 represent a young multiple system. At least one of its sources drives an outflow in north-east and south-west directions. To the east from AFGL 5180 there is an older cluster, where stars already have been formed. Using millimeter and mid-IR data, we identify a third - the youngest star forming regions on the south. This region is still embedded and not visible in near-IR.

With SINFONI spectroscopy data we classified 31 sources in the field of view. One of them we classified as B4V - B8V star. Nine stars are G and K pre- and main sequence stars with masses between 1.5 and 2 $M_{\odot}$. In addition, two objects were identified as YSOs and the rest are featureless stars. We estimate an age of the cluster around 1-3 Myr, however with the small sample of classified stars we can not determine it very precisely.

Analising previously obtained data and results of our study, we can definitely say that the sequential star-formation takes place in this region. However, location of the clusters in IRAS 06058+2138 do not let us to confirm the triggered scenario.

5

Conclusions and future prospects

This thesis is devoted to the investigation of two stages of massive star formation. The first phase is represented by infrared dark clouds (IRDCs). Their properties (low temperature, high column density, etc.) imply that they are ideal sites for the very early stages of massive star formation. A later stage relates to embedded, newly formed massive stars in typical cluster environments. The main results of this thesis are the following:

- Using 1.2 mm continuum data from the SIMBA bolometer array at the SEST telescope and mid-IR Spitzer/GLIMPSE images, dust properties of a new sample of southern IRDCs were investigated. Analysis of the dust emission and extinction enables us to determine the masses and column densities, which are important quantities for characterizing the initial conditions of massive star formation. The total masses of the IRDCs were found to be in the ranges from 150 to 1150 $M_\odot$ (emission data) and from 300 to 1750 $M_\odot$ (extinction data). Thus, the IRDCs in our sample have the potential to form not only low- and intermediate-mass stars, but can also be the birth places of massive stars. The derived peak column densities are between 0.9 and 4.6 $\times 10^{22}$ cm^{-2} (emission data) and 2.1 and 5.4 $\times 10^{22}$ cm^{-2} (extinction data). A comparison of our results with previously obtained data for low-mass starless cores show a clear trend for IRDCs to have systematically higher column densities. By taking the effects of spatial resolution into account and restoring the column densities derived from the dust emission to a linear resolution of 0.01 pc, we calculate peak column densities of $3-19$

$\times 10^{23}$ cm^{-2}. These peak column densities are beyond the column density threshold of 3.0 $\times 10^{23}$ cm^{-2} advocated by theoretical considerations for massive star formation. Thus, the values of column densities derived for the selected IRDC sample imply that these objects are good candidates for objects in the earliest stages of massive star formation. Apart from the investigation of the properties of IRDCs, the use of two different methods allows us to compare millimeter and mid-IR techniques, and to work out the advantages and disadvantages of each. In this work, we demonstrated that while the mid-IR extinction method provides a higher spatial resolution and is independent of temperature, it is unreliable at very high extinction values (and column densities) beyond A_V values of roughly 75 mag. The millimeter technique is, on the contrary, sensitive to the column densities $\geq 10^{24}$ cm^{-2}. However, the temperature dependence comes in and a resolution, comparable with Spitzer/GLIMPSE data, can only be reached with interferometric techniques.

- Millimeter continuum and mid-IR data give us information about dust properties. In order to get information about the gas properties and the chemical composition of IRDCs, we performed molecular line observations towards 15 IRDCs with the 22-m Mopra radio telescope. In total, 13 molecular species comprising N_2H^+, ^{13}CS, CH_3CN, HC_3N, HNC, HCO^+, HCN, HNCO, C_2H, SiO, $H^{13}CO^+$, $H^{13}CN$ and CH_3C_2H were observed in the frequency range between 86 and 93 GHz for all targets. HNC, HCO^+ and HNC emission was detected in all clouds and N_2H^+ in all IRDCs except one. The presence of SiO emission and the complex shape of the HCO^+ emission line profiles indicate possible infall and outflow motions and the beginning of star formation activity, at least in some parts of the IRDCs. Comparison between the line width and integrated intensities of the IRDCs and those of low-mass dark clouds show several times higher values for IRDCs. Broader and more intense lines mean that in IRDCs we have more turbulent conditions in comparison with low-mass clouds. We calculated molecular abundances of all detected species and made a comparison with previously obtained values for low-mass pre-stellar cores and high-mass protostellar objects. We show a tendency for IRDCs to have molecular abundances similar to those of low-mass pre-stellar cores on the scale of our single-dish observations. However, we explicitly mention that the uncertainties for derived IRDC molecular abundances, as well as for the comparison low– and high–mass objects in the literature are probably around one order of magnitude. Therefore, further studies are needed to make stronger conclusions about the evolutionary status of IRDCs.

- The last chapter of this thesis is devoted to the study of the already formed, but still embedded cluster IRAS 06058+2138. To form a more complete picture of the star formation processes in the region, we combined near-IR SINFONI spectroscopy data with mid-IR Spitzer/IRAC images and SubMillimeter Array (SMA) millimeter interferometry maps. To reconstruct also the large-scale structure of the surroundings, we used SCUBA and NVSS data.

  In IRAS 06058+2138 we identified three star-forming regions at different evolutionary stages. Using SINFONI spectroscopy data we analyse the stellar content of the most evolved cluster, where stars have already formed. One star was classified as B4V - B8V star, nine - as G and K pre- and main sequence stars. Clear Brγ emission lines in three spectra let us identify these objects as YSOs. All other objects were classified as featureless. The age of the cluster was estimated to be in the range 1 - 3 Myr. On the edge of the molecular hydrogen bubble surrounding this cluster, there are two younger star-forming regions: AFGL 5180 on the west side, and a millimeter cluster on the south. These two regions show the presence of outflows, indicating beginning of star-formation activity. Comparing the relative age of these clusters and their location, we conclude that sequential star-formation is taking place in IRAS 06058+2138.

  With this study we also show the importance of the multiwavelength approach. Combining data at different wavelength allows us to investigate both more evolved stellar population and very young embedded objects, and, hence, to reconstruct the star-forming history of such complex regions.

5.1 Prospects for the future work

Below we outline a few further directions for the research, based on what is done in this thesis:

5.1.1 Further understanding of the nature of IRDCs.

Since IRDCs were discovered as dark features seen as a silhouette against the bright galactic background in the mid-IR, they were assumed to be cold quiescent clouds without any star-formation activity in them. For this stage we wanted to know if stars already form there. Subsequent millimeter single-dish and interferometric studies show that many IRDCs are in fact actively forming stars. Quiescent IRDCs, on the contrary, are rare and less understood. Thus, by now, the search for and the investigation of the youngest clouds are very important. How young are these quiescent IRDCs? Do they harbor genuine prestellar cores? Does a pronounced pre-stellar phase exist for massive star formation at all? These are the questions, which we would like to address in further studies. In order to answer these questions, we have to go further in our investigation of the chemical and physical processes in IRDCs.

One way to estimate the evolutionary status of IRDCs is to compare of their parameters with available data for other types of clouds. In Chapter 3, we showed that direct comparison of the molecular abundances can be difficult, because of the large uncertainties in different data sets. To be able to compare abundances of IRDCs with low-mass starless cores and more evolved high-mass objects, we have to perform a series of observations with one instrument for different types of sources. This will reduce uncertainties caused by different spatial and spectral resolutions.

Another way to determine the evolutionary status of IRDCs is to use chemical modeling. The first attempt to estimate the ages of IRDCs using $C^{18}O$, CS and N_2H^+ abundances and a chemical evolution code was performed by Gibson et al. (2009). However, chemical models have a number of degeneracies. To minimize them, we have to use additional criteria, like the CO depletion factor and the abundance ratios of deuterated and non-deuterated species. With this, we will be able to derive the evolutionary status of IRDCs, identify colder, and hence, younger objects more clearly.

For a better understanding of the physical processes taking place in IRDCs, high-resolution observations are necessary. Based on the results of the present study we can select a sub-sample of both quiescent and active cores and perform a more detailed study with modern instruments like Herschel and ALMA.

In the far–infrared regime, the 3.5-m Herschel Space Observatory (Pilbratt et al., 2010) currently provides us with dust emission maps of unprecedented resolution and sensitivity. The two bolometer cameras PACS (Poglitsch et al., 2010) and SPIRE (Griffin et al., 2010) on board of Herschel cover the ranges 70 – 160 μm and 250 – 500 μm, respectively, where the spatial resolution at the shortest wavelength is around 5.5 arcseconds. Thus, besides tracing the IRDC appearance in their transition from absorption to emission, Herschel enables us to search for very embedded objects in IRDCs and, for the first time, to assemble the complete SEDs of such objects that often show no discernible emission at shorter wavelengths (e.g, Henning et al., 2010). Five of the southern IRDCs from this thesis are contained in the target list of the MPIA-led Herschel Key Project EPOS (Earliest Phases of Star Formation) and are being observed in autumn 2010.

Millimeter interferometric observations in the case of quiescent regions will let us go deep enough and map starless cores, if they exist. At mid-IR wavelengths, they are not visible due to high extinction, and with single-dish millimeter observations they simply cannot be resolved. In the more evolved regions, where there is mid-IR emission or/and SiO emission, high resolution data will allow us to detect outflows and their driving sources, and, probably, accretion disks. Work in this direction can be started with existing instruments: the SMA on Mauna Kea, Hawaii, and the Australia Telescope Compact Array (ATCA) near Narrabri in the southeast of Australia. Both are interferometers with a moderate number of telescopes are capable of tracing cold dust emission as well as the emission from a large variety of molecular species. The SMA consists of eight 6-m antennas and can operate at frequencies from 180 GHz up to 700 GHz. A pioneering SMA study about the massive IRDC G28.34+0.06 was recently published (Zhang et al., 2009) and demonstrates the fruitfulness of such an approach. ATCA is currently the only millimeter interferometer in the southern hemisphere. It consists of six 22-m antennas, but can operate up to frequencies of only around 100 GHz (3 mm). The ATCA correlator has been recently refurbished (September 2010), and now has a strongly improved continuum sensitivity, as well as an enhanced versatility regarding molecular line setups. This will enable us to apply for dedicated follow-up studies at higher spatial resolution for selected objects from our southern IRDC sample. Finally, in the near future (2011), the Atacama Large Millimeter Array (ALMA) will play the main role in this field. Due to its fifty 12-m antennas, its location in one of the driest places on Earth at an elevation of 5100 m in the Chilean Atacama desert, and its multi–frequency receiver capabilities it will be the ultimate tool for high–angular–resolution research in many astrophysical fields covering cold (and warm) dust and molecular line emission.

5.1.2 Investigation of young embedded star clusters

We showed in Chapter 4 that we can reconstruct a complete picture of the star-formation processes in a region only by analysing information at different wavelengths and taking into account both large- and small-scale structures. In this thesis we focused on the investigation of the young embedded cluster IRAS 06058+2138. This is part of the larger survey aimed to study massive star formation in clustered mode. The first results of this investigation, showing the advantages of near-IR spectroscopy and its combination with data at other wavelength, are presented in the following papers by Bik et al. (2010) and Wang et al. (submitted). Continuing our study we would like to investigate other two clusters IRAS 06056+2131 and IRAS 06061+2151. Together with IRAS 06058+2138 they form a cluster complex surrounding the Sh 247 HII region. As well as for IRAS 06058+2138, SMA millimeter data are available for them. A multiwavelength analysis of all three regions will let us understand, which star-formation scenario is more appropriate here and whether they are triggered by the H II region.

To go further in understanding the stellar content of the young embedded clusters we have to use new instruments, which have larger field of view, provide us with better sensitivity, spectral and spatial resolution. High-precision astrometry techniques let us measure relative proper motions and study the internal dynamics in clusters. Hence, this enables us to distinguish cluster members from field stars (e.g Rochau et al., 2010). Using the Lucifer Multi-mode instrument for the near-IR we can perform studies of a larger sample of high-mass star-forming regions.

Bibliography

Abuter, R., Schreiber, J., Eisenhauer, F., Ott, T., Horrobin, M., & Gillesen, S. 2006, New Astronomy Review, 50, 398 63

Afonso, J. M., Yun, J. L., & Clemens, D. P. 1998, Astronomical Journal, 115, 1111 49

Allen, L. E., Calvet, N., D'Alessio, P., Merin, B., Hartmann, L., Megeath, S. T., Gutermuth, R. A., Muzerolle, J., Pipher, J. L., Myers, P. C., & Fazio, G. G. 2004, Astrophys. J., Suppl. Ser, 154, 363 73

Alvarez, C., Hoare, M., Glindemann, A., & Richichi, A. 2004, Astron. Astrophys, 427, 505 ix, 62, 65, 67, 75

Araya, E., Hofner, P., Kurtz, S., Bronfman, L., & DeDeo, S. 2005, Astrophys. J., Suppl. Ser, 157, 279 37

Bacmann, A., André, P., Puget, J.-L., Abergel, A., Bontemps, S., & Ward-Thompson, D. 2000, Astron. Astrophys, 361, 555 viii, 26, 27, 28, 30

Banerjee, R. & Pudritz, R. E. 2008, in Astronomical Society of the Pacific Conference Series, Vol. 387, Astronomical Society of the Pacific Conference Series, ed. H. Beuther, H. Linz, & T. Henning, 216–+ 29

Battersby, C., Bally, J., Jackson, J. M., Ginsburg, A., Shirley, Y. L., Schlingman, W., & Glenn, J. 2010, Astrophys. J, 721, 222 59, 108

Benjamin, R. A., Churchwell, E., Babler, B. L., Bania, T. M., Clemens, D. P., Cohen, M., Dickey, J. M., Indebetouw, R., Jackson, J. M., Kobulnicky, H. A., Lazarian, A., Marston, A. P., Mathis, J. S., Meade, M. R., Seager, S., Stolovy, S. R., Watson, C., Whitney, B. A., Wolff, M. J., & Wolfire, M. G. 2003, Publ.. Astron. Soc. Pac, 115, 953 8, 36

Benson, P. J., Caselli, P., & Myers, P. C. 1998, Astrophys. J, 506, 743 56

Bergin, E. A., Goldsmith, P. F., Snell, R. L., & Ungerechts, H. 1994, Astrophys. J, 431, 674 39, 52

Bergin, E. A., Snell, R. L., & Goldsmith, P. F. 1996, Astrophys. J, 460, 343 37

Beuther, H., Churchwell, E. B., McKee, C. F., & Tan, J. C. 2007, in Protostars and Planets V, ed. B. Reipurth, D. Jewitt, & K. Keil, 165–180 1, 2, 58

Beuther, H. & Henning, T. 2009, Astron. Astrophys, 503, 859 46

Beuther, H., Schilke, P., Menten, K. M., Motte, F., Sridharan, T. K., & Wyrowski, F. 2002, Astrophys. J, 566, 945 19, 20, 22, 27, 28

Beuther, H., Semenov, D., Henning, T., & Linz, H. 2008, Astrophys. J., Lett, 675, L33 38

Beuther, H. & Sridharan, T. K. 2007, Astrophys. J, 668, 348 46, 58

Beuther, H., Sridharan, T. K., & Saito, M. 2005, Astrophys. J., Lett, 634, L185 19, 20

Bik, A. 2004, Ph.D. Thesis, University of Amsterdam 70, 77

Bik, A., Kaper, L., & Waters, L. B. F. M. 2006, Astron. Astrophys, 455, 561 65, 77

Bik, A., Puga, E., Waters, L. B. F. M., Horrobin, M., Henning, T., Vasyunina, T., Beuther, H., Linz, H., Kaper, L., van den Ancker, M., Lenorzer, A., Churchwell, E., Kurtz, S., Kouwenhoven, M. B. N., Stolte, A., de Koter, A., Thi, W. F., Comerón, F., & Waelkens, C. 2010, Astrophys. J, 713, 883 63, 90

Blake, G. A., Sutton, E. C., Masson, C. R., & Phillips, T. G. 1987, Astrophys. J, 315, 621 58, 59

Bonnell, I. A. & Bate, M. R. 2006, Mon. Not. R. Astron. Soc, 370, 488 2

Bonnell, I. A., Bate, M. R., Clarke, C. J., & Pringle, J. E. 1997, Mon. Not. R. Astron. Soc, 285, 201 1

Bonnell, I. A., Bate, M. R., & Zinnecker, H. 1998, Mon. Not. R. Astron. Soc, 298, 93 1

Bonnet, H., Abuter, R., Baker, A., Bornemann, W., Brown, A., Castillo, R., Conzelmann, R., Damster, R., Davies, R., Delabre, B., Donaldson, R., Dumas, C., Eisenhauer, F., Elswijk, E., Fedrigo, E., Finger, G., Gemperlein, H., Genzel, R., Gilbert, A., Gillet, G., Goldbrunner, A., Horrobin, M., Ter Horst, R., Huber, S., Hubin, N., Iserlohe, C., Kaufer, A., Kissler-Patig, M., Kragt, J., Kroes, G., Lehnert, M., Lieb, W., Liske, J., Lizon, J., Lutz, D., Modigliani, A., Monnet, G., Nesvadba, N., Patig, J., Pragt, J., Reunanen, J., Röhrle, C., Rossi, S., Schmutzer, R., Schoenmaker, T., Schreiber, J., Stroebele, S., Szeifert, T., Tacconi, L., Tecza, M., Thatte, N., Tordo, S., van der Werf, P., & Weisz, H. 2004, The Messenger, 117, 17 63

Bronfman, L., Nyman, L., & May, J. 1996, Astron. Astrophys. Suppl. Ser, 115, 81 23, 37

Butler, M. J. & Tan, J. C. 2009, Astrophys. J, 696, 484 108

Carey, S. J., Clark, F. O., Egan, M. P., Price, S. D., Shipman, R. F., & Kuchar, T. A. 1998, Astrophys. J, 508, 721 3, 10, 35, 56, 108

Carey, S. J., Feldman, P. A., Redman, R. O., Egan, M. P., MacLeod, J. M., & Price, S. D. 2000, Astrophys. J., Lett, 543, L157 2, 3, 108

Carpenter, J. M., Snell, R. L., & Schloerb, F. P. 1995a, Astrophys. J, 445, 246 ix, 61, 64, 66, 83

—. 1995b, Astrophys. J, 450, 201 61, 64, 83

Caselli, P., Benson, P. J., Myers, P. C., & Tafalla, M. 2002, Astrophys. J, 572, 238 37

Caswell, J. L., Vaile, R. A., Ellingsen, S. P., Whiteoak, J. B., & Norris, R. P. 1995, Mon. Not. R. Astron. Soc, 272, 96 61

Chambers, E. T., Jackson, J. M., Rathborne, J. M., & Simon, R. 2009, Astrophys. J., Suppl. Ser, 181, 360 38, 46, 47, 48, 60, 65, 108

Chen, H., Liu, S., Su, Y., & Zhang, Q. 2010, Astrophys. J., Lett, 713, L50 108

Clark, P. C., Klessen, R. S., Bonnell, I. A., & Smith, R. J. 2008, in Astronomical Society of the Pacific Conference Series, Vol. 387, Massive Star Formation: Observations Confront Theory, ed. H. Beuther, H. Linz, & T. Henning, 208–+ 2

Codella, C., Bachiller, R., Nisini, B., Saraceno, P., & Testi, L. 2001, Astron. Astrophys, 376, 271 38

Condon, J. J., Cotton, W. D., Greisen, E. W., Yin, Q. F., Perley, R. A., Taylor, G. B., & Broderick, J. J. 1998, Astronomical Journal, 115, 1693 64

Crapsi, A., Caselli, P., Walmsley, C. M., Myers, P. C., Tafalla, M., Lee, C. W., & Bourke, T. L. 2005, Astrophys. J, 619, 379 48

Cushing, M. C., Rayner, J. T., & Vacca, W. D. 2005, Astrophys. J, 623, 1115 76

Cyganowski, C. J., Whitney, B. A., Holden, E., Braden, E., Brogan, C. L., Churchwell, E., Indebetouw, R., Watson, D. F., Babler, B. L., Benjamin, R., Gomez, M., Meade, M. R., Povich, M. S., Robitaille, T. P., & Watson, C. 2008, Astronomical Journal, 136, 2391 38, 46, 65

Da Rio, N., Gouliermis, D. A., & Henning, T. 2009, Astrophys. J, 696, 528 x, 77, 79

Dabrowski, I. & Herzberg, , G. 1984, Can. J. Phys., 62, 1639 69

Davis, C. J., Moriarty-Schieven, G., Eislöffel, J., Hoare, M. G., & Ray, T. P. 1998, Astronomical Journal, 115, 1118 66

De Buizer, J. M. & Vacca, W. D. 2010, Astronomical Journal, 140, 196 38

Devine, K. E., Churchwell, E. B., Indebetouw, R., Watson, C., & Crawford, S. M. 2008, Astronomical Journal, 135, 2095 62

Di Francesco, J., Johnstone, D., Kirk, H., MacKenzie, T., & Ledwosinska, E. 2008, Astrophys. J., Suppl. Ser, 175, 277 64

Diolaiti, E., Bendinelli, O., Bonaccini, D., Close, L. M., Currie, D. G., & Parmeggiani, G. 2000, in Presented at the Society of Photo-Optical Instrumentation Engineers (SPIE) Conference, Vol. 4007, Proc. SPIE Vol. 4007, p. 879-888, Adaptive Optical Systems Technology, Peter L. Wizinowich; Ed., ed. P. L. Wizinowich, 879–888 10

Dobashi, K., Uehara, H., Kandori, R., Sakurai, T., Kaiden, M., Umemoto, T., & Sato, F. 2005, Publ. Aston. Soc. Jpn, 57, 1 24

Draine, B. T. & Lee, H. M. 1984, Astrophys. J, 285, 89 18, 26

Du, F. & Yang, J. 2008, Astrophys. J, 686, 384 108

Egan, M. P., Shipman, R. F., Price, S. D., Carey, S. J., Clark, F. O., & Cohen, M. 1998, Astrophys. J., Lett, 494, L199+ 3

Eisenhauer, F., Abuter, R., Bickert, K., Biancat-Marchet, F., Bonnet, H., Brynnel, J., Conzelmann, R. D., Delabre, B., Donaldson, R., Farinato, J., Fedrigo, E., Genzel, R., Hubin, N. N., Iserlohe, C., Kasper, M. E., Kissler-Patig, M., Monnet, G. J., Roehrle, C., Schreiber, J., Stroebele, S., Tecza, M., Thatte, N. A., & Weisz, H. 2003, in Presented at the Society of Photo-Optical Instrumentation Engineers (SPIE) Conference, Vol. 4841, Society of Photo-Optical Instrumentation Engineers (SPIE) Conference Series, ed. M. Iye & A. F. M. Moorwood, 1548–1561 63

Fallscheer, C., Beuther, H., Zhang, Q., Keto, E., & Sridharan, T. K. 2009, Astron. Astrophys, 504, 127 19

Fazio, G. G., Hora, J. L., Allen, L. E., Ashby, M. L. N., Barmby, P., Deutsch, L. K., Huang, J., Kleiner, S., Marengo, M., Megeath, S. T., Melnick, G. J., Pahre, M. A., Patten, B. M., Polizotti, J., Smith, H. A., Taylor, R. S., Wang, Z., Willner, S. P., Hoffmann, W. F., Pipher, J. L., Forrest, W. J., McMurty, C. W., McCreight, C. R., McKelvey, M. E., McMurray, R. E., Koch, D. G., Moseley, S. H., Arendt, R. G., Mentzell, J. E., Marx, C. T., Losch, P., Mayman, P., Eichhorn, W., Krebs, D., Jhabvala, M., Gezari, D. Y., Fixsen, D. J., Flores, J., Shakoorzadeh, K., Jungo, R., Hakun, C., Workman, L., Karpati, G., Kichak, R., Whitley, R., Mann, S., Tollestrup, E. V., Eisenhardt, P., Stern, D., Gorjian, V., Bhattacharya, B., Carey, S., Nelson, B. O., Glaccum, W. J., Lacy, M., Lowrance, P. J., Laine, S., Reach, W. T., Stauffer, J. A., Surace, J. A., Wilson, G., Wright, E. L., Hoffman, A., Domingo, G., & Cohen, M. 2004, Astrophys. J., Suppl. Ser, 154, 10 63

Frieswijk, W. F., Spaans, M., Shipman, R. F., Teyssier, D., Carey, S. J., & Tielens, A. G. G. M. 2008, Astrophys. J., Lett, 685, L51 108

Frieswijk, W. W. F., Spaans, M., Shipman, R. F., Teyssier, D., & Hily-Blant, P. 2007, Astron. Astrophys, 475, 263 108

Froebrich, D., Ray, T. P., Murphy, G. C., & Scholz, A. 2005, Astron. Astrophys, 432, L67 24

Fuller, G. A., Williams, S. J., & Sridharan, T. K. 2005, Astron. Astrophys, 442, 949 37, 48, 49

Gibson, D., Plume, R., Bergin, E., Ragan, S., & Evans, N. 2009, Astrophys. J, 705, 123 4, 108

Goldsmith, P. F., Irvine, W. M., Hjalmarson, A., & Ellder, J. 1986, Astrophys. J, 310, 383 38, 52, 59

Griffin, M. J., Abergel, A., Abreu, A., Ade, P. A. R., André, P., Augueres, J., Babbedge, T., Bae, Y., Baillie, T., Baluteau, J., Barlow, M. J., Bendo, G., Benielli, D., Bock, J. J., Bonhomme, P., Brisbin, D., Brockley-Blatt, C., Caldwell, M., Cara, C., Castro-Rodriguez, N., Cerulli, R., Chanial, P., Chen, S., Clark, E., Clements, D. L., Clerc, L., Coker, J., Communal, D., Conversi, L., Cox, P., Crumb, D., Cunningham, C., Daly, F., Davis, G. R., de Antoni, P., Delderfield, J., Devin, N., di Giorgio, A., Didschuns, I., Dohlen, K., Donati, M., Dowell, A., Dowell, C. D., Duband, L., Dumaye, L., Emery, R. J., Ferlet, M., Ferrand, D., Fontignie, J., Fox, M., Franceschini, A., Frerking, M., Fulton, T., Garcia, J., Gastaud, R., Gear, W. K., Glenn, J., Goizel, A., Griffin, D. K., Grundy, T., Guest, S., Guillemet, L., Hargrave, P. C., Harwit, M., Hastings, P., Hatziminaoglou, E., Herman, M., Hinde, B., Hristov, V., Huang, M., Imhof, P., Isaak, K. J., Israelsson, U., Ivison, R. J., Jennings, D., Kiernan, B., King, K. J., Lange, A. E., Latter, W., Laurent, G., Laurent, P., Leeks, S. J., Lellouch, E., Levenson, L., Li, B., Li, J., Lilienthal, J., Lim, T., Liu, S. J., Lu, N., Madden, S., Mainetti, G., Marliani, P., McKay, D., Mercier, K., Molinari, S., Morris, H., Moseley, H., Mulder, J., Mur, M., Naylor, D. A., Nguyen, H., O'Halloran, B., Oliver, S., Olofsson, G., Olofsson, H., Orfei, R., Page, M. J., Pain, I., Panuzzo, P., Papageorgiou, A., Parks, G., Parr-Burman, P., Pearce, A., Pearson, C., Pérez-Fournon, I., Pinsard, F., Pisano, G., Podosek, J., Pohlen, M., Polehampton, E. T., Pouliquen, D., Rigopoulou, D., Rizzo, D., Roseboom, I. G., Roussel, H., Rowan-Robinson, M., Rownd, B., Saraceno, P., Sauvage, M., Savage, R., Savini, G., Sawyer, E., Scharmberg, C., Schmitt, D., Schneider, N., Schulz, B., Schwartz, A., Shafer, R., Shupe, D. L., Sibthorpe, B., Sidher, S., Smith, A., Smith, A. J., Smith, D., Spencer, L., Stobie, B., Sudiwala, R., Sukhatme, K., Surace, C., Stevens, J. A., Swinyard, B. M., Trichas, M., Tourette, T., Triou, H., Tseng, S., Tucker, C., Turner, A., Vaccari, M., Valtchanov, I., Vigroux, L., Virique, E., Voellmer, G., Walker, H., Ward, R., Waskett, T., Weilert, M., Wesson, R., White, G. J., Whitehouse, N., Wilson, C. D., Winter, B., Woodcraft, A. L., Wright, G. S., Xu, C. K., Zavagno, A., Zemcov, M., Zhang, L., & Zonca, E. 2010, Astron. Astrophys, 518, L3+ 89

Hanson, M. M., Conti, P. S., & Rieke, M. J. 1996, Astrophys. J., Suppl. Ser, 107, 281 75

Hanson, M. M., Rieke, G. H., & Luhman, K. L. 1998, Astronomical Journal, 116, 1915 75

Helmich, F. P. & van Dishoeck, E. F. 1997, Astron. Astrophys. Suppl. Ser, 124, 205 58, 59

Henning, T., Cesaroni, R., Walmsley, M., & Pfau, W. 1992, Astron. Astrophys. Suppl. Ser, 93, 525 61

Henning, T., Linz, H., Krause, O., Ragan, S., Beuther, H., Launhardt, R., Nielbock, M., & Vasyunina, T. 2010, Astron. Astrophys, 518, L95+ 89

Henning, T., Pfau, W., & Altenhoff, W. J. 1990, Astron. Astrophys, 227, 542 23

Heyer, M. H., Carpenter, J. M., & Snell, R. L. 2001, Astrophys. J, 551, 852 48

Hillenbrand, L. A. 1997, Astronomical Journal, 113, 1733 76

Hofner, P., Wiesemeyer, H., & Henning, T. 2001, Astrophys. J, 549, 425 38

Indebetouw, R., Mathis, J. S., Babler, B. L., Meade, M. R., Watson, C., Whitney, B. A., Wolff, M. J., Wolfire, M. G., Cohen, M., Bania, T. M., Benjamin, R. A., Clemens, D. P., Dickey, J. M., Jackson, J. M., Kobulnicky, H. A., Marston, A. P., Mercer, E. P., Stauffer, J. R., Stolovy, S. R., & Churchwell, E. 2005, Astrophys. J, 619, 931 18

Jackson, J. M., Finn, S. C., Chambers, E. T., Rathborne, J. M., & Simon, R. 2010, Astrophys. J., Lett, 719, L185 108

Jackson, J. M., Finn, S. C., Rathborne, J. M., Chambers, E. T., & Simon, R. 2008, Astrophys. J, 680, 349 3, 43, 108

Jimenez-Serra, I., Caselli, P., Tan, J. C., Hernandez, A. K., Fontani, F., Butler, M. J., & van Loo, S. 2010, ArXiv e-prints 108

Johnstone, D., Fiege, J. D., Redman, R. O., Feldman, P. A., & Carey, S. J. 2003, Astrophys. J., Lett, 588, L37 28, 108

Jones, P. A., Burton, M. G., Cunningham, M. R., Menten, K. M., Schilke, P., Belloche, A., Leurini, S., Ott, J., & Walsh, A. J. 2008, Mon. Not. R. Astron. Soc, 386, 117 37

Jørgensen, J. K., Schöier, F. L., & van Dishoeck, E. F. 2004, Astron. Astrophys, 416, 603 56, 58

Kalenskii, S. V., Promislov, V. G., Alakoz, A., Winnberg, A. V., & Johansson, L. E. B. 2000, Astron. Astrophys, 354, 1036 37

Kenyon, S. J. & Hartmann, L. 1995, Astrophys. J., Suppl. Ser, 101, 117 76

Klein, R., Posselt, B., Schreyer, K., Forbrich, J., & Henning, T. 2005, Astrophys. J., Suppl. Ser, 161, 361 61

Koornneef, J. 1983, Astron. Astrophys, 128, 84 77

Krumholz, M. R., Klein, R. I., McKee, C. F., Offner, S. S. R., & Cunningham, A. J. 2009, Science, 323, 754 1

Krumholz, M. R. & McKee, C. F. 2008, Nature, 451, 1082 29

Kuiper, R., Klahr, H., Beuther, H., & Henning, T. 2010a, Astrophys. J, 722, 1556 1

Kuiper, R., Klahr, H., Dullemond, C., Kley, W., & Henning, T. 2010b, Astron. Astrophys, 511, A81+ 2

Ladd, N., Purcell, C., Wong, T., & Robertson, S. 2005, Publications of the Astronomical Society of Australia, 22, 62 39

Lee, C. W., Myers, P. C., & Tafalla, M. 2001, Astrophys. J., Suppl. Ser, 136, 703 37, 48, 49, 50

Lee, M., Stanimirović, S., Ott, J., van Loon, J. T., Bolatto, A. D., Jones, P. A., Cunningham, M. R., Devine, K. E., & Oliveira, J. M. 2009, Astronomical Journal, 138, 1101 51, 108

Leistra, A., Cotera, A. S., & Liebert, J. 2006, Astronomical Journal, 131, 2571 62

Levine, E. S., Heiles, C., & Blitz, L. 2008, Astrophys. J, 679, 1288 9

Lo, N., Cunningham, M., Bains, I., Burton, M. G., & Garay, G. 2007, Mon. Not. R. Astron. Soc, 381, L30 38, 46

Lombardi, M. 2008, ArXiv e-prints 24

Lombardi, M. & Alves, J. 2001, Astron. Astrophys, 377, 1023 24

Longmore, S. N., Burton, M. G., Minier, V., & Walsh, A. J. 2006, Mon. Not. R. Astron. Soc, 369, 1196 ix, 62, 65, 67, 80, 82

Marcelino, N., Brünken, S., Cernicharo, J., Quan, D., Roueff, E., Herbst, E., & Thaddeus, P. 2010, Astron. Astrophys, 516, A105+ 56

Marcelino, N., Cernicharo, J., Tercero, B., & Roueff, E. 2009, Astrophys. J., Lett, 690, L27 56

Mardones, D., Myers, P. C., Tafalla, M., Wilner, D. J., Bachiller, R., & Garay, G. 1997, Astrophys. J, 489, 719 49

Marshall, D. J., Joncas, G., & Jones, A. P. 2009, Astrophys. J, 706, 727 108

Martín-Hernández, N. L., Esteban, C., Mesa-Delgado, A., Bik, A., & Puga, E. 2008, Astron. Astrophys, 482, 215 69

Mathis, J. S. 1990, Ann. Rev. Astron. Astrophys, 28, 37 33

McKee, C. F. & Tan, J. C. 2002, Nature, 416, 59 1

—. 2003, Astrophys. J, 585, 850 1

Megeath, S. T., Allen, L. E., Gutermuth, R. A., Pipher, J. L., Myers, P. C., Calvet, N., Hartmann, L., Muzerolle, J., & Fazio, G. G. 2004, Astrophys. J., Suppl. Ser, 154, 367 73

Miettinen, O. & Harju, J. 2010, ArXiv e-prints 108

Minier, V., Conway, J. E., & Booth, R. S. 2001, Astron. Astrophys, 369, 278 61

Müller, H. S. P., Schlöder, F., Stutzki, J., & Winnewisser, G. 2005, Journal of Molecular Structure, 742, 215 51

Müller, H. S. P., Thorwirth, S., Roth, D. A., & Winnewisser, G. 2001, Astron. Astrophys, 370, L49 51

Myers, P. C., Mardones, D., Tafalla, M., Williams, J. P., & Wilner, D. J. 1996, Astrophys. J., Lett, 465, L133+ 49

Nomura, H. & Millar, T. J. 2004, Astron. Astrophys, 414, 409 58

Nyman, L.-Å., Lerner, M., Nielbock, M., Anciaux, M., Brooks, K., Chini, R., Albrecht, M., Lemke, R., Kreysa, E., Zylka, R., Johansson, L. E. B., Bronfman, L., Kontinen, S., Linz, H., & Stecklum, B. 2001, The Messenger, 106, 40 8

Oh, C. S., Kobayashi, H., Honma, M., Hirota, T., Sato, K., & Ueno, Y. 2010, Publ. Aston. Soc. Jpn, 62, 101 62, 77

Ohishi, M., Irvine, W. M., & Kaifu, N. 1992, in IAU Symposium, Vol. 150, Astrochemistry of Cosmic Phenomena, ed. P. D. Singh, 171–+ 56, 58

Ormel, C. W., Shipman, R. F., Ossenkopf, V., & Helmich, F. P. 2005, Astron. Astrophys, 439, 613 108

Ossenkopf, V. & Henning, T. 1994, Astron. Astrophys, 291, 943 10, 18, 22

Padovani, M., Walmsley, C. M., Tafalla, M., Galli, D., & Müller, H. S. P. 2009, Astron. Astrophys, 505, 1199 56

Parsons, H., Thompson, M. A., & Chrysostomou, A. 2009, Mon. Not. R. Astron. Soc, 399, 1506 108

Perault, M., Omont, A., Simon, G., Seguin, P., Ojha, D., Blommaert, J., Felli, M., Gilmore, G., Guglielmo, F., Habing, H., Price, S., Robin, A., de Batz, B., Cesarsky, C., Elbaz, D., Epchtein, N., Fouque, P., Guest, S., Levine, D., Pollock, A., Prusti, T., Siebenmorgen, R., Testi, L., & Tiphene, D. 1996, Astron. Astrophys, 315, L165 3

Peretto, N. & Fuller, G. A. 2009, Astron. Astrophys, 505, 405 108

Peretto, N., Fuller, G. A., André, P., & Hennebelle, P. 2008, in Astronomical Society of the Pacific Conference Series, Vol. 387, Astronomical Society of the Pacific Conference Series, ed. H. Beuther, H. Linz, & T. Henning, 50–+ 17

Peters, T., Klessen, R. S., Mac Low, M., & Banerjee, R. 2010, ArXiv e-prints 2

Pilbratt, G. L., Riedinger, J. R., Passvogel, T., Crone, G., Doyle, D., Gageur, U., Heras, A. M., Jewell, C., Metcalfe, L., Ott, S., & Schmidt, M. 2010, Astron. Astrophys, 518, L1+ 88

Pillai, T., Wyrowski, F., Carey, S. J., & Menten, K. M. 2006a, Astron. Astrophys, 450, 569 3, 35, 48, 56

—. 2006b, Astron. Astrophys, 450, 569 108

Pillai, T., Wyrowski, F., Menten, K. M., & Krügel, E. 2006c, Astron. Astrophys, 447, 929 10

Pirogov, L., Zinchenko, I., Caselli, P., Johansson, L. E. B., & Myers, P. C. 2003, Astron. Astrophys, 405, 639 37, 48, 49, 58

Poglitsch, A., Waelkens, C., Geis, N., Feuchtgruber, H., Vandenbussche, B., Rodriguez, L., Krause, O., Renotte, E., van Hoof, C., Saraceno, P., Cepa, J., Kerschbaum, F., Agnèse, P., Ali, B., Altieri, B., Andreani, P., Augueres, J., Balog, Z., Barl, L., Bauer, O. H., Belbachir, N., Benedettini, M., Billot, N., Boulade, O., Bischof, H., Blommaert, J., Callut, E., Cara, C., Cerulli, R., Cesarsky, D., Contursi, A., Creten, Y., De Meester, W., Doublier, V., Doumayrou, E., Duband, L., Exter, K., Genzel, R., Gillis, J., Grözinger, U., Henning, T., Herreros, J., Huygen, R., Inguscio, M., Jakob, G., Jamar, C., Jean, C., de Jong, J., Katterloher, R., Kiss, C., Klaas, U., Lemke, D., Lutz, D., Madden, S., Marquet, B., Martignac, J., Mazy, A., Merken, P., Montfort, F., Morbidelli, L., Müller, T., Nielbock, M., Okumura, K., Orfei, R., Ottensamer, R., Pezzuto, S., Popesso, P., Putzeys, J., Regibo, S., Reveret, V., Royer, P., Sauvage, M., Schreiber, J., Stegmaier, J., Schmitt, D., Schubert, J., Sturm, E., Thiel, M., Tofani, G., Vavrek, R., Wetzstein, M., Wieprecht, E., & Wiezorrek, E. 2010, Astron. Astrophys, 518, L2+ 89

Purcell, C. R., Balasubramanyam, R., Burton, M. G., Walsh, A. J., Minier, V., Hunt-Cunningham, M. R., Kedziora-Chudczer, L. L., Longmore, S. N., Hill, T., Bains, I., Barnes, P. J., Busfield, A. L., Calisse, P., Crighton, N. H. M., Curran, S. J., Davis, T. M., Dempsey, J. T., Derragopian, G., Fulton, B., Hidas, M. G., Hoare, M. G., Lee, J., Ladd, E. F., Lumsden, S. L., Moore, T. J. T., Murphy, M. T., Oudmaijer, R. D., Pracy, M. B., Rathborne, J., Robertson, S., Schultz, A. S. B., Shobbrook, J., Sparks, P. A., Storey, J., & Travouillion, T. 2006, Mon. Not. R. Astron. Soc, 367, 553 37, 49, 51

Ragan, S. E., Bergin, E. A., & Gutermuth, R. A. 2009, Astrophys. J, 698, 324 2, 3, 108

Ragan, S. E., Bergin, E. A., Plume, R., Gibson, D. L., Wilner, D. J., O'Brien, S., & Hails, E. 2006, Astrophys. J., Suppl. Ser, 166, 567 37, 43, 48, 108

Rathborne, J. M., Jackson, J. M., & Simon, R. 2006, Astrophys. J, 641, 389 viii, 2, 3, 27, 28, 31, 108

Rathborne, J. M., Jackson, J. M., Zhang, Q., & Simon, R. 2008, Astrophys. J, 689, 1141 28, 108

Rathborne, J. M., Simon, R., & Jackson, J. M. 2007, Astrophys. J, 662, 1082 108

Rawlings, J. M. C., Redman, M. P., Keto, E., & Williams, D. A. 2004, Mon. Not. R. Astron. Soc, 351, 1054 38

Rawlings, J. M. C., Taylor, S. D., & Williams, D. A. 2000, Mon. Not. R. Astron. Soc, 313, 461 38

Rayner, J. T., Cushing, M. C., & Vacca, W. D. 2009, Astrophys. J., Suppl. Ser, 185, 289 76

Redman, M. P., Khanzadyan, T., Loughnane, R. M., & Carolan, P. B. 2008, in Astronomical Society of the Pacific Conference Series, Vol. 387, Massive Star Formation: Observations Confront Theory, ed. H. Beuther, H. Linz, & T. Henning, 38–+ 38

Rochau, B., Brandner, W., Stolte, A., Gennaro, M., Gouliermis, D., Da Rio, N., Dzyurkevich, N., & Henning, T. 2010, Astrophys. J., Lett, 716, L90 90

Saito, H., Mizuno, N., Moriguchi, Y., Matsunaga, K., Onishi, T., Mizuno, A., & Fukui, Y. 2001, Publ. Aston. Soc. Jpn, 53, 1037 9, 41

Sakai, T., Sakai, N., Kamegai, K., Hirota, T., Yamaguchi, N., Shiba, S., & Yamamoto, S. 2008, Astrophys. J, 678, 1049 3, 35, 56

Sarrasin, E., Abdallah, D. B., Wernli, M., Faure, A., Cernicharo, J., & Lique, F. 2010, Mon. Not. R. Astron. Soc, 404, 518 38, 52, 59

Schilke, P., Walmsley, C. M., Pineau Des Forets, G., Roueff, E., Flower, D. R., & Guilloteau, S. 1992, Astron. Astrophys, 256, 595 38, 52, 59

Schreiber, J., Thatte, N., Eisenhauer, F., Tecza, M., Abuter, R., & Horrobin, M. 2004, in Astronomical Society of the Pacific Conference Series, Vol. 314, Astronomical Data Analysis Software and Systems (ADASS) XIII, ed. F. Ochsenbein, M. G. Allen, & D. Egret, 380–+ 63

Shirley, Y. L., Evans, II, N. J., Young, K. E., Knez, C., & Jaffe, D. T. 2003, Astrophys. J., Suppl. Ser, 149, 375 48

Siegel, S. & Castellan, N. J. 1988, Nonparametric Statistics for the Behavioural Sciences (McGraw-Hill) 27

Simon, R., Jackson, J. M., Rathborne, J. M., & Chambers, E. T. 2006a, Astrophys. J, 639, 227 18, 108

Simon, R., Rathborne, J. M., Shah, R. Y., Jackson, J. M., & Chambers, E. T. 2006b, Astrophys. J, 653, 1325 3

Smith, R. J., Glover, S. C. O., Bonnell, I. A., Clark, P. C., & Klessen, R. S. 2010, ArXiv e-prints 2

Snell, R. L., Huang, Y., Dickman, R. L., & Claussen, M. J. 1988, Astrophys. J, 325, 853 61, 62, 82

Sridharan, T. K., Beuther, H., Saito, M., Wyrowski, F., & Schilke, P. 2005, Astrophys. J., Lett, 634, L57 viii, 3, 20, 27, 31

Sridharan, T. K., Beuther, H., Schilke, P., Menten, K. M., & Wyrowski, F. 2002, Astrophys. J, 566, 931 2, 58

Steinacker, J., Bacmann, A., Henning, T., Klessen, R., & Stickel, M. 2005, Astron. Astrophys, 434, 167 26

Szymczak, M., Hrynek, G., & Kus, A. J. 2000, Astron. Astrophys. Suppl. Ser, 143, 269 61

Tafalla, M., Myers, P. C., Caselli, P., Walmsley, C. M., & Comito, C. 2002, Astrophys. J, 569, 815 37

Tafalla, M., Santiago-García, J., Myers, P. C., Caselli, P., Walmsley, C. M., & Crapsi, A. 2006, Astron. Astrophys, 455, 577 56, 58

Tamura, M., Gatley, I., Joyce, R. R., Ueno, M., Suto, H., & Sekiguchi, M. 1991, Astrophys. J, 378, 611 61, 65, 82

Turner, J., Kirby-Docken, K., & Dalgarno, A. 1977, Astrophys. J., Suppl. Ser, 35, 281 69

Vasyunina, T., Linz, H., Henning, T., Stecklum, B., Klose, S., & Nyman, L.-Å. 2009, Astron. Astrophys, 499, 149 36, 41, 51

Viti, S. 2005, in IAU Symposium, Vol. 231, Astrochemistry: Recent Successes and Current Challenges, ed. D. C. Lis, G. A. Blake, & E. Herbst, 67–76 37

Wall, J. V. & Jenkins, C. R. 2003, Practical Statistics for Astronomers (Princeton Series in Astrophysics) 26

Walsh, A. J. & Burton, M. G. 2006, Mon. Not. R. Astron. Soc, 365, 321 37

Weferling, B., Reichertz, L. A., Schmid-Burgk, J., & Kreysa, E. 2002, Astron. Astrophys, 383, 1088 8

Weingartner, J. C. & Draine, B. T. 2001, Astrophys. J, 548, 296 17, 18, 26, 27, 33

Werner, M. W., Roellig, T. L., Low, F. J., Rieke, G. H., Rieke, M., Hoffmann, W. F., Young, E., Houck, J. R., Brandl, B., Fazio, G. G., Hora, J. L., Gehrz, R. D., Helou, G., Soifer, B. T., Stauffer, J., Keene, J., Eisenhardt, P., Gallagher, D., Gautier,

T. N., Irace, W., Lawrence, C. R., Simmons, L., Van Cleve, J. E., Jura, M., Wright, E. L., & Cruikshank, D. P. 2004, Astrophys. J., Suppl. Ser, 154, 1 63

Zhang, Q., Ho, P. T. P., & Ohashi, N. 1998, Astrophys. J, 494, 636 69

Zhang, Q., Sridharan, T. K., Hunter, T. R., Chen, Y., Beuther, H., & Wyrowski, F. 2007, Astron. Astrophys, 470, 269 38

Zhang, Q., Wang, Y., Pillai, T., & Rathborne, J. 2009, Astrophys. J, 696, 268 89

Zinchenko, I., Caselli, P., & Pirogov, L. 2009, Mon. Not. R. Astron. Soc, 395, 2234 58

Zinchenko, I., Henkel, C., & Mao, R. Q. 2000, Astron. Astrophys, 361, 1079 38, 58

Zinnecker, H. & Yorke, H. W. 2007, Ann. Rev. Astron. Astrophys, 45, 481 1

Appendix A

Chronology of IRDCs

A. CHRONOLOGY OF IRDCS

Table A.1. Chronology of IRDCs.

Authors, year	What was done
(Carey et al., 1998)	H_2CO observations. First probing of the physical properties of dark clouds.
(Carey et al., 2000)	Submillimeter continuum mapping. Mass and column density estimations.
(Johnstone et al., 2003)	Investigation of the dust properties in IRDC 11.11-0.12. Extracted column density profile.
(Ormel et al., 2005)	The modeling of IRDCs of the sum-mm dust continuum and HCO^+ line data.
(Pillai et al., 2006b)	Ammonia Observations.
(Ragan et al., 2006)	Molecular line observations.
(Rathborne et al., 2006)	Millimeter continuum mapping. Masses estimation.
(Simon et al., 2006a)	Produced a catalog of 11 000 IRDCs.
(Frieswijk et al., 2007)	Molecular line observations of the Outer Galaxy IRDC candidate G111.80+0.58.
(Rathborne et al., 2007)	Detected bright, compact high- and low-mass condensations toward IRDC cores.
(Du & Yang, 2008)	CO isotops survey.
(Jackson et al., 2008)	CS observations. Investigation of the galactic distribution of IRDCs.
(Frieswijk et al., 2008)	Spitzer observations of the Outer Galaxy IRDC candidate G111.80+0.58.
(Rathborne et al., 2008)	Submillimeter array observations. Found the possible existence of two high-mass star-forming cores.
(Butler & Tan, 2009)	Mid-IR extinction mapping.
(Chambers et al., 2009)	Classification of 190 IRDCs based upon their IR characteristics. Producing a list of high-mass starless cores candidates.
(Lee et al., 2009)	Molecular lines probing in IRDCs in the Small Magellanic Cloud.
(Ragan et al., 2009)	Characterization of the environment and nature of IRDCs with SPITZER.
(Peretto & Fuller, 2009)	A catalog of Spitzer dark clouds. New clouds detection.
(Gibson et al., 2009)	Explored properties of the molecular gas. Extended the range of IRDCs from very massive, to clouds which are similar to local counterparts.
(Marshall et al., 2009)	Distribution of the IRDCs based on 2MASS data.
(Parsons et al., 2009)	Investigation of the IRDCs from the SCUBA catalog. Estimated column densities based on 8 and 850 micron data.
(Miettinen & Harju, 2010)	Determination of the physical properties and spatial distribution of dense clumps in the IRDC MSXDC G304.74+01.32.
(Chen et al., 2010)	The first probe of the deuterium fractionation in IRDC 28.34+0.06. The $N(N_2D^+)/N(N_2H^+)$ ratio decreases over a factor of 3 for more evolved regions.
(Jimenez-Serra et al., 2010)	High sensitivity molecular lines mapping toward IRDC G035.39-00.33
(Jackson et al., 2010)	Study of a filamentary IRDC - "Nessie" Nebula
(Battersby et al., 2010)	Complex study of the 8 IRDCs, including mass estimation and investigation of the IRDCs molecular gas properties. Identification of the UC HII regions within IRDCs clumps.

Appendix B

3-color Spitzer/Glimpse images.

B. 3-COLOR SPITZER/GLIMPSE IMAGES.

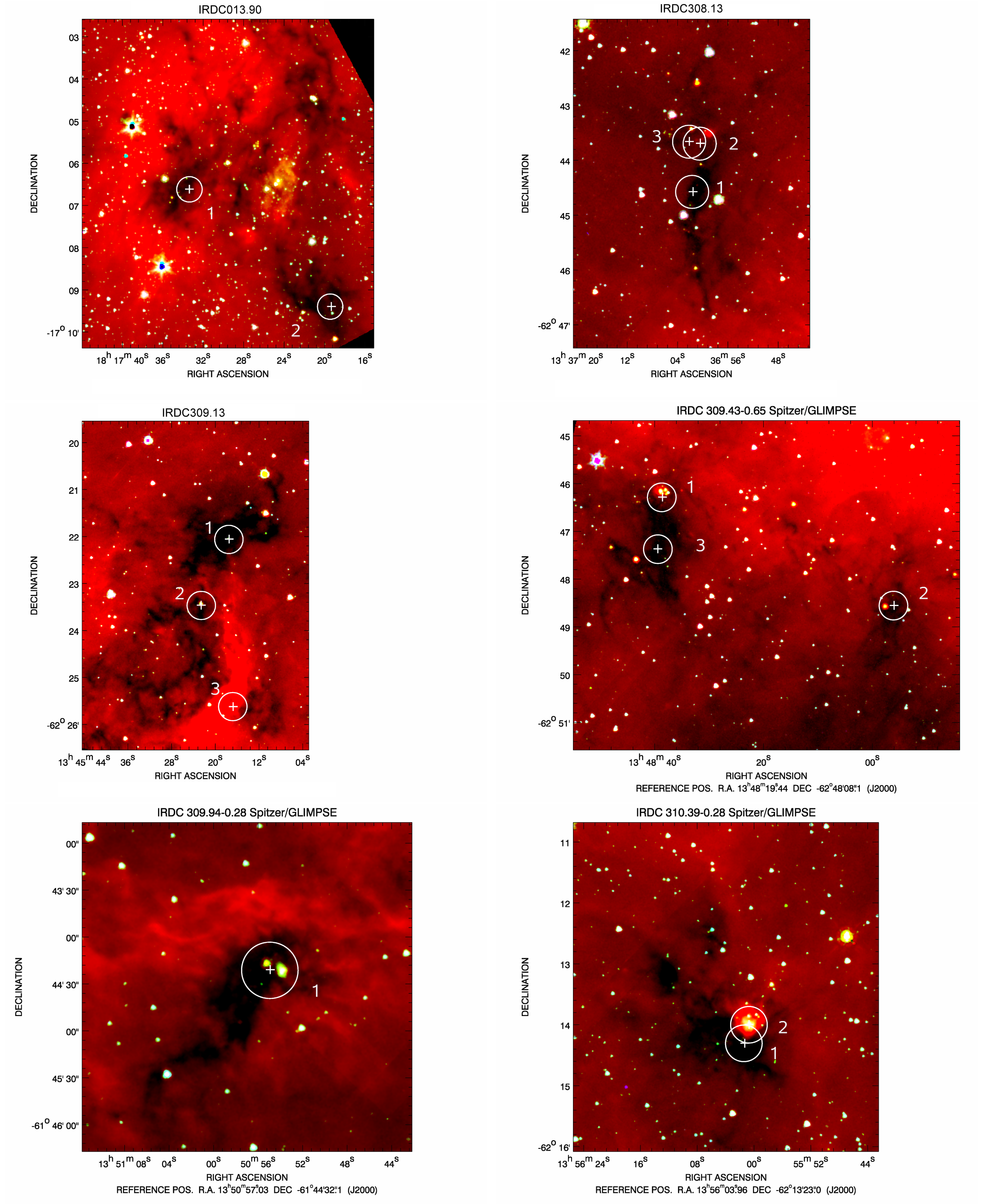

Figure B.1 3-color Spitzer/GLIMPSE image of the Infrared Dark Cloud, where 3.6 μm is blue, 4.5μm is green and 8μm is red. Circles mark observed positions and show the beam size.

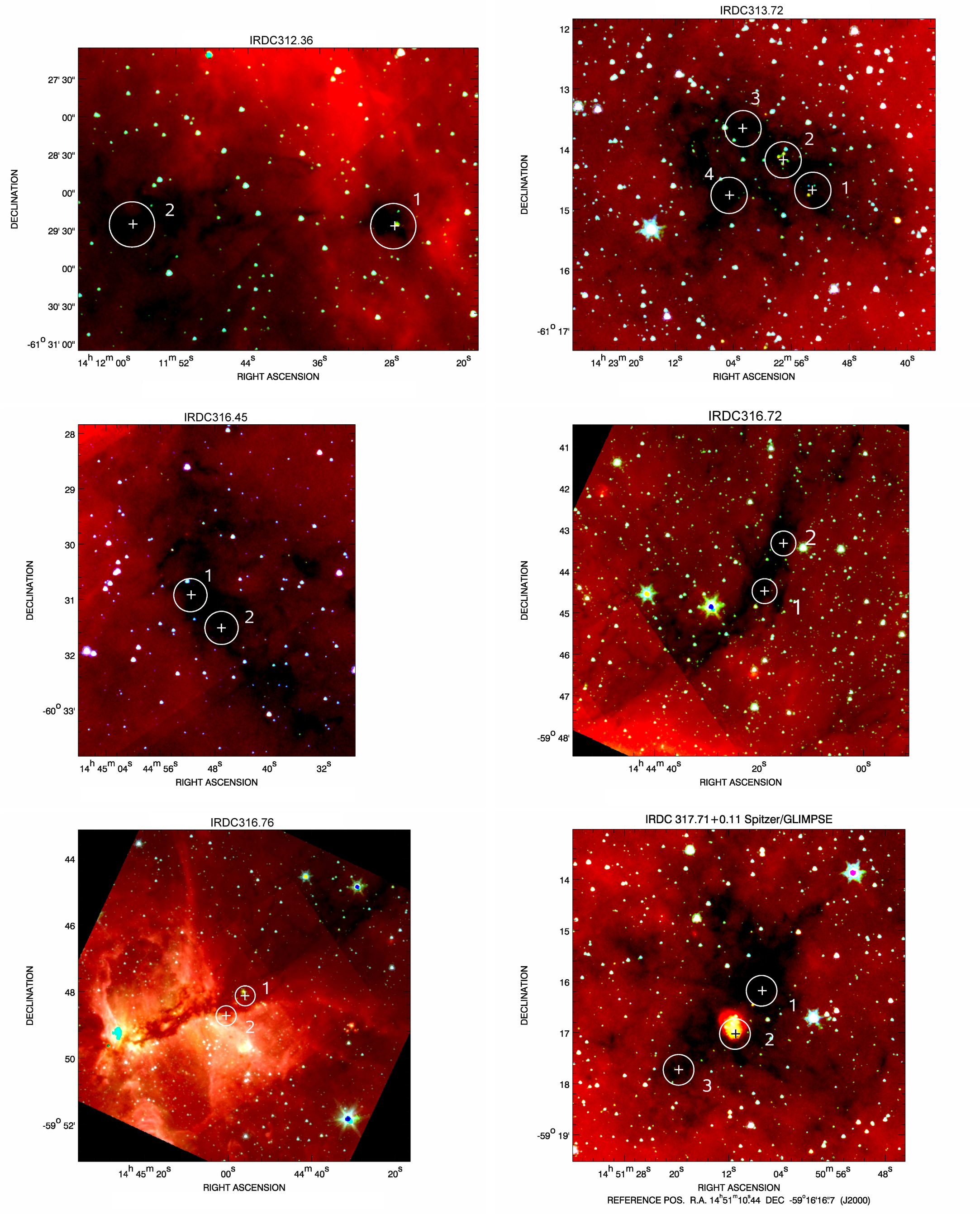

Figure B.2 3-color Spitzer/GLIMPSE image of the Infrared Dark Cloud, where 3.6 μm is blue, 4.5μm is green and 8μm is red. Circles mark observed positions and show the beam size.

B. 3-COLOR SPITZER/GLIMPSE IMAGES.

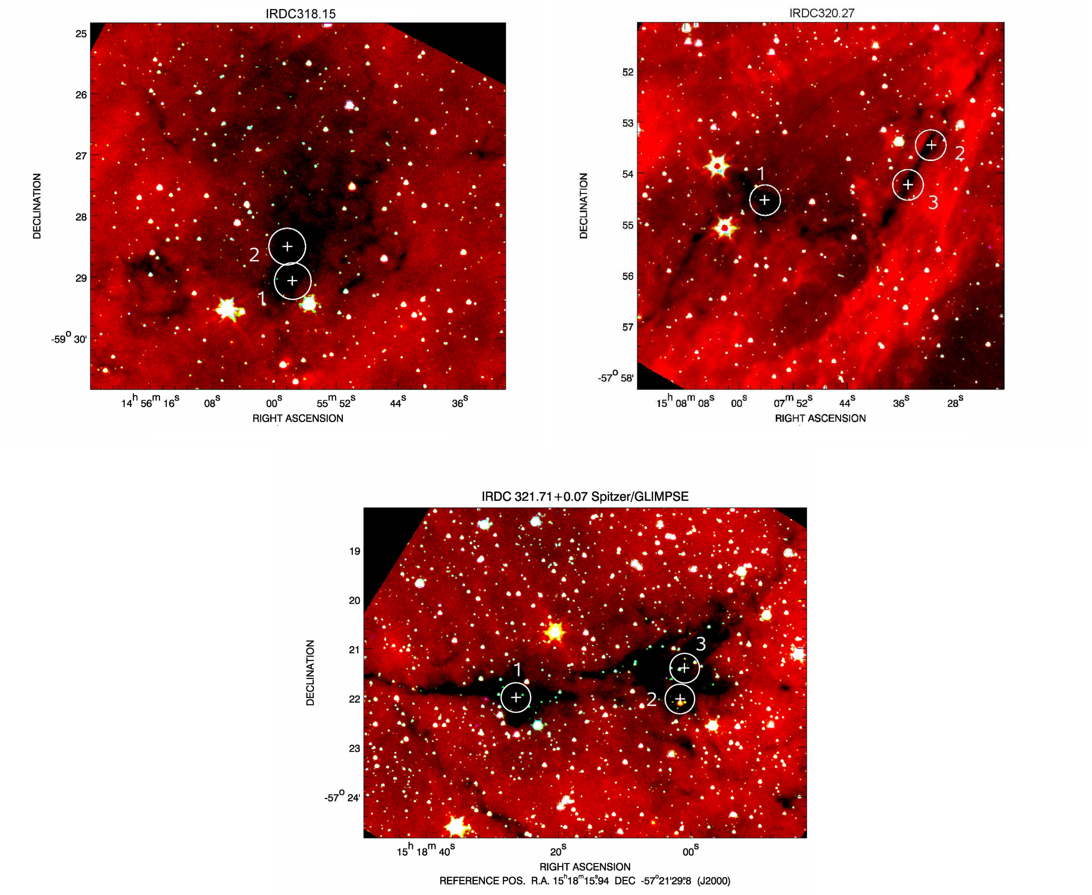

Figure B.3 3-color Spitzer/GLIMPSE image of the Infrared Dark Cloud, where 3.6 μm is blue, 4.5μm is green and 8μm is red. Circles mark observed positions and show the beam size.

Appendix C

Spectra images.

...

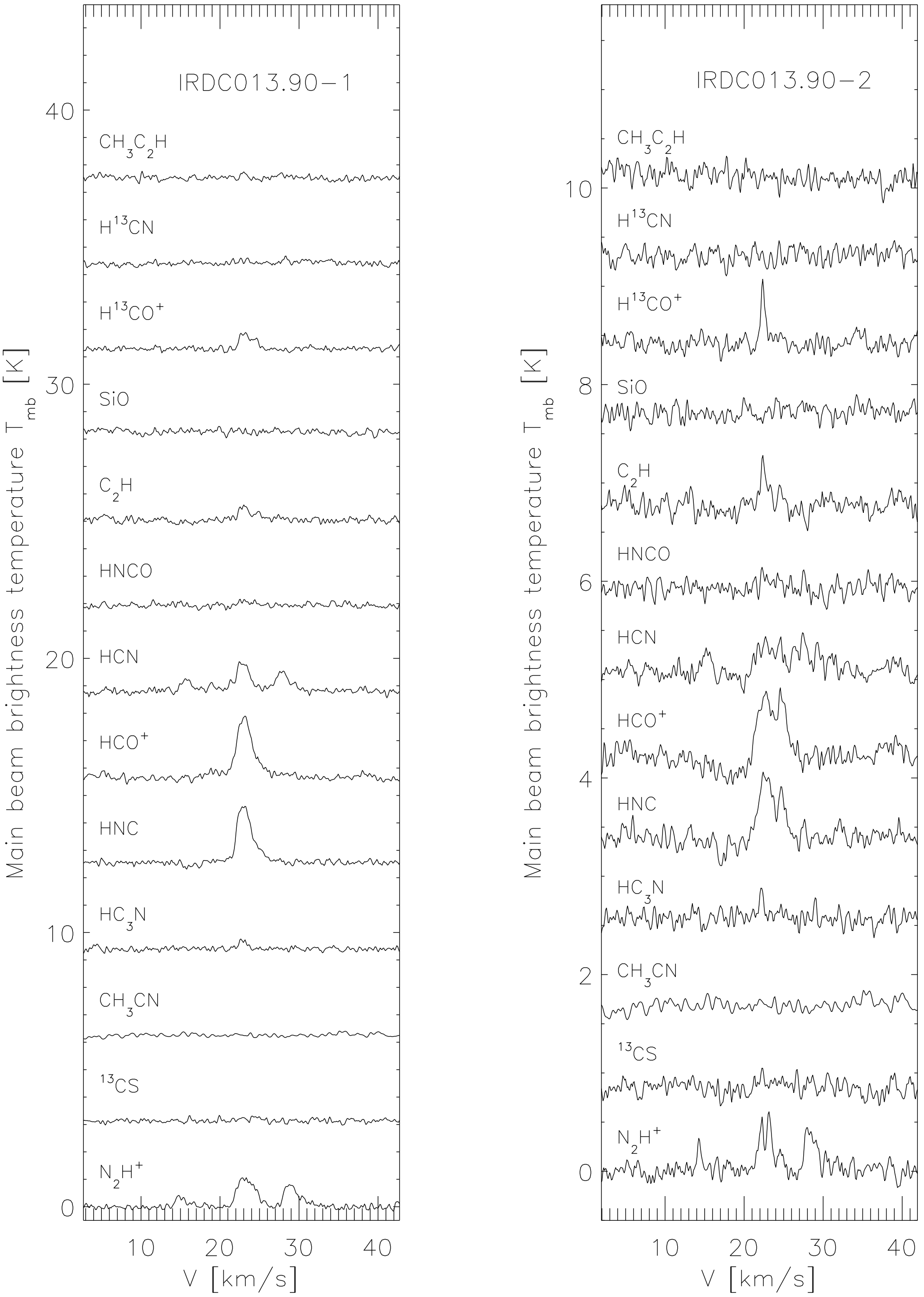

Figure C.1 Observed lines

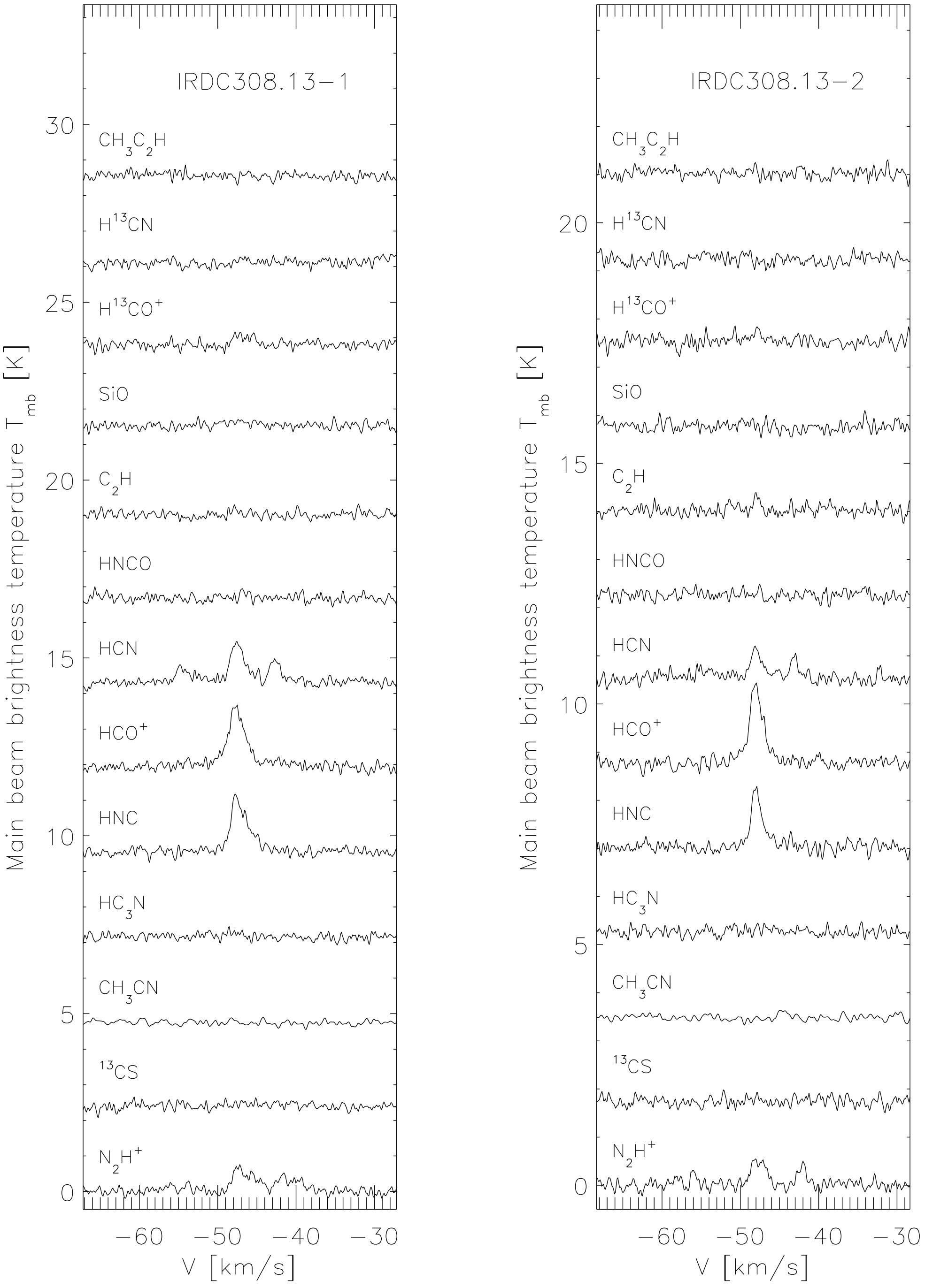

Figure C.2 Observed lines

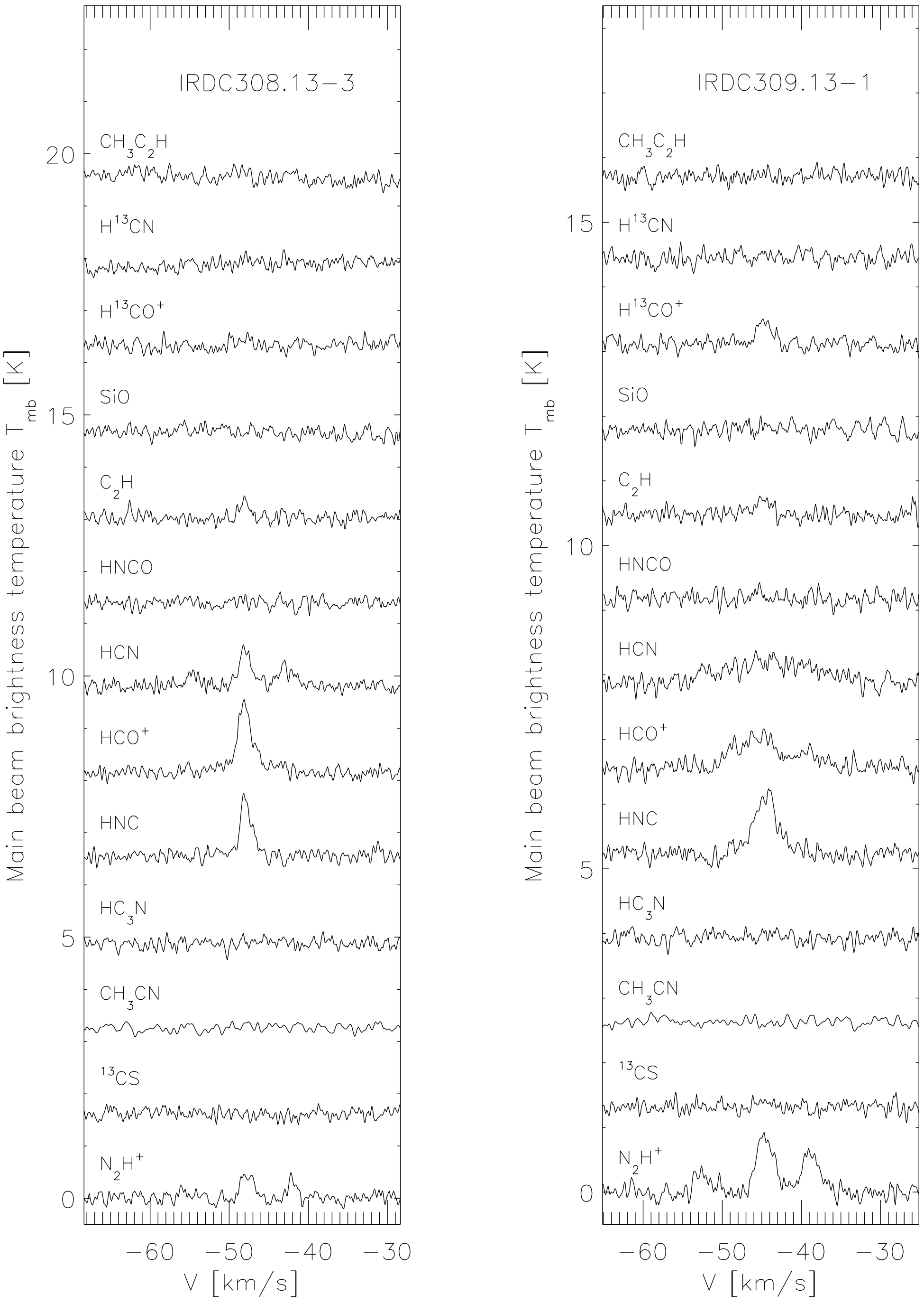

Figure C.3 Observed lines

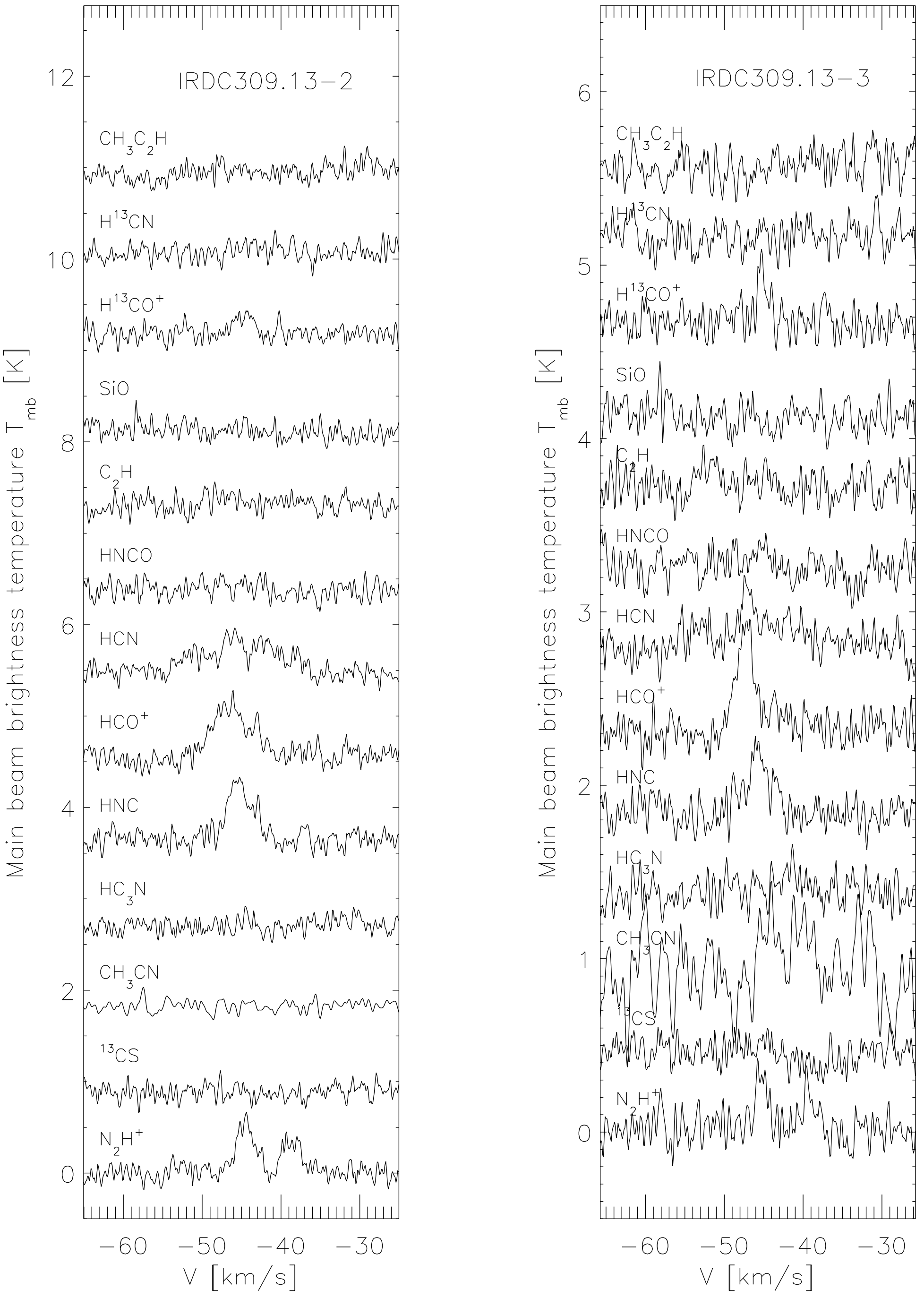

Figure C.4 Observed lines

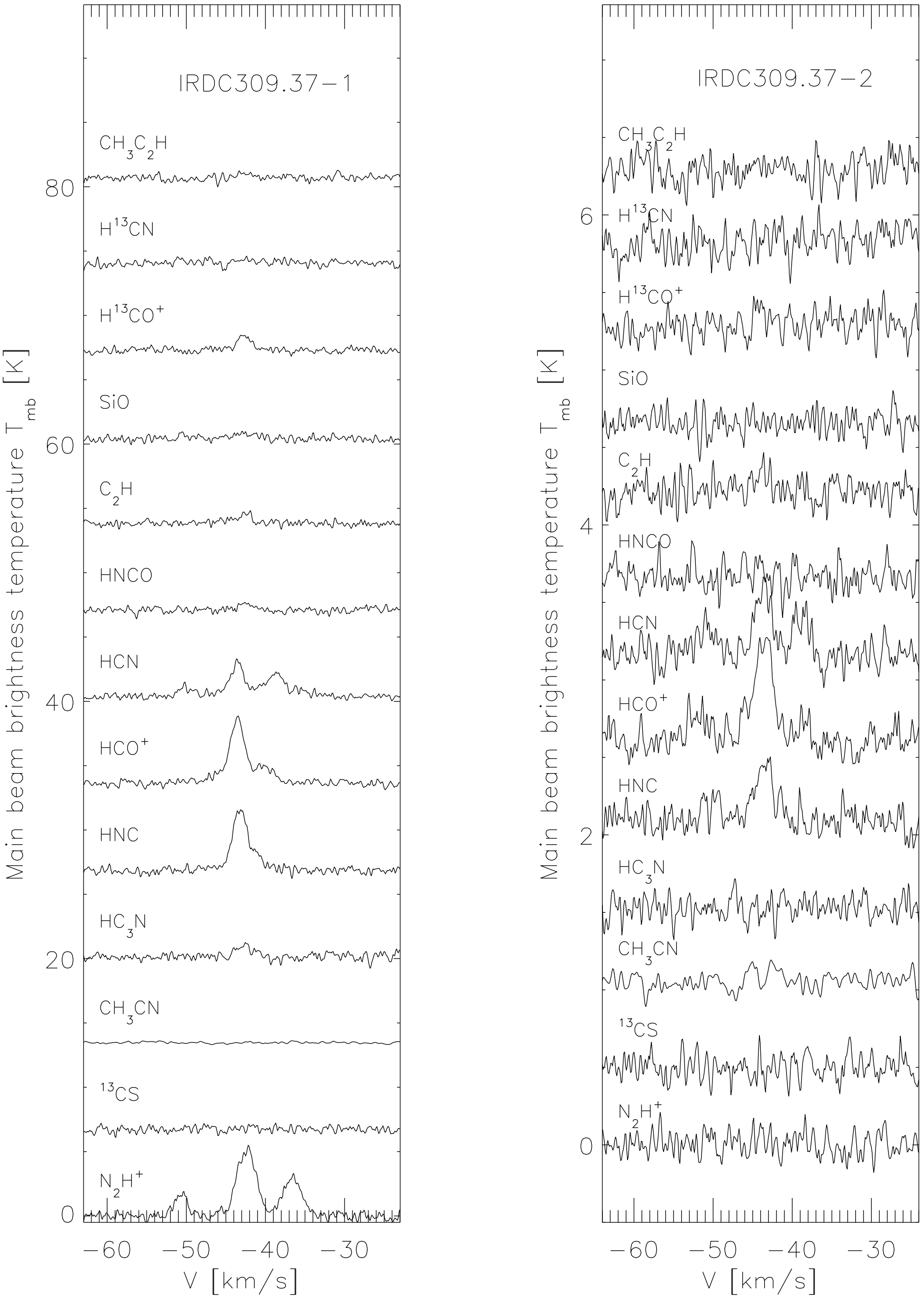

Figure C.5 Observed lines

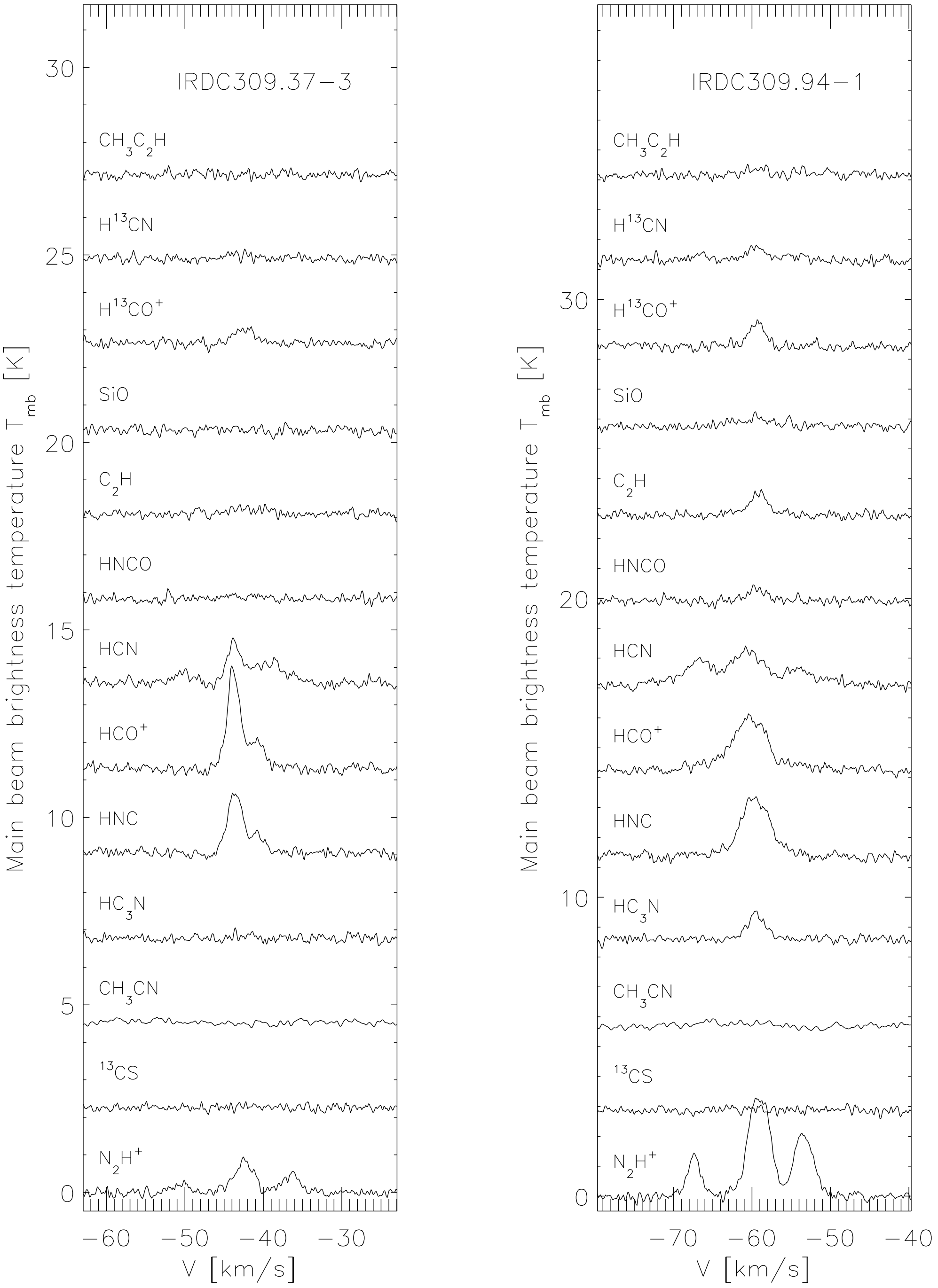

Figure C.6 Observed lines

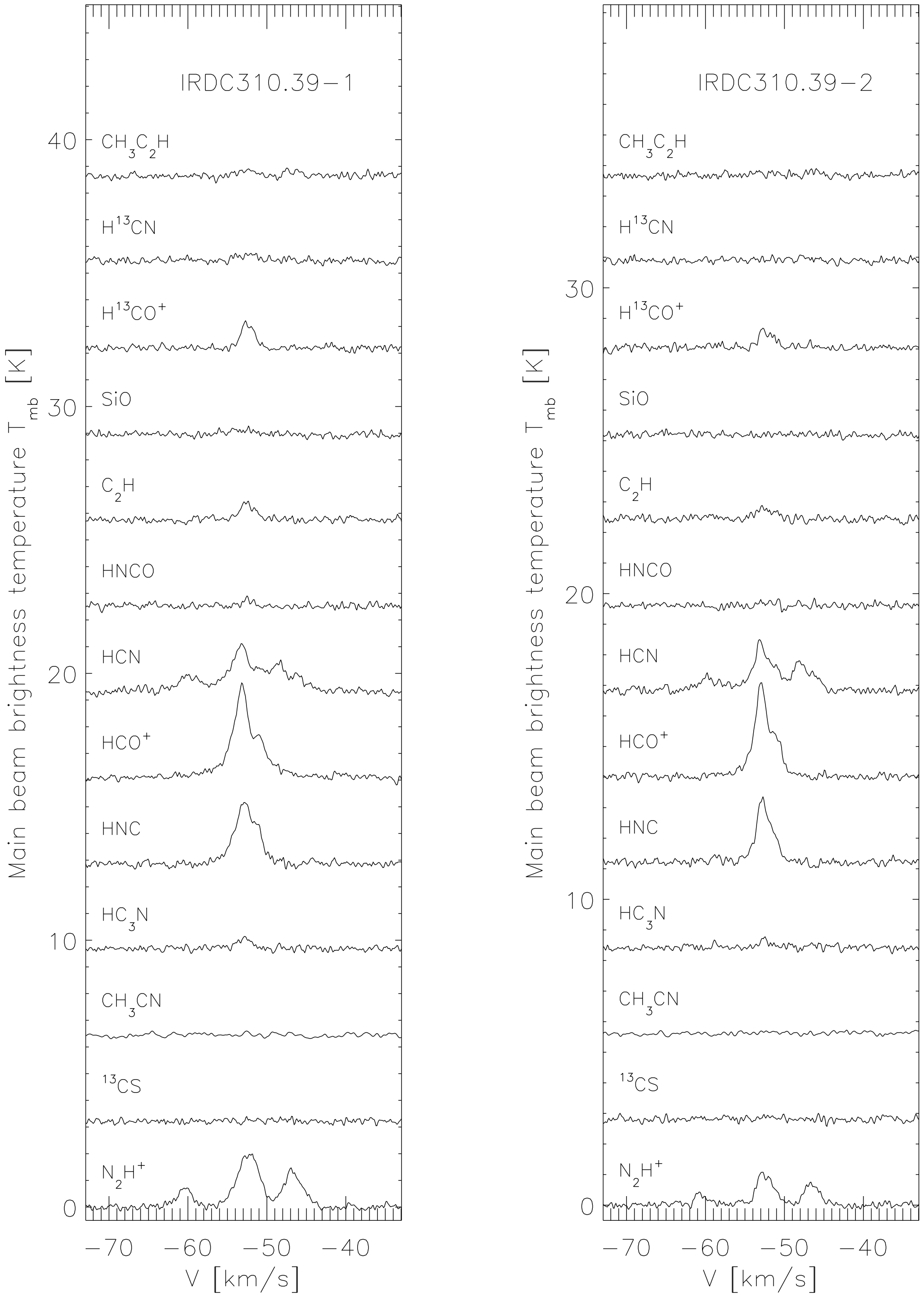

Figure C.7 Observed lines

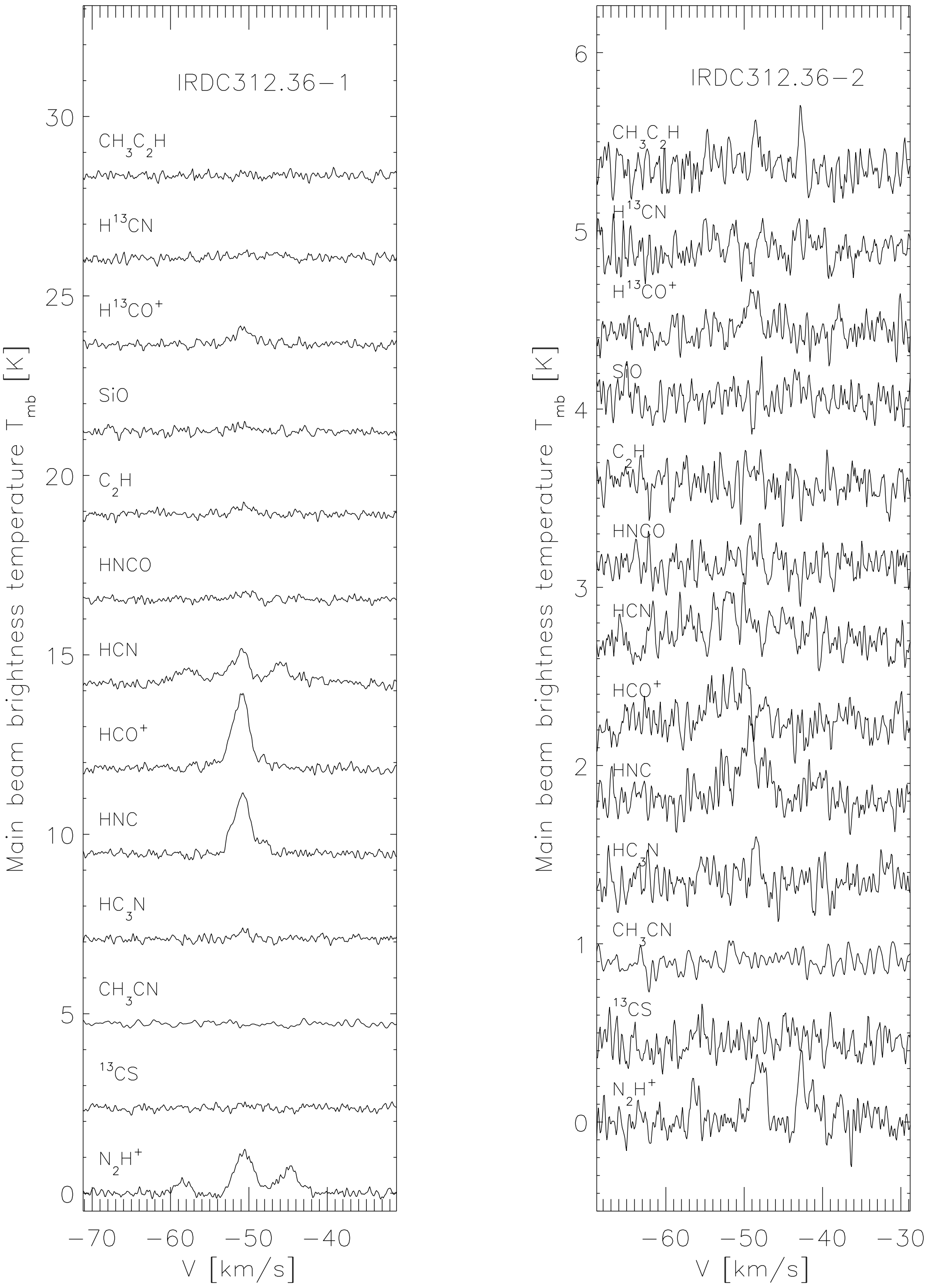

Figure C.8 Observed lines

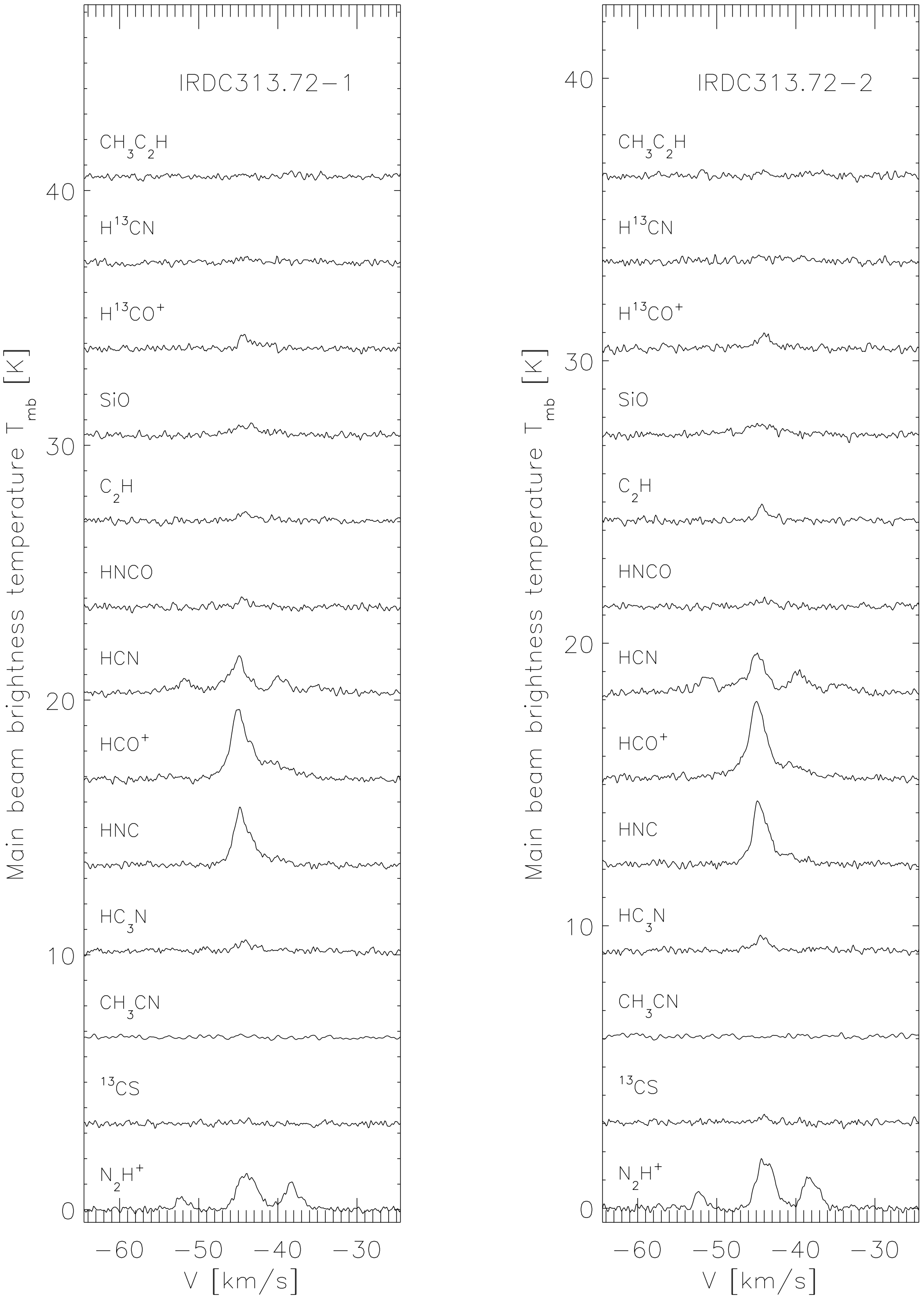

Figure C.9 Observed lines

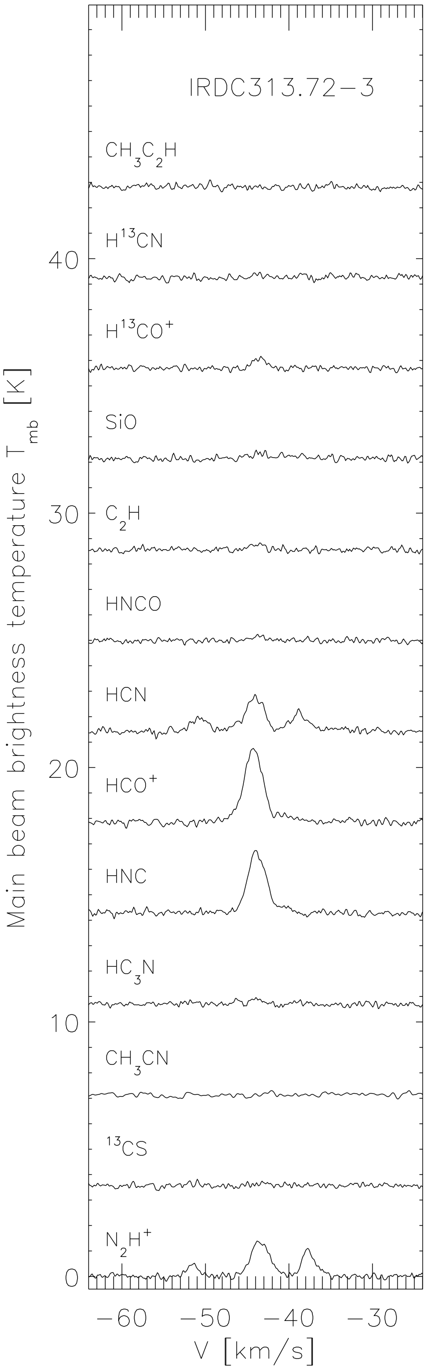

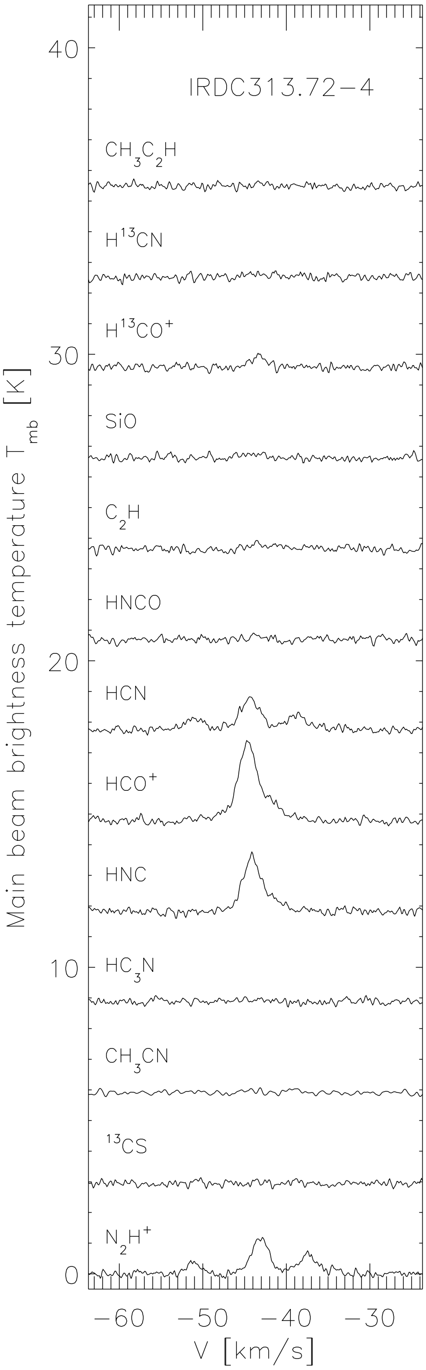

Figure C.10 Observed lines

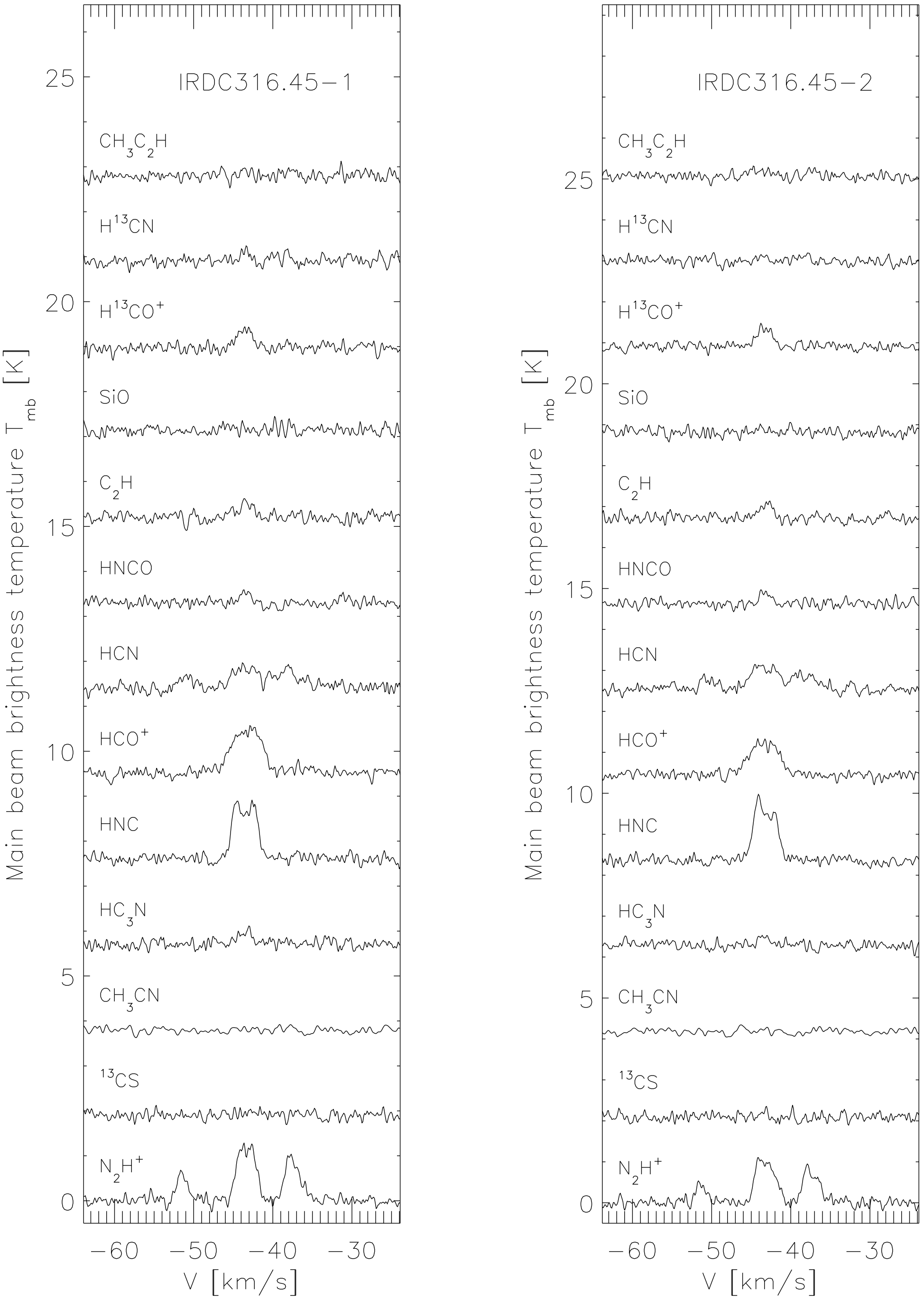

Figure C.11 Observed lines

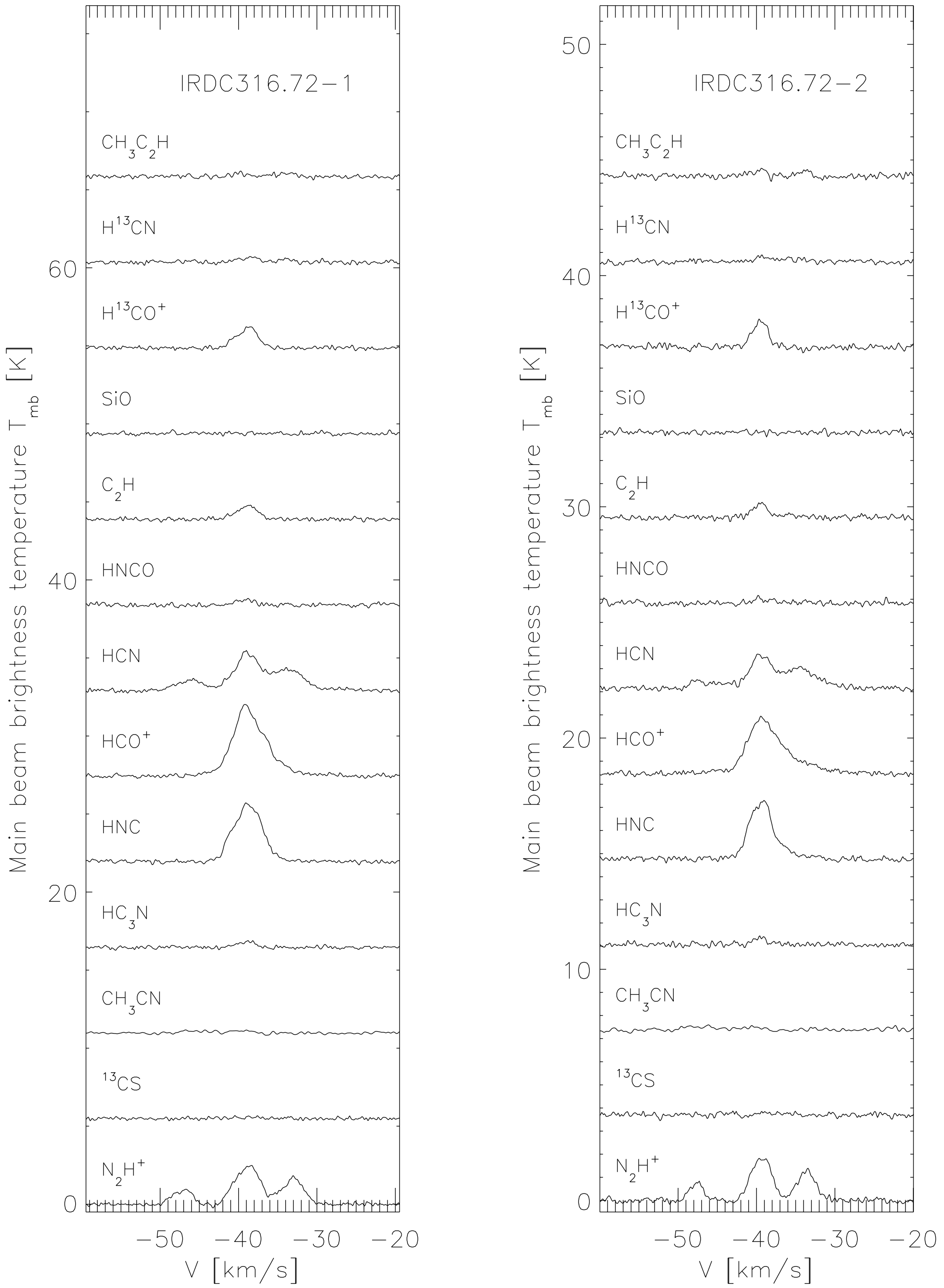

Figure C.12 Observed lines

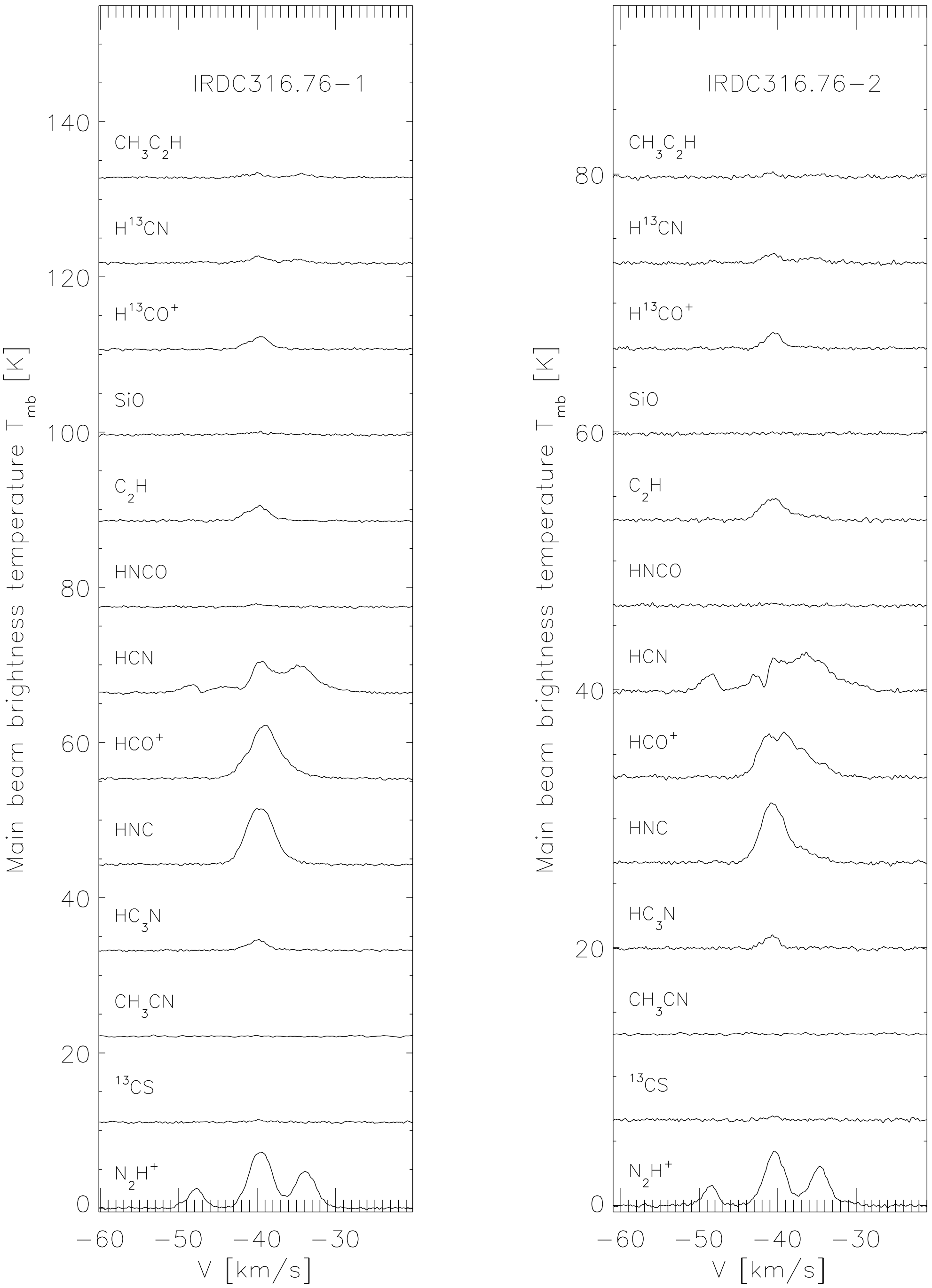

Figure C.13 Observed lines

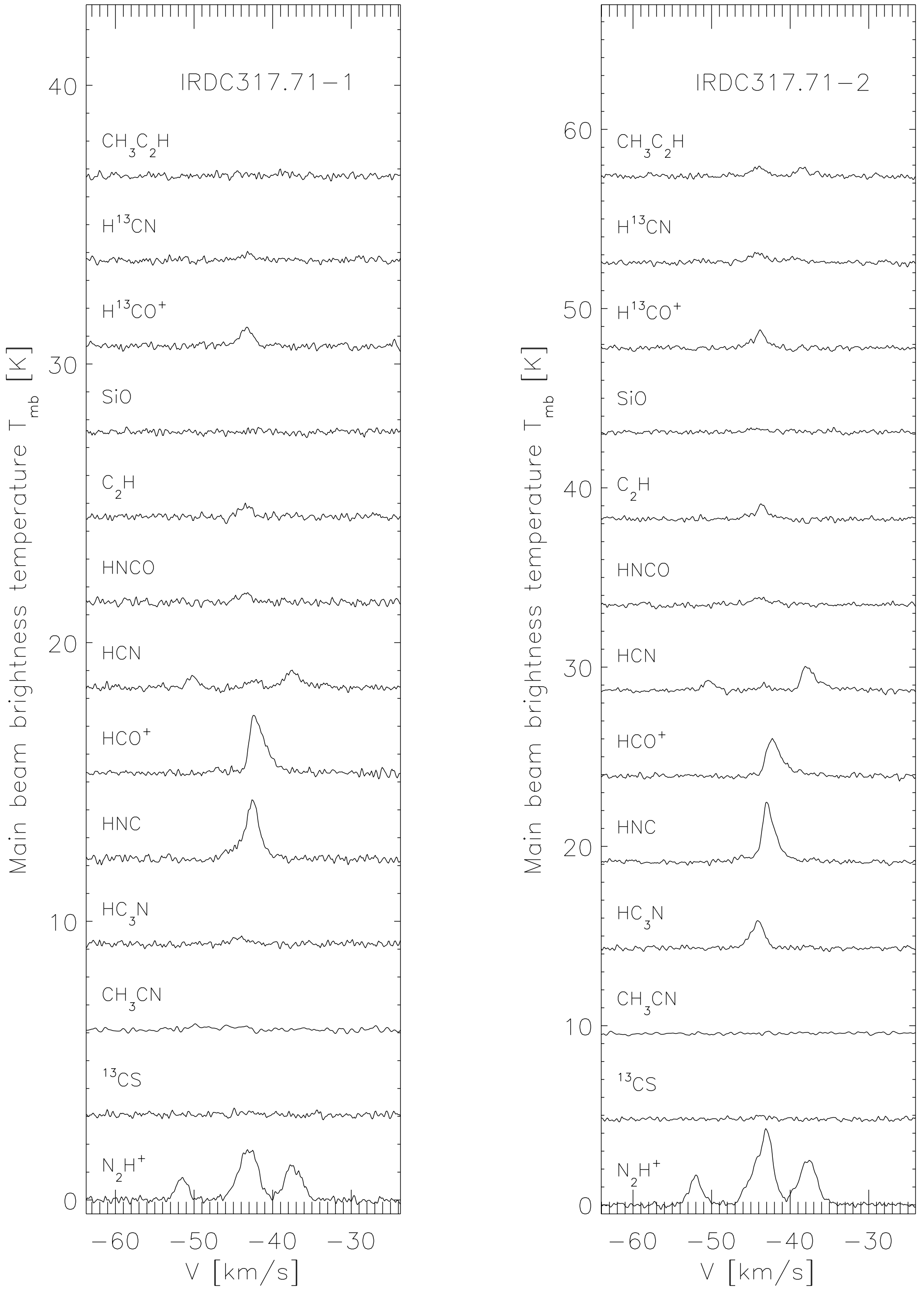

Figure C.14 Observed lines

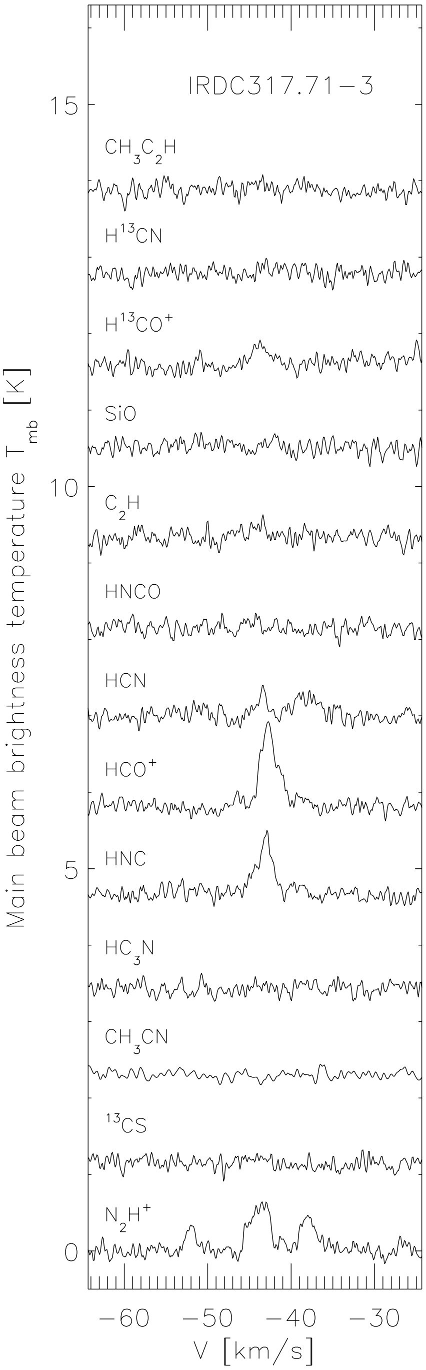

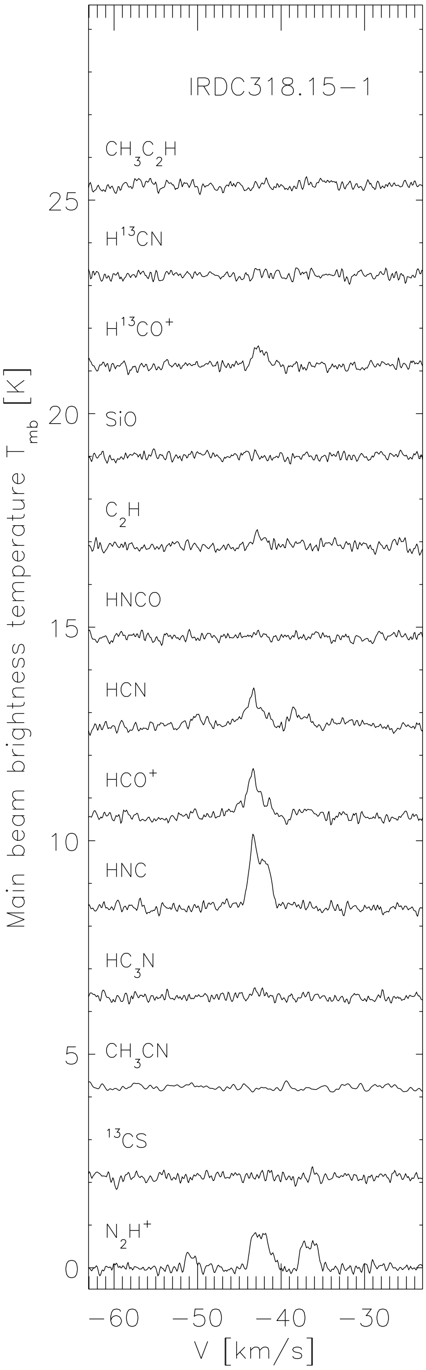

Figure C.15 Observed lines

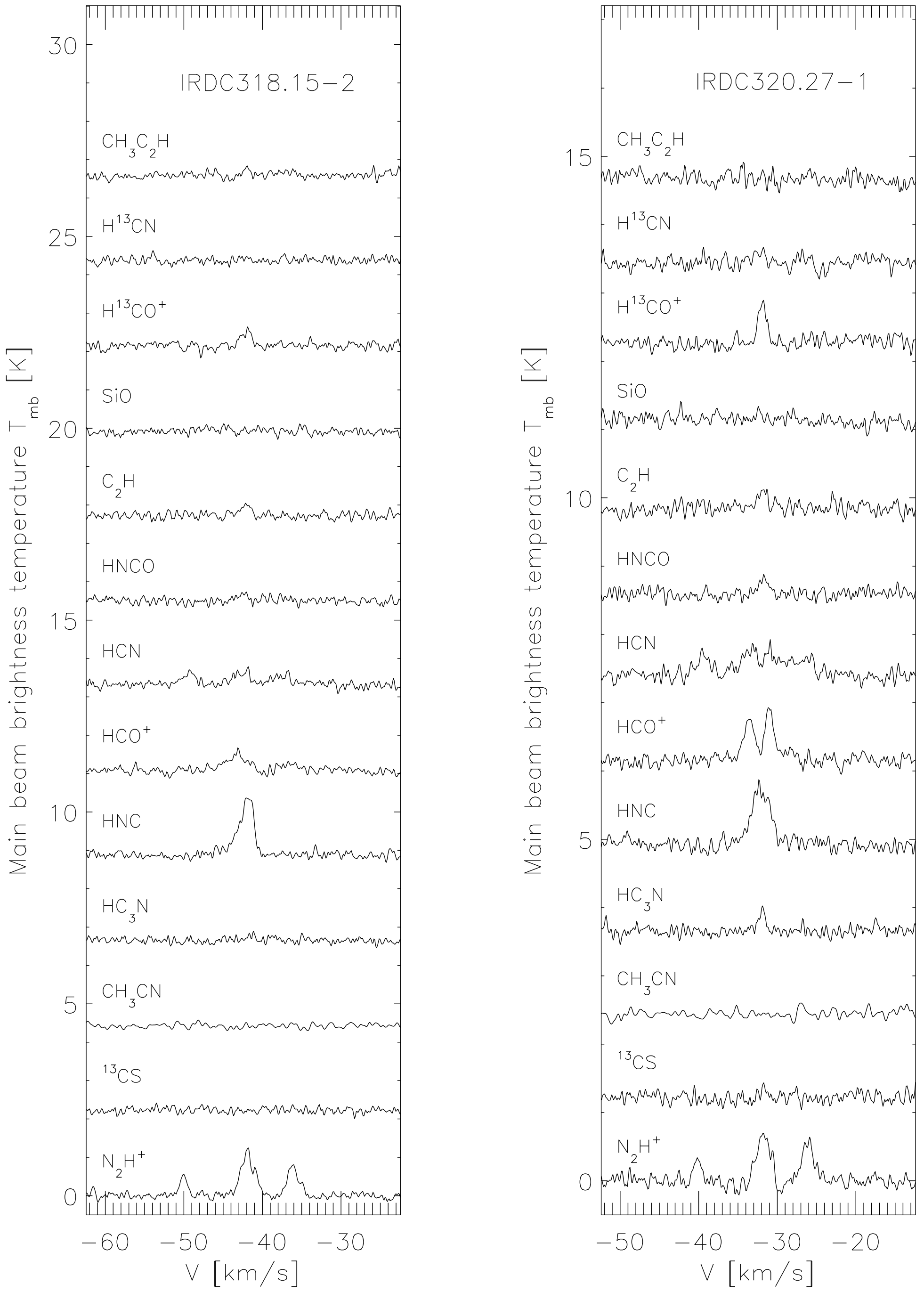

Figure C.16 Observed lines

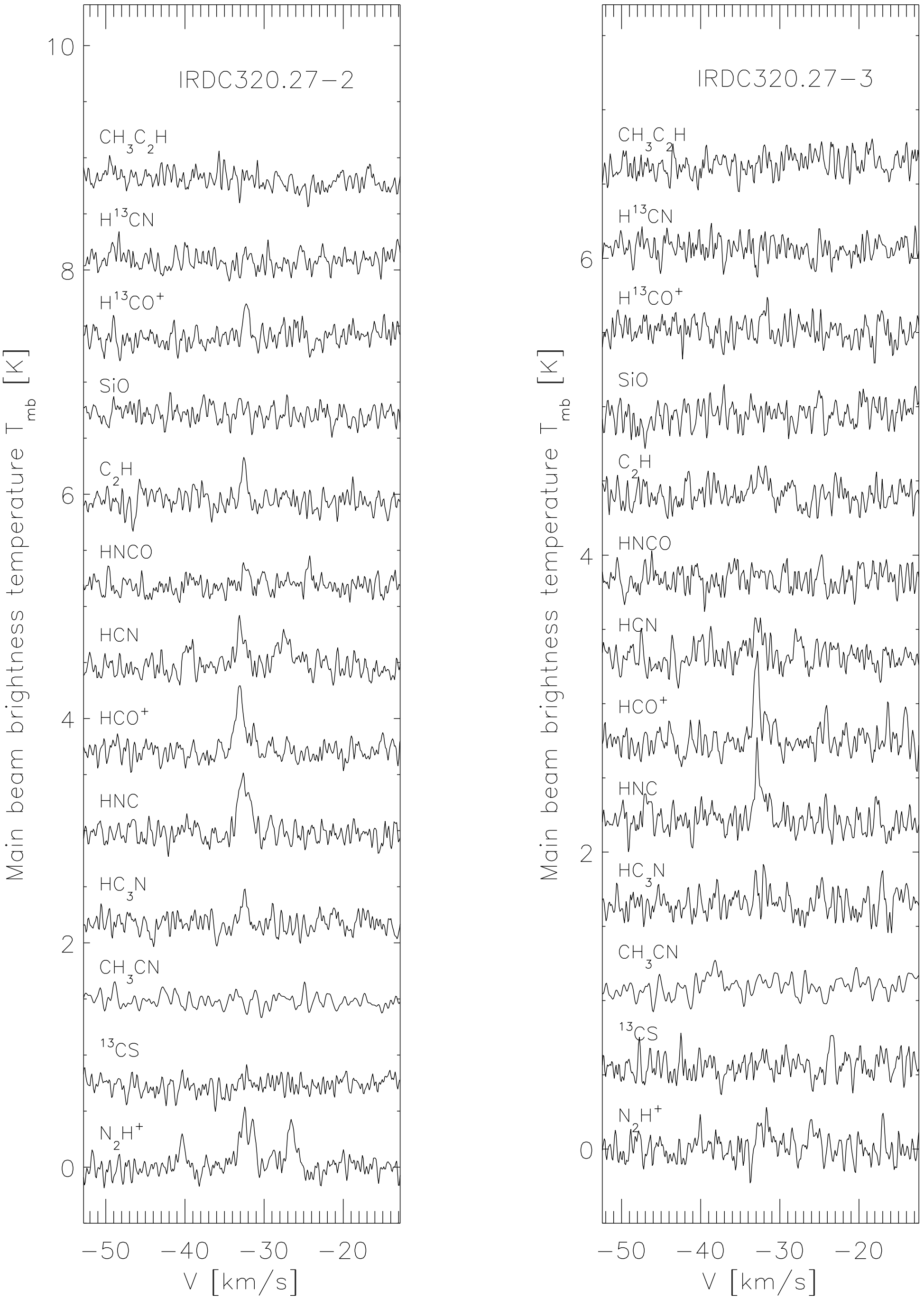

Figure C.17 Observed lines

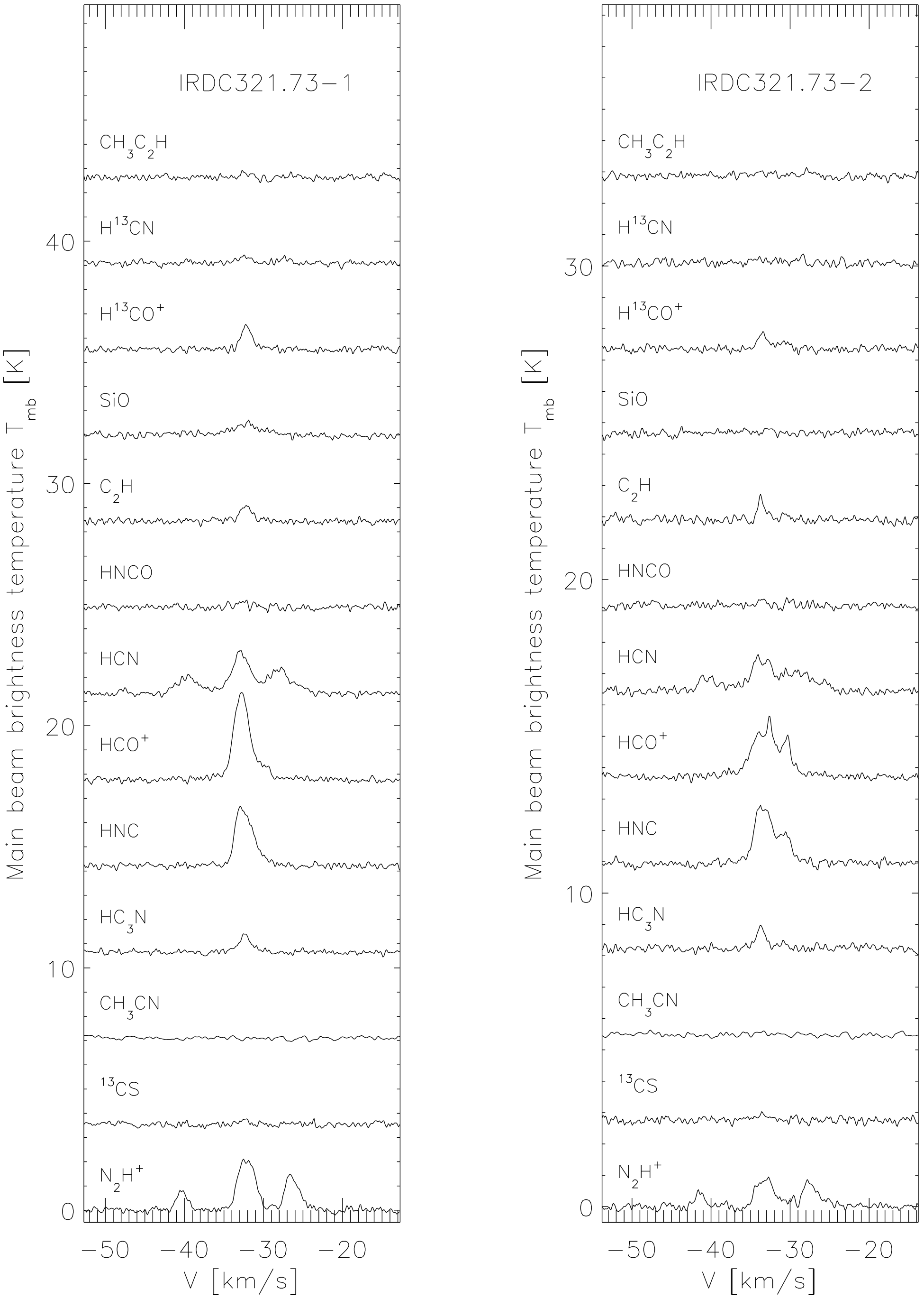

Figure C.18 Observed lines

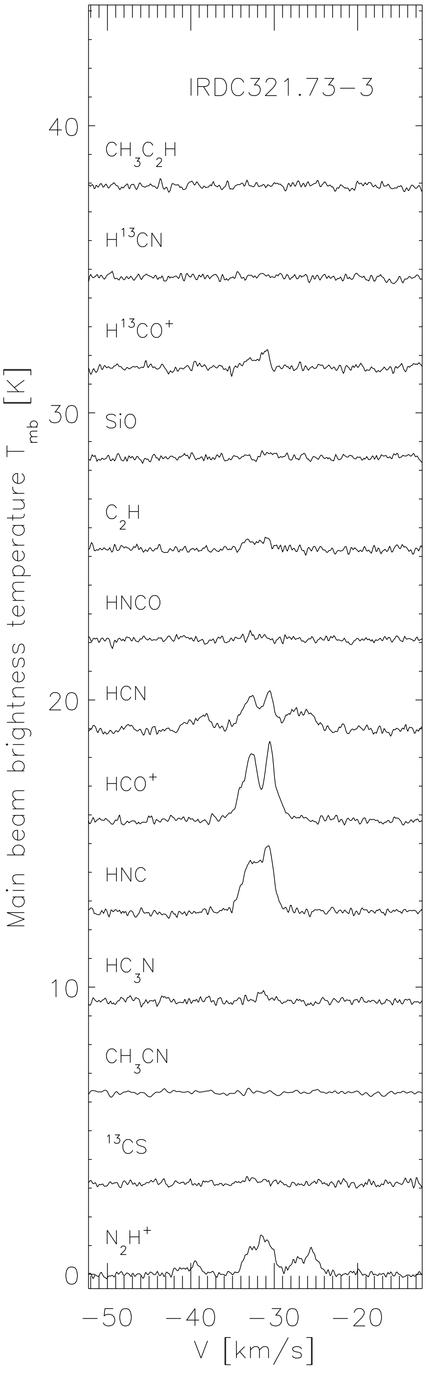

Figure C.19 Observed lines

Appendix D

Line parameters.

Table D.1. N_2H^+ line parameters.

Name	T_{mb} (K)	V_{lsr} (km/s)	δ V (km/s)	1σ rms (K)
IRDC308.13-1	0.7 (0.02)	-47.1 (0.05)	2.8 (0.08)	0.15
IRDC308.13-2	0.7 (0.2)	-48.3 (0.03)	0.8 (0.08)	0.16
IRDC308.13-3	0.8 (0.09)	-48.3 (0.03)	0.8 (0.06)	0.14
IRDC309.13-1	1.2 (0.05)	-45.1 (0.03)	1.8 (0.06)	0.15
IRDC309.13-2	0.7 (0.01)	-45.0 (0.04)	2.0 (0.08)	0.13
IRDC309.13-3	0.6 (0.07)	-45.7 (0.04)	0.8 (0.09)	0.13
IRDC309.37-1	6.4 (0.05)	-42.9 (0.01)	2.0 (0.03)	0.42
IRDC309.37-3	1.0 (0.01)	-42.9 (0.03)	2.1 (0.06)	0.13
IRDC310.39-1	2.5 (0.01)	-52.9 (0.01)	2.4 (0.02)	0.12
IRDC310.39-2	1.4 (0.02)	-52.9 (0.02)	1.7 (0.04)	0.13
IRDC312.36-1	1.4 (0.01)	-51.1 (0.02)	2.1 (0.04)	0.12
IRDC312.36-2	0.3 (0.05)	-48.8 (0.03)	0.6 (0.05)	0.11
IRDC313.72-1	1.8 (0.01)	-44.5 (0.01)	2.0 (0.03)	0.12
IRDC313.72-2	2.2 (0.01)	-44.4 (0.01)	1.7 (0.02)	0.12
IRDC313.72-3	1.9 (0.01)	-43.9 (0.01)	1.6 (0.03)	0.12
IRDC313.72-4	1.4 (0.01)	-43.6 (0.02)	1.8 (0.05)	0.12
IRDC316.72-1	3.1 (0.01)	-39.4 (0.01)	2.8 (0.01)	0.12
IRDC316.76-1	9.1 (0.01)	-40.1 (0.01)	2.6 (0.00)	0.12
IRDC316.72-2	2.5 (0.03)	-39.9 (0.01)	2.1 (0.02)	0.12
IRDC316.76-2	5.3 (0.01)	-40.9 (0.01)	2.3 (0.01)	0.12
IRDC317.71-1	2.4 (0.01)	-43.7 (0.01)	2.0 (0.02)	0.12
IRDC317.71-2	4.7 (0.01)	-44.0 (0.01)	2.2 (0.01)	0.12
IRDC317.71-3	0.7 (0.10)	-44.3 (0.03)	1.6 (0.11)	0.12
IRDC320.27-1	0.8 (0.12)	-32.4 (0.02)	1.0 (0.05)	0.13
IRDC320.27-2	0.6 (0.12)	-32.8 (0.02)	0.6 (0.04)	0.13
IRDC320.27-3	0.1 (0.05)	-32.4 (0.06)	0.5 (0.09)	0.07
IRDC321.73-1	3.0 (0.02)	-32.7 (0.01)	1.6 (0.02)	0.13
IRDC321.73-2	1.0 (0.09)	-33.7 (0.02)	1.5 (0.08)	0.12
IRDC321.73-3	1.5 (0.01)	-32.2 (0.02)	2.5 (0.03)	0.12
IRDC013.90-1	1.5 (0.02)	22.7 (0.01)	1.6 (0.04)	0.12
IRDC013.90-2	0.5 (0.07)	21.9 (0.02)	0.6 (0.05)	0.11
IRDC316.45-1	1.3 (0.08)	-43.9 (0.01)	1.4 (0.04)	0.13
IRDC316.45-2	1.3 (0.10)	-43.8 (0.02)	1.6 (0.06)	0.14
IRDC318.15-1	1.1 (0.12)	-43.0 (0.02)	1.4 (0.06)	0.12
IRDC318.15-2	1.7 (0.13)	-42.4 (0.01)	1.1 (0.03)	0.12

Table D.1 (cont'd)

Name	T $_{mb}$ (K)	V$_{lsr}$ (km/s)	δ V (km/s)	1σ rms (K)
IRDC309.94-1	4.3 (0.01)	-59.7 (0.01)	2.3 (0.01)	0.16

Note. — Columns are name, main beam brightness temperature, LSR velocity, full linewidth at half maximum, 1σ rms values.

Table D.2. ^{13}CS line parameters.

Name	$\int T_{MB}\,dv$ (K km/s)	V$_{lsr}$ (km/s)	δ V (km/s)	T $_{mb}$ (K)	1σ rms (K)
IRDC313.72-2	0.3 (0.02)	-44.1 (0.1)	1.3 (0.2)	0.2	0.06
IRDC316.76-1	0.4 (0.01)	-39.8 (0.1)	1.0 (0.0)	0.4	0.06
IRDC316.76-2	0.5 (0.02)	-40.6 (0.1)	1.9 (0.2)	0.3	0.06

Note. — Columns are name, integrated area obtained from the Gaussian fits, LSR velocity, full linewidth at half maximum, main beam brightness temperature, 1σ rms values.

Table D.3. HC_3N line parameters.

Name	$\int T_{MB}\,dv$ (K km/s)	V_{lsr} (km/s)	δ V (km/s)	T $_{mb}$ (K)	1σ rms (K)
IRDC309.37-1	2.1 (0.09)	-42.6 (0.10)	2.3 (0.2)	0.8	0.42
IRDC310.39-1	1.0 (0.03)	-52.8 (0.06)	2.4 (0.1)	0.4	0.13
IRDC310.39-2	0.4 (0.02)	-52.5 (0.07)	1.5 (0.2)	0.2	0.13
IRDC312.36-1	0.3 (0.02)	-50.7 (0.09)	1.4 (0.2)	0.2	0.12
IRDC313.72-1	1.0 (0.03)	-44.0 (0.09)	3.0 (0.2)	0.3	0.13
IRDC313.72-2	1.0 (0.02)	-44.2 (0.05)	2.1 (0.1)	0.4	0.12
IRDC316.72-1	1.0 (0.02)	-39.0 (0.07)	2.6 (0.1)	0.3	0.12
IRDC316.76-1	4.2 (0.03)	-39.9 (0.02)	3.0 (0.1)	1.2	0.12
IRDC316.72-2	0.5 (0.02)	-39.5 (0.06)	1.8 (0.1)	0.3	0.12
IRDC316.76-2	2.3 (0.02)	-40.8 (0.02)	2.2 (0.0)	0.9	0.12
IRDC317.71-1	0.5 (0.02)	-44.2 (0.12)	2.3 (0.2)	0.2	0.13
IRDC317.71-2	3.0 (0.02)	-44.1 (0.01)	2.0 (0.0)	1.4	0.13
IRDC320.27-1	0.2 (0.01)	-31.9 (0.05)	0.8 (0.1)	0.3	0.13
IRDC321.73-1	1.3 (0.02)	-32.3 (0.03)	1.8 (0.1)	0.6	0.13
IRDC321.73-2	1.0 (0.02)	-33.7 (0.03)	1.4 (0.1)	0.6	0.13
IRDC321.73-3	0.7 (0.04)	-31.3 (0.10)	2.4 (0.5)	0.2	0.13
IRDC013.90-1	0.4 (0.02)	22.8 (0.05)	1.2 (0.1)	0.3	0.12
IRDC316.45-1	0.6 (0.03)	-43.4 (0.09)	2.2 (0.2)	0.2	0.15
IRDC309.94-1	2.7 (0.04)	-59.5 (0.04)	2.9 (0.1)	0.8	0.16

Note. — Columns are name, integrated area obtained from the Gaussian fits, LSR velocity, full linewidth at half maximum, main beam brightness temperature, 1σ rms values.

Table D.4. HNC line parameters.

Name	$\int T_{MB}\,dv$ (K km/s)	V$_{lsr}$ (km/s)	δ V (km/s)	T $_{mb}$ (K)	1σ rms (K)
IRDC308.13-1	3.5 (0.02)	-47.3 (0.02)	2.1 (0.00)	1.5	0.16
IRDC308.13-2	2.1 (0.03)	-47.9 (0.02)	1.7 (0.07)	1.1	0.17
IRDC308.13-3	2.1 (0.03)	-47.8 (0.02)	1.8 (0.08)	1.0	0.16
IRDC309.13-1	3.2 (0.04)	-44.4 (0.04)	3.4 (0.10)	0.8	0.15
IRDC309.13-2	2.4 (0.04)	-45.2 (0.06)	3.7 (0.15)	0.6	0.14
IRDC309.13-3	1.1 (0.05)	-45.6 (0.15)	3.4 (0.40)	0.3	0.16
IRDC309.37-1	12.2 (0.10)	-43.1 (0.02)	2.5 (0.05)	4.4	0.41
IRDC309.37-2	1.0 (0.03)	-43.5 (0.08)	2.7 (0.20)	0.3	0.13
IRDC309.37-3	4.3 (0.03)	-43.4 (0.02)	2.7 (0.06)	1.5	0.13
IRDC310.39-1	7.9 (0.03)	-52.6 (0.01)	3.4 (0.03)	2.1	0.13
IRDC310.39-2	5.0 (0.02)	-52.5 (0.01)	2.5 (0.03)	1.8	0.13
IRDC312.36-1	4.5 (0.03)	-50.8 (0.01)	2.7 (0.04)	1.5	0.13
IRDC312.36-2	1.6 (0.04)	-49.4 (0.13)	5.3 (0.36)	0.2	0.12
IRDC313.72-1	4.7 (0.02)	-44.5 (0.01)	2.0 (0.00)	2.2	0.12
IRDC313.72-2	5.5 (0.03)	-44.4 (0.01)	2.5 (0.03)	2.0	0.12
IRDC313.72-3	6.5 (0.02)	-43.8 (0.01)	2.5 (0.02)	2.3	0.12
IRDC313.72-4	4.1 (0.02)	-44.0 (0.01)	2.0 (0.00)	1.9	0.12
IRDC316.72-1	16.6 (0.03)	-38.8 (0.01)	4.2 (0.02)	3.6	0.12
IRDC316.76-1	32.7 (0.03)	-39.6 (0.01)	4.1 (0.01)	7.3	0.12
IRDC316.72-2	9.4 (0.03)	-39.3 (0.01)	3.6 (0.03)	2.4	0.12
IRDC316.76-2	19.4 (0.04)	-40.4 (0.01)	4.1 (0.02)	4.4	0.13
IRDC317.71-1	4.3 (0.02)	-42.5 (0.01)	2.0 (0.00)	2.0	0.13
IRDC317.71-2	6.1 (0.02)	-42.7 (0.01)	1.8 (0.00)	3.1	0.12
IRDC317.71-3	1.4 (0.02)	-43.0 (0.03)	1.8 (0.00)	0.7	0.13
IRDC320.27-1	2.4 (0.03)	-32.1 (0.03)	2.8 (0.09)	0.8	0.13
IRDC320.27-2	0.9 (0.02)	-32.5 (0.04)	1.7 (0.10)	0.4	0.13
IRDC320.27-3	0.5 (0.03)	-32.6 (0.07)	1.3 (0.24)	0.3	0.13
IRDC321.73-1	6.6 (0.03)	-32.4 (0.01)	2.6 (0.02)	2.3	0.13
IRDC321.73-2	5.8 (0.02)	-33.1 (0.01)	3.0 (0.00)	1.8	0.13
IRDC321.73-3	8.3 (0.03)	-31.7 (0.01)	3.7 (0.03)	2.1	0.13
IRDC013.90-1	5.4 (0.04)	23.1 (0.02)	2.4 (0.05)	2.0	0.12
IRDC013.90-2	1.8 (0.03)	23.1 (0.05)	3.1 (0.11)	0.5	0.12
IRDC316.45-1	4.5 (0.03)	-43.5 (0.02)	3.3 (0.05)	1.2	0.15
IRDC316.45-2	4.7 (0.03)	-43.3 (0.02)	3.2 (0.05)	1.3	0.14
IRDC318.15-1	3.7 (0.02)	-42.7 (0.01)	2.5 (0.04)	1.4	0.13

Table D.4 (cont'd)

Name	$\int T_{MB}\,dv$ (K km/s)	V$_{lsr}$ (km/s)	δ V (km/s)	T $_{mb}$ (K)	1σ rms (K)
IRDC318.15-2	3.3 (0.02)	-42.0 (0.01)	2.1 (0.04)	1.4	0.13
IRDC309.94-1	8.5 (0.05)	-59.5 (0.02)	4.2 (0.05)	1.8	0.16

Note. — Columns are name, integrated area obtained from the Gaussian fits, LSR velocity, full linewidth at half maximum, main beam brightness temperature, 1σ rms values.

Table D.5. HCO^+ line parameters.

Name	$\int T_{MB}\,dv$ (K km/s)	V_{lsr} (km/s)	δ V (km/s)	T $_{mb}$ (K)	1σ rms (K)
IRDC308.13-1	4.7 (0.04)	-47.6 (0.02)	2.7 (0.07)	1.5	0.17
IRDC308.13-2	3.4 (0.03)	-47.9 (0.02)	2.1 (0.05)	1.5	0.16
IRDC308.13-3	3.0 (0.03)	-48.0 (0.02)	2.3 (0.07)	1.2	0.16
IRDC309.13-1	4.1 (0.07)	-45.0 (0.15)	9.1 (0.41)	0.4	0.16
IRDC309.13-2	3.2 (0.05)	-46.2 (0.09)	5.6 (0.20)	0.5	0.14
IRDC309.13-3	1.6 (0.03)	-47.3 (0.05)	2.6 (0.14)	0.5	0.15
IRDC309.37-1	13.9 (0.14)	-43.4 (0.02)	2.8 (0.08)	4.5	0.31
IRDC309.37-2	1.8 (0.03)	-43.6 (0.05)	2.8 (0.13)	0.6	0.14
IRDC309.37-3	5.9 (0.05)	-43.7 (0.02)	2.2 (0.06)	2.4	0.13
IRDC310.39-1	8.5 (0.05)	-53.0 (0.02)	2.3 (0.00)	3.4	0.12
IRDC310.39-2	6.4 (0.02)	-52.8 (0.01)	2.0 (0.00)	3.0	0.12
IRDC312.36-1	5.7 (0.03)	-51.0 (0.01)	2.7 (0.04)	1.9	0.12
IRDC312.36-2	1.1 (0.04)	-51.4 (0.21)	5.7 (0.44)	0.1	0.12
IRDC313.72-1	7.2 (0.06)	-44.8 (0.02)	2.5 (0.00)	2.7	0.11
IRDC313.72-2	7.1 (0.04)	-44.8 (0.02)	2.5 (0.00)	2.7	0.13
IRDC313.72-3	8.1 (0.04)	-44.2 (0.01)	2.6 (0.03)	2.8	0.12
IRDC313.72-4	7.0 (0.03)	-44.5 (0.01)	2.5 (0.00)	2.6	0.12
IRDC316.72-1	19.6 (0.04)	-38.7 (0.01)	4.0 (0.00)	4.6	0.12
IRDC316.76-1	30.0 (0.04)	-39.0 (0.01)	4.0 (0.00)	7.0	0.12
IRDC316.72-2	12.9 (0.04)	-38.9 (0.01)	5.4 (0.05)	2.2	0.12
IRDC316.76-2	23.2 (0.04)	-39.3 (0.01)	6.5 (0.03)	3.3	0.12
IRDC317.71-1	4.5 (0.02)	-41.9 (0.01)	2.1 (0.00)	2.0	0.13
IRDC317.71-2	4.5 (0.02)	-42.1 (0.01)	2.1 (0.00)	2.0	0.12
IRDC317.71-3	2.3 (0.02)	-42.7 (0.02)	2.1 (0.00)	1.0	0.12
IRDC320.27-1	1.1 (0.03)	-31.0 (0.04)	1.5 (0.00)	0.7	0.12
IRDC320.27-2	0.7 (0.02)	-33.0 (0.03)	1.3 (0.10)	0.5	0.12
IRDC320.27-3	0.4 (0.01)	-32.9 (0.02)	0.7 (0.06)	0.5	0.14
IRDC321.73-1	9.2 (0.03)	-32.7 (0.01)	2.4 (0.02)	3.4	0.13
IRDC321.73-2	8.0 (0.04)	-32.7 (0.02)	5.0 (0.06)	1.4	0.12
IRDC321.73-3	4.3 (0.10)	-30.6 (0.05)	1.5 (0.00)	2.7	0.14
IRDC013.90-1	5.4 (0.03)	23.1 (0.01)	2.4 (0.04)	2.1	0.45
IRDC013.90-2	2.1 (0.04)	23.5 (0.07)	3.4 (0.12)	0.5	0.20
IRDC316.45-1	4.7 (0.04)	-43.2 (0.03)	4.3 (0.09)	1.0	0.12
IRDC316.45-2	3.6 (0.03)	-43.3 (0.04)	4.1 (0.09)	0.8	0.13
IRDC318.15-1	1.9 (0.02)	-43.3 (0.02)	1.8 (0.00)	0.9	0.12

Table D.5 (cont'd)

Name	$\int T_{MB}\,dv$ (K km/s)	V$_{lsr}$ (km/s)	δ V (km/s)	T $_{mb}$ (K)	1σ rms (K)
IRDC318.15-2	0.9 (0.02)	-43.2 (0.06)	1.8 (0.00)	0.5	0.12
IRDC309.94-1	9.9 (0.06)	-60.3 (0.03)	5.4 (0.08)	1.7	0.15

Note. — Columns are name, integrated area obtained from the Gaussian fits, LSR velocity, full linewidth at half maximum, main beam brightness temperature, 1σ rms values.

Table D.6. HNCO line parameters.

Name	$\int T_{MB}\,dv$ (K km/s)	V$_{lsr}$ (km/s)	δ V (km/s)	T $_{mb}$ (K)	1σ rms (K)
IRDC309.37-1	1.3 (0.07)	-42.4 (0.12)	2.3 (0.36)	0.5	0.15
IRDC310.39-1	0.3 (0.02)	-53.8 (0.08)	1.3 (0.20)	0.2	0.07
IRDC312.36-1	0.4 (0.02)	-50.4 (0.14)	2.5 (0.26)	0.1	0.06
IRDC313.72-1	0.5 (0.02)	-44.3 (0.06)	1.4 (0.19)	0.3	0.06
IRDC313.72-2	0.6 (0.02)	-44.1 (0.13)	2.9 (0.30)	0.1	0.05
IRDC313.72-3	0.3 (0.02)	-43.6 (0.11)	2.0 (0.36)	0.1	0.06
IRDC316.72-1	0.9 (0.03)	-39.1 (0.08)	2.6 (0.18)	0.3	0.06
IRDC316.76-1	1.0 (0.03)	-39.7 (0.10)	3.3 (0.29)	0.2	0.06
IRDC317.71-1	0.6 (0.03)	-43.5 (0.09)	2.0 (0.23)	0.3	0.07
IRDC317.71-2	1.1 (0.04)	-43.7 (0.10)	3.4 (0.31)	0.3	0.06
IRDC320.27-1	0.3 (0.01)	-31.7 (0.07)	1.3 (0.17)	0.2	0.06
IRDC316.45-1	0.3 (0.02)	-43.4 (0.08)	1.4 (0.19)	0.2	0.07
IRDC316.45-2	0.4 (0.02)	-43.2 (0.07)	1.5 (0.16)	0.3	0.07
IRDC309.94-1	1.1 (0.03)	-59.4 (0.08)	2.6 (0.22)	0.3	0.07

Note. — Columns are name, integrated area obtained from the Gaussian fits, LSR velocity, full linewidth at half maximum, main beam brightness temperature, 1σ rms values.

Table D.7. SiO line parameters.

Name	$\int T_{MB}\,dv$ (K km/s)	V$_{lsr}$ (km/s)	δ V (km/s)	T $_{mb}$ (K)	1σ rms (K)
IRDC309.37-1	0.9 (0.08)	-42.6 (0.2)	2.8 (0.5)	0.3	0.18
IRDC310.39-1	0.6 (0.03)	-53.3 (0.2)	3.9 (0.4)	0.1	0.08
IRDC312.36-1	0.2 (0.03)	-50.8 (0.2)	2.0 (0.5)	0.1	0.08
IRDC313.72-1	1.6 (0.04)	-43.9 (0.1)	4.5 (0.3)	0.3	0.08
IRDC313.72-2	1.7 (0.05)	-44.4 (0.1)	5.1 (0.4)	0.3	0.08
IRDC313.72-3	1.3 (0.06)	-41.9 (0.3)	8.2 (0.8)	0.1	0.08
IRDC313.72-4	0.5 (0.03)	-44.1 (0.2)	3.4 (0.4)	0.1	0.08
IRDC316.76-1	2.4 (0.07)	-39.5 (0.2)	8.9 (0.7)	0.2	0.08
IRDC317.71-3	0.3 (0.03)	-42.1 (0.2)	1.9 (0.5)	0.1	0.08
IRDC321.73-1	2.1 (0.05)	-32.1 (0.1)	4.8 (0.3)	0.4	0.08
IRDC309.94-1	2.4 (0.05)	-59.6 (0.2)	5.0 (0.0)	0.4	0.10

Note. — Columns are name, integrated area obtained from the Gaussian fits, LSR velocity, full linewidth at half maximum, main beam brightness temperature, 1σ rms values.

Table D.8. $H^{13}CO^+$ line parameters.

Name	$\int T_{MB}\, dv$ (K km/s)	V_{lsr} (km/s)	δ V (km/s)	T $_{mb}$ (K)	1σ rms (K)
IRDC308.13-1	0.6 (0.06)	-46.7 (0.28)	2.5 (0.41)	0.2	0.08
IRDC309.13-1	0.8 (0.05)	-44.7 (0.14)	2.1 (0.31)	0.3	0.07
IRDC309.13-3	0.5 (0.05)	-45.2 (0.12)	1.5 (0.39)	0.3	0.08
IRDC309.37-1	2.6 (0.13)	-42.6 (0.09)	2.1 (0.26)	1.1	0.16
IRDC309.37-3	1.3 (0.06)	-42.4 (0.15)	3.2 (0.34)	0.3	0.08
IRDC310.39-1	1.9 (0.04)	-52.4 (0.04)	1.9 (0.11)	0.9	0.08
IRDC310.39-2	1.2 (0.05)	-52.3 (0.09)	2.2 (0.20)	0.5	0.08
IRDC312.36-1	1.3 (0.06)	-50.6 (0.13)	3.0 (0.35)	0.4	0.08
IRDC312.36-2	0.2 (0.03)	-48.8 (0.20)	1.4 (0.38)	0.1	0.08
IRDC313.72-1	1.1 (0.08)	-43.9 (0.19)	2.5 (0.63)	0.4	0.08
IRDC313.72-2	1.1 (0.05)	-43.9 (0.10)	2.2 (0.31)	0.4	0.08
IRDC313.72-3	0.7 (0.04)	-43.5 (0.10)	1.8 (0.21)	0.4	0.08
IRDC313.72-4	0.8 (0.05)	-43.3 (0.12)	2.2 (0.30)	0.3	0.08
IRDC316.72-1	4.4 (0.06)	-38.8 (0.04)	3.1 (0.10)	1.2	0.08
IRDC316.76-1	5.2 (0.06)	-39.7 (0.03)	3.2 (0.09)	1.5	0.08
IRDC316.72-2	2.7 (0.05)	-39.5 (0.04)	2.2 (0.09)	1.1	0.08
IRDC316.76-2	3.1 (0.05)	-40.5 (0.04)	2.4 (0.10)	1.1	0.08
IRDC317.71-1	1.3 (0.04)	-43.3 (0.07)	1.9 (0.17)	0.6	0.08
IRDC317.71-2	1.7 (0.05)	-43.8 (0.05)	1.9 (0.16)	0.8	0.08
IRDC317.71-3	0.4 (0.04)	-43.7 (0.20)	1.7 (0.47)	0.2	0.09
IRDC320.27-1	0.7 (0.03)	-31.9 (0.05)	1.1 (0.12)	0.5	0.09
IRDC321.73-1	1.6 (0.04)	-32.1 (0.04)	1.5 (0.09)	0.9	0.08
IRDC321.73-2	0.6 (0.04)	-33.4 (0.08)	1.3 (0.22)	0.4	0.08
IRDC321.73-3	1.2 (0.06)	-31.6 (0.14)	2.5 (0.31)	0.4	0.09
IRDC013.90-1	1.0 (0.04)	23.3 (0.09)	1.9 (0.18)	0.5	0.08
IRDC013.90-2	0.3 (0.02)	22.3 (0.03)	0.4 (0.10)	0.6	0.08
IRDC316.45-1	0.8 (0.05)	-43.5 (0.12)	1.9 (0.25)	0.4	0.08
IRDC316.45-2	1.1 (0.05)	-43.3 (0.10)	2.2 (0.23)	0.4	0.08
IRDC318.15-1	0.7 (0.04)	-42.5 (0.09)	1.6 (0.21)	0.4	0.08
IRDC318.15-2	0.6 (0.04)	-42.0 (0.10)	1.5 (0.20)	0.3	0.08
IRDC309.94-1	1.7 (0.06)	-59.3 (0.07)	2.1 (0.17)	0.7	0.11

Note. — Columns are name, integrated area obtained from the Gaussian fits, LSR velocity, full linewidth at half maximum, main beam brightness temperature, 1σ rms values.

Table D.9. Integrated areas, measured by summing the channels between suitable velocity limits under the line.

Name	N_2H^+ (K km/s)	^{13}CS (K km/s)	HC_3N (K km/s)	HNC (K km/s)	HCO^+ (K km/s)	HCN (K km/s)	HNCO (K km/s)	C_2H (K km/s)	SiO (K km/s)	$H^{13}CN$ (K km/s)	CH_3C_2H (K km/s)
IRDC308.13-1	4.2			4.8	6.2	5.3					
IRDC308.13-2	2.1			2.6	4.2	2.9		0.6			
IRDC308.13-3	1.6			2.9	3.7	3.3					
IRDC309.13-1	5.0			3.1	4.1	4.5		0.4			
IRDC309.13-2	2.8			2.5	3.2	3.9					
IRDC309.13-3	1.5			0.8	1.9	2.3					
IRDC309.37-1	29.1		1.6	13.6	17.9	15.4	1.4	3.2			
IRDC309.37-2				1.2	2.4	2.4					
IRDC309.37-3	4.6			4.8	6.8	6.0					
IRDC310.39-1	13.4		1.9	8.1	13.3	12.5	0.2	1.7	0.4		
IRDC310.39-2	5.4		1.2	5.5	8.7	9.0		1.4			
IRDC312.36-1	6.2		0.2	4.9	6.6	6.6	0.6	0.7			
IRDC312.36-2	1.3			1.9	1.0	2.1					
IRDC313.72-1	8.0		1.7	6.9	11.3	7.8	0.6	1.1	1.6		
IRDC313.72-2	8.6	0.3	1.2	6.7	10.6	8.0	0.5	0.9	1.9		
IRDC313.72-3	7.1		0.6	7.3	9.1	7.3	0.4	0.6	1.3		
IRDC313.72-4	5.9			5.7	9.3	5.9			0.6		
IRDC316.72-1	18.4		1.1	17.1	23.2	18.6	0.8	2.8		1.9	0.3
IRDC316.76-1	50.7	0.9	4.9	34.1	34.6	33.8	1.1	7.1	2.3	4.8	0.7
IRDC316.72-2	11.8		0.8	10.2	14.1	10.9		1.9			0.3
IRDC316.76-2	27.4	0.5	2.9	21.4	23.3	27.4		7.1		3.3	0.3
IRDC317.71-1	10.5		0.4	5.0	5.6	2.7	0.7	0.8			
IRDC317.71-2	21.9		2.9	8.1	5.6	4.9	1.3	1.5		1.5	0.57
IRDC317.71-3	3.5			2.3	2.5	1.8			1.0		
IRDC320.27-1	2.5			2.6	2.6	3.8					
IRDC320.27-2	1.7			1.1	0.7	1.7					
IRDC320.27-3	0.6			0.8	0.3	0.8					
IRDC321.73-1	11.0		1.3	7.0	10.5	11.1		1.4	2.5		
IRDC321.73-2	5.5		1.7	6.9	8.4	7.9		0.9			
IRDC321.73-3	7.5		1.3	8.4	10.4	8.9		0.8			
IRDC013.90-1	5.6		0.7	5.6	6.3	5.4		0.9			
IRDC013.90-2	2.4			1.4	0.8	1.9					
IRDC316.45-1	7.0		1.0	4.7	5.1	4.0	0.1	0.7			
IRDC316.45-2	6.2			4.9	3.4	4.0	0.4	0.7			
IRDC318.15-1	3.7			3.9	3.0	3.3		0.7			
IRDC318.15-2	4.6			3.9	1.8	2.9		0.5			
IRDC309.94-1	22.0		3.7	9.4	11.0	11.8	0.9	2.4		2.1	

Note. — Columns are name, integrated area for every species.

Declaration

I herewith declare that I have produced this paper without the prohibited assistance of third parties and without making use of aids other than those specified; notions taken over directly or indirectly from other sources have been identified as such. This paper has not previously been presented in identical or similar form to any other German or foreign examination board.

The thesis work was conducted from 2007 to 2010 under the supervision of Prof. Dr. Thomas Henning, Dr. Hendrik Linz and Dr. Arjan Bik at the Max-Planck-Institute for Astronomy (MPIA).

Heidelberg, September 27, 2010.